REPORT DOCUMENTATION PAGE

Form Approved
OMB NO. 0704-0188

1. AGENCY USE ONLY (Leave Blank)	2. REPORT DATE February 2008	3. REPORT TYPE AND DATES COVERED

4. TITLE AND SUBTITLE

Ultrasonically Absorptive Coatings for Hypersonic Laminar Flow Control

5. FUNDING NUMBERS

6. AUTHOR(S)

David Marshall and Alexander Fedorov

7. PERFORMING ORGANIZATION NAME(S) AND ADDRESS(ES)

Teledyne Scientific Company
1049 Camino Dos Rios
Thousand Oaks, CA 91360

8. PERFORMING ORGANIZATION REPORT NUMBER

9. SPONSORING / MONITORING AGENCY NAME(S) AND ADDRESS(ES)

AFOSR

10. SPONSORING / MONITORING AGENCY REPORT NUMBER

11. SUPPLEMENTARY NOTES

The views, opinions and/or findings contained in this report are those of the author(s) and should not be construed as an official Department of the Army position, policy or decision, unless so designated by other documentation.

12 a. DISTRIBUTION / AVAILABILITY STATEMENT

Approved for public release; distribution unlimited.

12 b. DISTRIBUTION CODE

13. ABSTRACT

This report summarizes results of theoretical, numerical and experimental studies related to ultrasonically absorptive coatings (UAC) for laminarization of hypersonic boundary layer flow. Laminar flow control (LFC) technologies reduce heat-transfer rates as well as the weight and complexity of thermal protection system (TPS). The effort has been focused on maturing of the UAC-LFC methodology. Key components of the effort include theoretical analysis, direct numerical simulation (DNS), wind-tunnel experiments, as well as fabrication of ceramic materials that integrate UAC and TPS functions. To aid in the design of UAC with regular microstructure to be tested the CUBRC LENS I tunnel, parametric studies of the UAC-LFC performance were conducted for Mach=7 and Mach=10 free-stream conditions. The UAC parameters providing significant (more than twice) increase of the laminar run were predicted. First steps have been made in mathematical (from first principles) modeling of acoustic processes in UAC of random structure. 2-D DNS of receptivity and stability of boundary layers on a flat plate and a sharp cone at Mach=6 free stream confirmed robustness of our theoretical tools for estimates of the UAC-LFC performance. DNS of the reflection of acoustic pulses by UAC comprising 2-D blind micro-cavities (without boundary-layer flow) showed that the reflection coefficient predicted by DNS agrees well with our theoretical model. Blunted cones with the felt-metal coating were tested in the ITAM AT-303 wind tunnel at Mach=8.8. Transition measurements showed that the felt-metal UAC causes 1.3-1.85 times increase of the laminar run. First samples of a ceramic UAC integrated into TPS tile were fabricated using a stamping technique. Benchmark (no flow) measurements of the ultrasonic reflection on UAC of regular microstructure agree well with theoretical prediction. The results reported herein provide a solid foundation for large-scale demonstration of the UAC-LFC performance the CUBRC LENS I tunnel as well as fabrication of ceramic UAC samples integrated into TPS.

14. SUBJECT TERMS

Laminar flow control, porous coating, ultrasonic absorption, ultrasonic reflection, boundary layer stability, hypersonic flow, transition measurements, direct numerical simulation, theoretical modeling, acoustic disturbances

15. NUMBER OF PAGES

16. PRICE CODE

17. SECURITY CLASSIFICATION OR REPORT	18. SECURITY CLASSIFICATION ON THIS PAGE	19. SECURITY CLASSIFICATION OF ABSTRACT	20. LIMITATION OF ABSTRACT
UNCLASSIFIED	**UNCLASSIFIED**	**UNCLASSIFIED**	UL

TELEDYNE SCIENTIFIC COMPANY
A Teledyne Technologies Company

Dedicated to memory of Dr. Norman Malmuth

Ultrasonically Absorptive Coatings for Hypersonic Laminar Flow Control

Final Report

AFOSR Contract FA9550-06-C-0097

for the period 12/01/2006 thru 12/01/2007

Prepared by:

Alexander Fedorov

Department of Aeromechanics and Flight Engineering
Moscow Institute of Physics and Technology
Zhukovsky, Moscow Region 140180

Norm Malmuth, David Marshall and Janet Davis

Teledyne Scientific Company
Thousand Oaks, CA 91360

December 2007

Executive summary

This report summarizes results of theoretical, numerical and experimental studies related to ultrasonically absorptive coatings (UAC) for laminarization of hypersonic boundary layer flow. Laminar flow control (LFC) technologies reduce heat-transfer rates as well as the weight and complexity of thermal protection system (TPS). The project was focused on maturing of the UAC-LFC methodology. Key components of the effort included theoretical analysis, direct numerical simulation, wind-tunnel experiments as well as fabrication and testing of ceramic materials that integrate UAC and TPS functions. To aid in the design of UAC with regular microstructure to be tested the CUBRC LENS I tunnel, extensive parametric studies of the UAC laminar flow control performance were conducted for Mach=7 and Mach=10 free-stream conditions. The UAC parameters providing significant (more than twice) increase of the laminar run were predicted. Results of these studies can be used for design and manufacturing of large-scale models with UAC of regular microstructures that could be tested under free-stream conditions relevant to hypersonic flight. First steps have been made in mathematical (from first principles) modeling of the acoustic processes in UAC of random structure. Namely, we derived governing equations, formulated a unit problem for propagation of acoustic wave in highly porous layered fibrous materials, and outlined its solution in terms of a Fourier series. Direct numerical simulation (DNS) of the second mode evolution in the boundary layer on a flat plate at Mach6 free stream was carried out using the theoretical boundary conditions on the UAC surface. It was shown that stability characteristics predicted by DNS agree well with linear stability theory. The UAC boundary effect associated with the juncture between solid and porous walls was simulated. It was shown that this effect is local and can be neglected in prediction of the integral laminar-flow-control performance of UAC coatings. To clarify pore-end effects we have conducted a series of DNS calculations for the reflection of acoustic pulses by UAC comprising 2-D blind micro-cavities (without external flow). These numerical simulations provided details of the disturbance field inside cavities and near the cavity edges as well as the reflection coefficient associated with the acoustic far field. It was shown that the reflection coefficients predicted by DNS agree well with our theoretical model. A cone of length 1 m with felt-metal coating (UAC of random micro-structure) was tested in the ITAM AT-303 wind tunnel at Mach8.8 free stream. Transition measurements were carried out on coated and uncoated cone surfaces at various nose-tip radii. The cone configuration is similar to the FRESH FX-1 fore-cone shape. It was shown that the felt-metal UAC causes 1.3-1.85 times increase of the laminar run. First samples of ceramic UAC integrated with TPS tile were fabricated. It was demonstrated that using a stamping technique it is feasible to make equally spaced blind holes of 100 -200 μm diameter and 500-600 μm depth. Parameters of these pores fit to laminar flow control requirements predicted theoretically. Apparatus for benchmark (no flow) measurements of ultrasonic absorption by porous coatings was assembled. Its robustness was demonstrated at low ambient pressures relevant to high-altitude flight conditions. The reflection coefficients measured in this facility agree well with our theoretical prediction. This facility can be used for measurements of acoustic characteristics of UAC-TPS articles. The results reported herein provide a solid foundation for large-scale demonstration of the UAC-LFC performance in the CUBRC LENS I tunnel as well as for fabrication of ceramic UAC integrated into TPS. This, in turn, provides basis for design of UAC-TPS test articles that could be flight tested within the framework of the HIFiRE (Hypersonic International Flight Research and Experimentation) program that includes transition measurements on cones and other configurations.

Technical Contributors

N. Malmuth (TSC, Thousand Oaks, CA) – former PI of this project, passed away on July 3, 2007

J. Davis, and D. Marshall (TSC, Thousand Oaks, CA) – Developments of ceramic UAC (Section 2.7)

R. Addison (TSC, Thousand Oaks, CA) – Benchmark measurements of reflection coefficients (Section 2.3)

G. Brès and T. Colonius (Caltech) – Direct numerical simulation of interaction of acoustic disturbances with UAC micro-cavities (Section 2.4)

A. Fedorov (MIPT, Moscow) – Theoretical analyses (Sections 2.1, 2.2, and 2.3)

V. Kozlov (MIPT, Moscow) – Theoretical analyses (Sections 2.3 and 2.6)

V. Soudakov (MIPT, Moscow) – Numerical simulation of UAC stabilization effect (Section 2.2)

A. Maslov, A. Shiplyuk, L. Vasenev, S. Shpak, and S. Lukashevich (ITAM, Novosibirsk) – Transition measurements on blunted cone with the felt-metal coating (Section 2.5)

M. Holden (CUBRC, Buffalo NY) – Data on transition in LENS facilities (Section 2.1)

H. Hornung – Technical discussions

E. Reshotko – Technical discussions

Table of contents

1. Background

Laminar-turbulent transition during hypersonic flight represents a severe restriction to vehicle performance [1], since early transition causes a significant increase (by a factor of 3-8) in heat transfer, which translates to higher cost and weight of thermal protection system (TPS) [2,3]. For hypersonic air-breathers, premature transition may be mission-critical because it reduces propulsion system efficiency, increases viscous drag (that can be more than 30% of the total drag), as well as degrading aerodynamic control surfaces and reaction control system performance. Because of these issues, strategies for achieving economically viable aerospace systems require laminar flow control (LFC) concepts that substantially delay transition [4]. State-of-the-art active and reactive LFC methods seem to be impractical under the severe conditions of hypersonic flight. Accordingly, passive LFC methods are promising to solve this problem.

In contrast to blunt configurations (e.g., Viking, Apollo type capsules) and moderately blunt lifting type configurations (e.g., Space Shuttle, the X-37 reusable launch vehicle), air-breathing hypersonic vehicles (e.g., NASP, Hyper-X) with relatively sharp leading edges can achieve high lift-to-drag ratio and fly at low angles of attack. This significantly increases local Mach numbers on the vehicle surfaces and leads to favorable changes in laminar-turbulent transition, namely:

- Roughness-induced transition becomes less important compared to other transition mechanisms since the critical roughness height quickly increases with the local Mach number [5]
- Relatively small leading-edge radii associated with hypersonic airbreathing cruise vehicles prevent transition due to nose-tip roughness and leading-edge contamination [6]
- The first mode (associated with Tollmien-Schlichting waves) does not amplify because of low wall temperature ratios [7]

Furthermore, shaping of hypersonic air-breathers is designed to achieve massive reduction of cross-flow and Görtler vortices. Under such conditions the second mode may become a dominant instability. This suggests that the laminar run can be substantially increased by stabilization of the second mode.

Because the second mode represents high-frequency (ultrasonic) trapped acoustic waves, Malmuth *et al.* [8] assumed that a passive ultrasonically absorptive coating (UAC) may stabilize the second mode and, at the same time, be aerodynamically smooth. This hypothesis was confirmed by the theoretical study [9] based on the linear stability theory. The transition experiments of Rasheed *et al.* [10], which were performed on a sharp cone in the GALCIT T5 high-enthalpy shock tunnel, qualitatively agree with the theoretical predictions. The stability experiments [11, 12] were conducted on sharp cones with porous coatings of random and regular microstructures in the T-326 wind tunnel of the Institute of Theoretical and Applied Mechanics (ITAM, Novosibirsk). Hot wire measurements and linear stability theory (LST) showed that the UAC of fibrous absorbent material (felt metal) effectively stabilizes the second mode and slightly destabilizes the first mode [11]. The UAC of regular microstructure (a perforated thin sheet which is analogous to that used in the experiments [10]) also leads to massive reduction of the second-mode growth rate, while it weakly affects the first mode [12]. Nonlinear aspects of the second mode stabilization by UAC of regular microstructure were studied using bi-spectral analysis [13]. It was shown that the harmonic resonance, which is quite pronounced in the latter stages of the disturbance evolution on solid surfaces, is completely suppressed on the porous

surface. Furthermore, the experiments [14], which were carried out in the ITAM AT-303 high-enthalpy wind tunnel at Mach=12, showed that the felt-metal coating significantly (up to 100% of the model length) delayed transition on a sharp cone.

These studies confirmed robustness of the UAC stabilization concept and motivated further experimental, DNS and theoretical efforts to mature the UAC-LFC methodology and provide a basis for design of UAC-TPS test articles that could be manufactured and deployed on a flight vehicle. Such articles could be flight tested within the framework of the HIFiRE (Hypersonic International Flight Research and Experimentation) project [15].

The aforementioned stability and transition experiments have been carried out on relatively small models. It is important to demonstrate robustness of the UAC-LFC method on large-scale configurations. In this connection, it is planned to carry out transition experiments in the CUBRC LENS facilities on a 3 m length cone model instrumented with the UAC surface. To aid in the design of the porous coating to be tested in these experiments, we have conduced parametric studies of the UAC-LFC performance for the free-stream conditions of the CUBRC LENS I shock tunnel. Results of this analysis are discussed in Section 2.1.

In previous works stability calculations were carried out using LST of the local-parallel or weakly nonparallel approximation. The mean flow was approximated by self-similar (compressible Blasius) solutions for a flat plate or sharp cone; i.e., the viscous-inviscid interaction was neglected. Nonuniformity of the boundary conditions due to UAC end effects associated with the upstream and downstream junctures between coated and uncoated surfaces was not considered. Interaction of free-stream disturbances with the porous surface was not analyzed. These aspects are addressed in Section 2.2 using direct numerical simulation (DNS) of boundary-layer disturbances on solid and porous walls. Results of this study are published in Ref. [16].

Since the second mode represents trapped acoustic waves of high (ultrasonic) frequency band [17], it is assumed that basic features of its interaction with a porous coating can be captured by considering reflection of ultrasonic disturbances from the UAC surface without external boundary-layer flow. In Section 2.3, we have analyzed reflection of ultrasonic waves from a plane surface covered by UAC of regular micro-structure comprising equally spaced cylindrical blind holes. The theoretical prediction of the reflection coefficient is compared with the benchmark (no flow) measurements at various ambient pressures with special emphasis on low pressures relevant to high-altitude hypersonic flights.

To validate our porous-wall boundary-condition models, we conduct DNS of unsteady processes within 2-D micro cavities that constitute UAC. This helps to examine end-effects at the mouths and bottoms of cavities, clarify dependencies of the UAC performance on the cavity spacing and depth, propose improvements of existing models to extend their range of validity, and generalize their use as a tool for design and implementation of UAC in applications. In Section 2.4, we consider the interaction of incident acoustic waves with groups of equally-spaced 2-D micro-cavities on the flat plate surface without flow. Although the external boundary layer flow is an important component of the UAC modeling, this unit problem is of particular interest, since mechanisms of reflection and absorption of incoming boundary-layer disturbances occur near the cavity edges and inside cavities where the external flow is relatively slow and seems to play a minor role. Furthermore, the acoustic properties of UAC samples should be estimated in an economical way before their testing in hypersonic wind tunnels. This can be done using the

aforementioned benchmark measurements of the reflection of acoustic waves from the porous coating.

UAC of random porosity could be more symbiotic with thermal protection systems (TPS) of actual hypersonic vehicles since the majority of TPS materials have random microstructures. This motivated us to conduct transition measurements on blunted cones with the felt-metal coating in the ITAM AT-303 hypersonic wind tunnel at free stream Mach number M_∞=8.8. The experimental results, which are presented in Section 2.5, help to estimate the nose bluntness effect on the UAC-LFC performance.

The first-cut model of acoustic absorption by UAC of random structure was developed in Ref. [11] and used for formulation of the boundary conditions on the felt-metal coating [11,14]. In Section 2.6, we continue our previous theoretical studies of a randomly porous UAC. Namely, we suggest new approach for modeling of slow gas motions (including acoustic disturbances) in highly porous fibrous materials. The differential equations governing this problem are derived from first principles using rigorous mathematical methods. The problem of sound propagation in highly porous layered fibrous materials is formulated. Its analytical solution is expressed in terms of Fourier series. These studies will help to refine our previous model [11] and formulate more accurate boundary conditions on UAC of random porosity.

In Section 2.7, we discuss results on development and demonstration of a suitable method for fabrication of UAC-TPS samples of relatively small ($6'' \times 6''$) dimension. The choice of materials and processing methods are constrained to those that could be reasonably scaled up in a follow-on program to manufacture large panels for wind-tunnel or flight testing ($10' \times 3'$). Several approaches have been assessed for producing porosity of the required size range (~ 100-200 μm diameter by ~ 500-600 μm depth), either in a periodic pattern or random array. In the reporting period, we have concentrated on coatings with porosity resembling an ideal geometry of regularly spaced blind holes, formed by adding a layer containing the holes to an existing rigid fibrous TPS tile with a smooth dense surface layer (i.e., reaction-cured glass as in space shuttle tiles). First samples of ceramic UAC integrated into the TPS tile are presented. It is shown that using the stamping technique it is feasible to make equally spaced blind cylindrical holes of the aforementioned diameter and depth. Parameters of these pores fit to laminar flow control requirements predicted by our theory.

2. Major accomplishments

2.1. Parametric studies of hypersonic laminar-flow control using UAC of regular microstructure

2.1.1. Theoretical model

Herein we briefly discuss the theoretical model used for parametric estimates of the UAC-LFC performance. Details are given in Ref. [18]. Consider the laminar boundary-layer flow past a sharp cone at zero angle of attack. The fluid is treated as a perfect gas of specific heat ratio $\gamma = 1.4$ and Prandtl number $\mathrm{Pr} = 0.72$. The mean flow in the laminar boundary layer is calculated using a self-similar solution of boundary-layer equations (compressible Blasius solution). It is assumed that the mean flows on both porous and solid surfaces are identical. The dynamic viscosity μ is calculated using the Sutherland formula. For stability calculations, the second viscosity is approximated as $\mu_v = 0.8\mu$, where μ is dynamic viscosity. The coordinates

x, y, z are nondimensionalized using the boundary-layer length scale $\Delta^* \equiv \sqrt{\nu_e^* x_p^* / U_e^*}$, where $x_p^* = x^* / 3$ according to the Mangler transformation. Three-dimensional disturbances are represented in the traveling-wave form

$$\tilde{q} = \text{Real}\{q(y)\exp[i(\alpha x + \beta z - \omega t)]\}, \quad \tilde{q} = (\tilde{u}, \tilde{v}, \tilde{w}, \tilde{p}, \tilde{\theta}), \tag{1.1}$$

where $\tilde{u}, \tilde{v}, \tilde{w}$ are velocity components; $\tilde{p}$ is pressure referenced to $\rho_e^* U_e^{*2}$, $\tilde{\theta}$ is temperature; $\alpha = \alpha^* \Delta^*$ and $\beta = \beta^* \Delta^*$ are wavenumber components; $\omega = \omega^* \Delta^* / U_e^*$ is angular frequency; asterisks denote dimensional quantities . The linear stability problem is formulated for locally parallel mean flow [17]. Since the boundary-layer modes exponentially decay as $y \to \infty$, the outer boundary conditions are

$$u(\infty) = v(\infty) = w(\infty) = \theta(\infty) = 0. \tag{1.2}$$

On the solid wall, the boundary conditions are

$$u(0) = v(0) = w(0) = \theta(0) = 0. \tag{1.3}$$

Solutions of the eigenvalue problem give the dispersion relationship $F(\alpha, \beta, \omega; M_e, R) = 0$, where M_e is Mach number at the upper boundary-layer edge, $R \equiv \sqrt{U_e^* x_p^* / \nu_e^*}$ is local Reynolds number, ν^* is kinematic viscosity. For spatial instability in 2-D or conical boundary layers, the frequency ω and the transverse wavenumber β are real, whereas α is complex eigenvalue. If $\text{Im}(\alpha) < 0$, then the disturbance amplifies with the spatial growth rate $\sigma_\alpha = -\text{Im}(\alpha)$.

Consider a porous coating with equally spaced vertical cylindrical blind micro-holes (Fig. 1.1). This coating has a regular microstructure that is characterized by the pore radius r, spacing s and depth h. On the porous wall, the boundary conditions for the vertical velocity and temperature disturbances are expressed as [9]

$$v(0) = Ap(0), \tag{1.4}$$
$$\theta(0) = Bp(0), \tag{1.5}$$

where A (porous-layer admittance) and B (thermal admittance) are complex quantities that depend on the porous layer characteristics, mean-flow parameters at $y = 0$ as well as the disturbance frequency and wavelength. The admittance A is calculated as [9]

$$A = -\frac{\phi}{Z_0}\tanh(m\,h), \tag{1.6}$$

where $h = h^* / \Delta^*$ – nondimensional thickness of the porous layer, $\phi = \pi r^2 / s^2$ – porosity. The characteristic impedance Z_0 and the propagation constant m are expressed in terms of the nondimensional complex dynamic density $\tilde{\rho} = \tilde{\rho}^* / \rho_e^*$ and the complex compressibility $\tilde{C} = \tilde{C}^* p_e^*$ as

$$Z_0 = \frac{\sqrt{\tilde{\rho} / \tilde{C}}}{M_e \sqrt{T_w}}, \; m = \frac{i\omega M_e}{\sqrt{T_w}}\sqrt{\tilde{\rho}\,\tilde{C}}, \tag{1.7}$$

where $T_w = T_w^* / T_e^*$ is nondimensional wall temperature. The values of $\tilde{\rho}$ and $\tilde{C}$ are calculated using analytical solutions for acoustic disturbances propagating within a long tube as reported in Ref. [19]. Note that these solutions account for gas rarefaction effect for small but finite Knudsen numbers based on the pore radius. As shown in Ref. [9] the thermal admittance produces negligible effect on the second-mode stability that allows us to put $B = 0$.

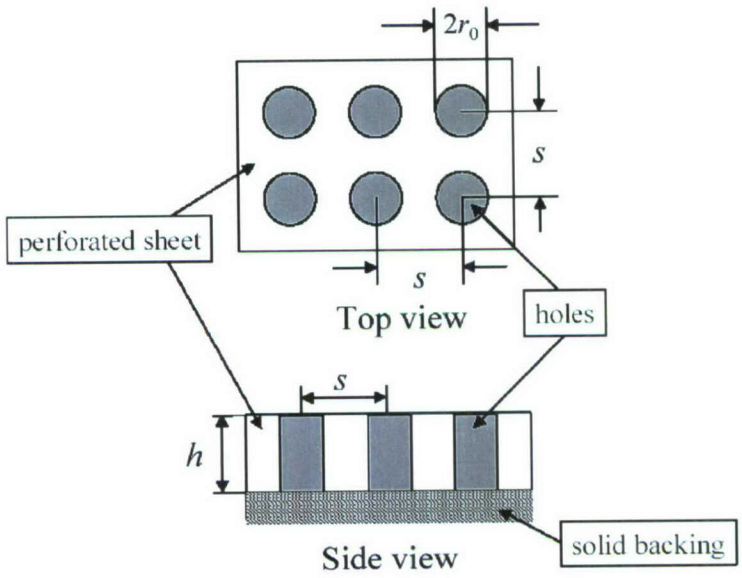

Fig. 1.1 Porous coating of regular microstructure.

To formulate the wall boundary conditions for u and w, one should solve the problem near the pore opening, average the local solution over the UAC surface and establish relationships between $u(0), w(0)$ and other disturbance components. This complicated procedure can be avoided using the following arguments. The second mode is inviscidly unstable and has maximum increments for 2-D waves ($\beta = 0$) [17]. Using 2-D stability equations for inviscid disturbances (in the limit $R \to \infty$) we obtain on the wall surface ($y = 0$)

$$v(0) = -i \frac{T_{sw}}{\omega} p'(0), \tag{1.8}$$

$$u(0) = -\left[i U'_{sw} v(0) + \alpha T_{sw} p(0) \right] / \omega, \tag{1.9}$$

where the subscript "s" denotes the mean-flow quantities, "w" denotes quantities on the wall, and prime denotes the derivative d / dy. The boundary condition (1.8) can be written in the form (1.4).

The viscous effects are essential in the near-wall Stokes layer (where the longitudinal velocity is quickly adjusted to the boundary condition $u(0) = 0$) and in the critical layer located near the critical point $y_c : U_s(y_c) = c$, where $c = \omega / \alpha_r$ is phase speed. To illustrate this feature we consider the compressible Blasius profiles for a flat plate at $M_e = 6.21$ and $T_{sw} = 1$. These parameters typifies local flow over a 7-degree half angle sharp cone at zero angle of attack in the CUBRC LENS I shock tunnel at freestream Mach=7.14 (see Section 2.1.3) The temperature eigenfunction $|\theta(y)|$ of 2-D second-mode wave of frequency $F \equiv \omega^* \nu_e^* / U_e^{*2} = 6 \times 10^{-5}$ is

shown in Fig. 1.2 at $R = 3452.54$, where $y = y^* / \sqrt{\nu_e^* x^* / U_e^*}$. The corresponding eigenvalue is $\alpha = (2.27157\text{E-}1, -8.17745\text{E-}3)$. The vertical line shows the Stokes layer edge that is calculated as

$$\overline{\delta}_s \equiv \delta_s / \sqrt{\nu_e^* x^* / U_e^*} = \sqrt{\nu_w^* / \omega^*} / \sqrt{\nu_e^* x^* / U_e^*} = F^{-1/2} R^{-1} \sqrt{\nu_w^* / \nu_e^*} . \qquad (1.10)$$

In the case considered herein, the wall temperature is $T_w^* = T_e^*$ that gives $\sqrt{\nu_w^* / \nu_e^*} = 1$. The nondimensional thickness of Stokes layer is $\overline{\delta}_s \approx 0.22$. The ratio of $\overline{\delta}_s$ to the disturbance wavelength $\lambda = 2\pi / \alpha_r$ is approximately 0.008; i.e., the Stokes layer is very thin. The phase speed $c \approx 0.91$ gives the critical point $y_c \approx 6.54$ that correlates with the disturbance temperature maximum. The critical layer thickness is of the order of half-width of this maximum, $\overline{\delta}_c \approx 2$, that is about 10 times larger than the Stokes-layer thickness.

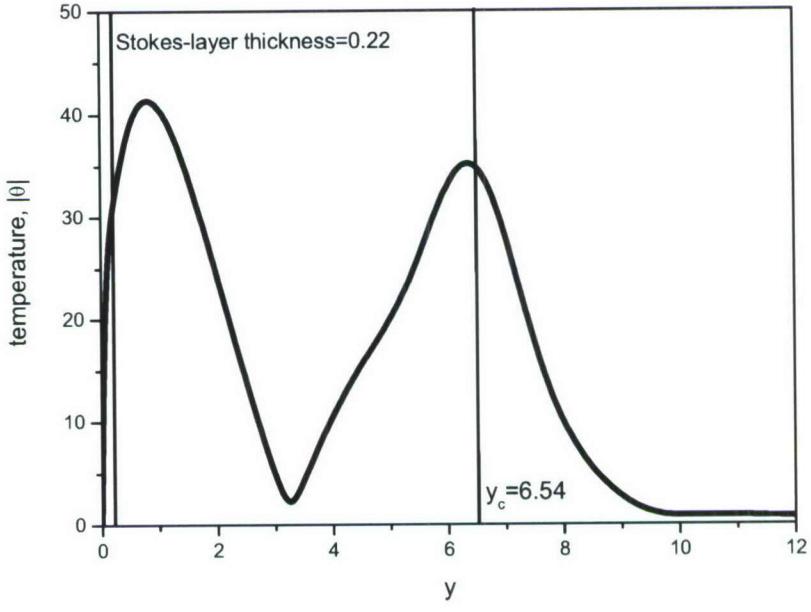

Fig. 1.2 Eigenfunction $|\theta(y)|$ of 2-D second-mode wave, $F = 6 \times 10^{-5}$, $\alpha = (2.27157\text{E-}1, -8.17745\text{E-}3)$, solid wall.

These findings suggest that the viscous effect on second-mode instability is predominately due to the critical layer, while the Stokes layer plays a minor role. To verify this assumption we conduct calculations of the second-mode wave by solving the stability equations (including all viscous terms in order to capture viscous effects in the critical layer) with the inviscid boundary condition (1.9) for $u(0)$ and $v(0) = \theta(0) = 0$. Figure 1.3 shows comparisons of the eigenfunctions calculated with viscous and inviscid boundary conditions at the aforementioned parameters. As expected, these eigenfunctions are almost identical. The eigenvalues are also very close:

$$\alpha_{\text{solid,vis}} = (2.272\text{E-}1, -8.177\text{E-}3), \ \alpha_{\text{solid,invis}} = (2.271\text{E-}1, -8.200\text{E-}3). \qquad (1.11)$$

Discrepancy between $|u(y)|$ is appreciable in the Stokes layer only as shown in the left top panel of Fig. 1.3.

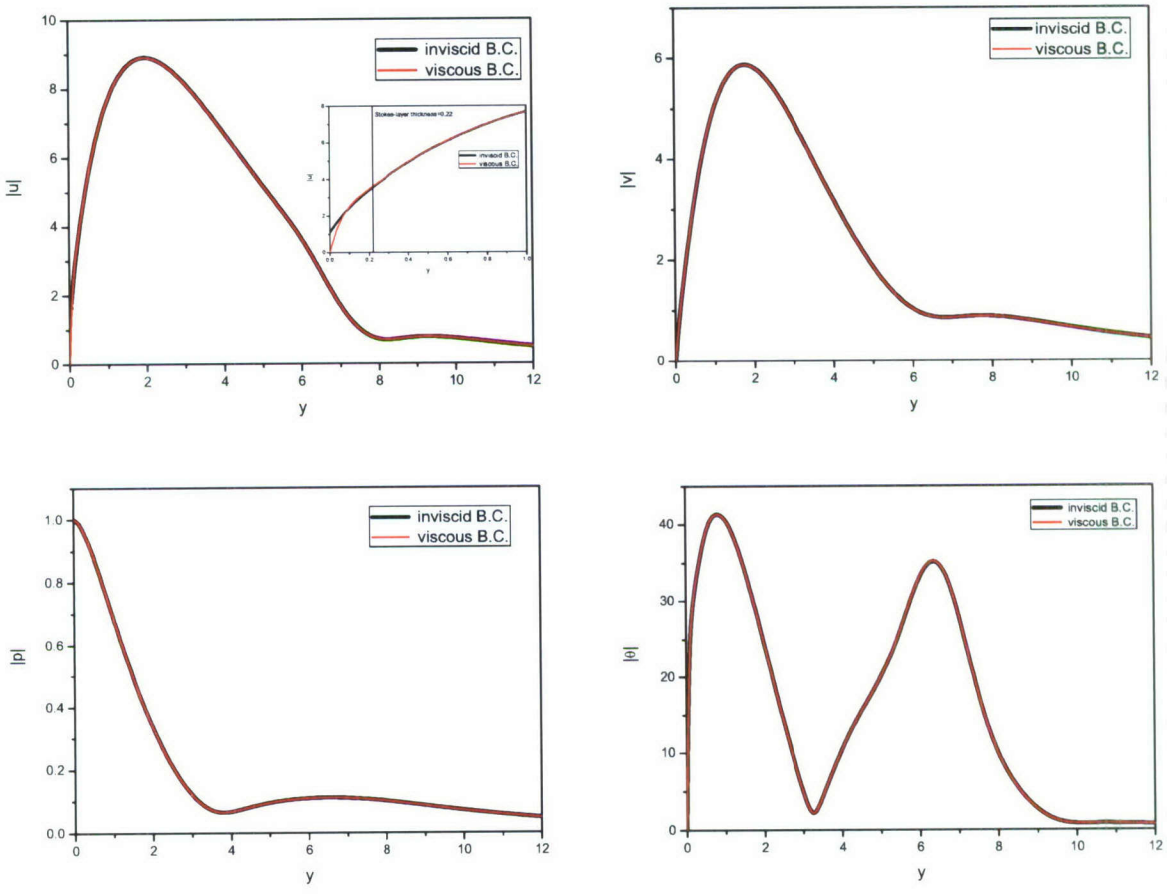

Fig. 1.3 Eigenfunctions of 2-D second-mode wave of frequency $F = 6 \times 10^{-5}$; black lines – inviscid boundary conditions, red lines – viscous boundary conditions; solid wall.

Similar calculations were conducted for the porous wall of $r^* = 25$ μm, $s^* = 100$ μm and $h^* = 300$ μm using:

- Inviscid boundary condition (1.9), and $v(0) = Ap(0)$, $\theta(0) = 0$ (1.12)
- Simplified viscous boundary conditions $u(0) = 0$, $v(0) = Ap(0)$, $\theta(0) = 0$ (1.13)

The boundary conditions (1.9) correspond to the case of maximum slip on the porous surface, while the boundary condition $u(0) = 0$ in (1.13) – to the case of no slip. In reality, the disturbance amplitude $u(0)$ lies somewhere in between. Comparing these extreme cases we can estimate sensitivity of the UAC performance to uncertainty of the boundary condition for u. As in the solid wall case, the eigenvalues for the plate with UAC are close to each other:

$$\alpha_{\text{porous,vis}}=(2.283\text{E-}1,\ -2.689\text{E-}3),\ \alpha_{\text{porous,invis}}=(2.283\text{E-}1,\ -2.671\text{E-}3)$$

The corresponding eigenfunctions $|u(y)|$ are shown in Fig. 1.4. The discrepancy between $|u(y)|$ is appreciable in the Stokes layer only.

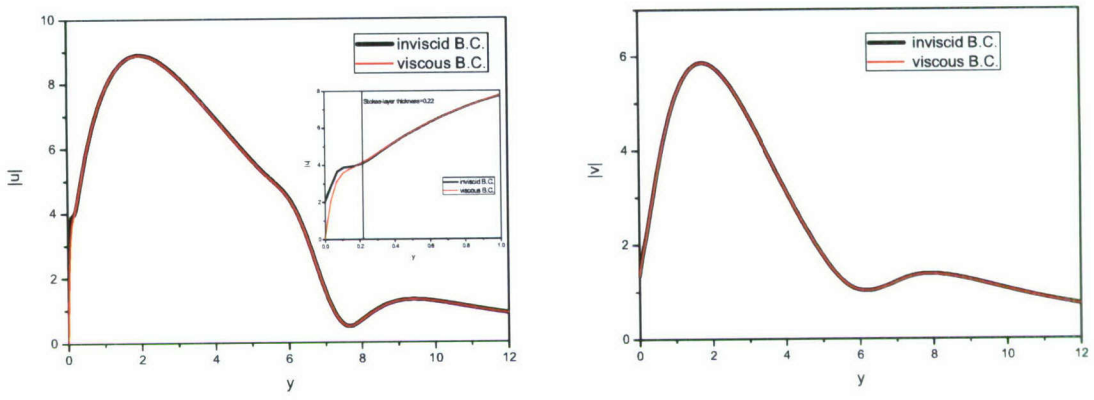

Fig. 1.4 Eigenfunctions of 2-D second-mode wave of frequency $F = 6 \times 10^{-5}$; black lines – inviscid boundary conditions (1.12), red lines – simplified viscous boundary conditions (1.13); porous wall.

The aforementioned analysis leads to the assumption that N-factors on porous and solid walls can be calculated with sufficient accuracy using the inviscid boundary conditions (1.12) or the simplified viscous boundary conditions (1.13). To validate this assumption we carried out calculations of N-factors for a 7° half-angle sharp cone at zero angle of attack at the free-stream parameters corresponding to the CUBRC LENS I shock tunnel: $M_\infty = 7.14$, $T_\infty^* = 231.8\,\mathrm{K}$ [20]. N-factors on the solid surface and on the porous surface with UAC of $r^* = 25$ μm, $s^* = 100$ μm and $h^* = 300$ μm, are shown in Fig. 1.5. The solid lines correspond to the solution obtained with the boundary conditions (1.12), symbols – with the boundary conditions (1.13). As expected, the difference between $N(x)$ is negligible. These findings allow us to conduct further parametric studies of the UAC laminar-flow-control performance using the simplified boundary conditions (1.13) on the porous wall.

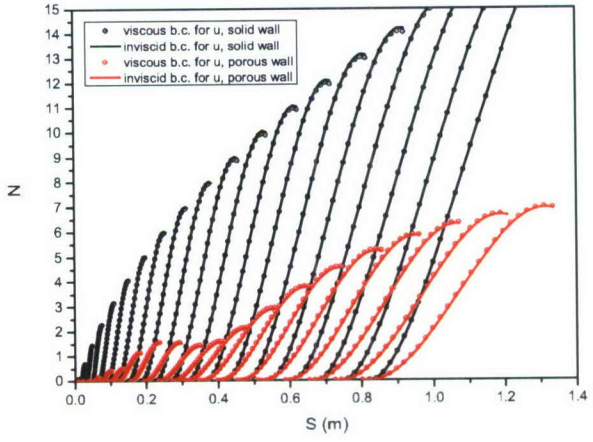

Fig. 1.5 Eigenfunctions of 2-D second-mode wave of frequency $F = 6 \times 10^{-5}$; lines – boundary conditions (1.12), symbols – (1.13), S – longitudinal coordinate measured along the cone surface.

2.1.2. Transition on solid wall and comparison with STABL

To calibrate our stability and transition prediction tools, we analyze transition data of Ref. [20]. Namely, we consider the laminar boundary-layer flow past a sharp 7° half-angle cone at zero angle of attack. The free-stream parameters correspond to Run 22 reported in Table 2 of Ref. [20]: Mach number $\mathrm{M}_\infty = 10.04$, unit Reynolds number $\mathrm{Re}_{1\infty} = 1.92 \times 10^6$ m^{-1}, temperature $T_\infty^* = 198.62$ K. The cone length measured along the cone surface is $L^* = 2.2$ m, and the wall temperature is $T_w^* = 297.28$ K. The local flow parameters (at the upper boundary-layer edge) are determined from the Navier-Stokes solution for laminar flow: $\mathrm{Re}_{1e} = 3.2 \times 10^6$ m^{-1}, $T_w / T_e = 1.03$, $T_e^* = 297.93$ K and $M_e = 8.1$. At these parameters the compressible Blasius solution agrees well with that predicted by the Navier-Stokes solver (Figs. 1.6 and 1.7); i.e., the viscous-inviscid interaction weakly affects the boundary-layer mean flow.

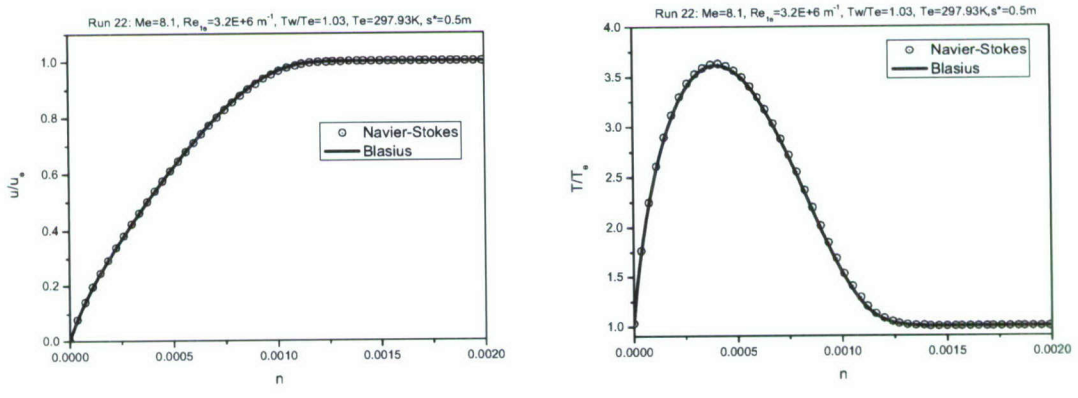

Fig. 1.6 Flow velocity (left) and temperature (right) profiles at the station $S^* = 0.5$ m, here S^* – longitudinal coordinate measured along the cone surface, $n = n^* / L^*$ – coordinate normal to the cone surface.

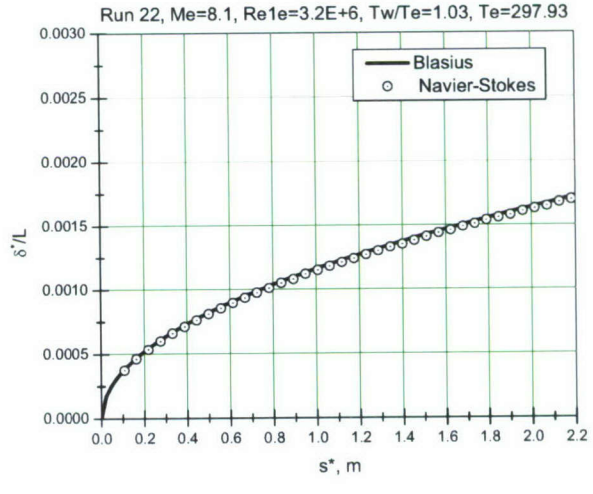

Fig. 1.7 Boundary-layer displacement thickness versus the longitudinal coordinate S^* measured along the cone surface.

Figure 1.8 shows the data scanned from Fig. 7 of Ref. [20]. Symbols correspond to the heat flux measurements on the sharp cone model tested in the CUBRC LENS I shock tunnel (Run 22). The thin black line represents the laminar heat flux distribution predicted by the Navier-Stokes solver of STABL. The green dashed line shows an envelope of N-factors predicted by the PSE solver of STABL. The family of solid black lines shows the amplification factors predicted by our reduced-order computational package that includes the compressible Blasius mean flow and the local-parallel linear stability solver. Strikingly, an envelope of these amplification curves is very close to that predicted by STABL. This opens up an opportunity to conduct quick turn-around parametric computations of the transition onset points and search for optimal UAC parameters appropriate for further experimental and DNS studies.

The critical amplification $N_{tr} = 5.5$ was suggested in Ref. [20] for the CUBRC LENS I shock tunnel (see dashed black line in Fig. 1.9). This value has been used for assessments of the transition locus on porous and solid surfaces.

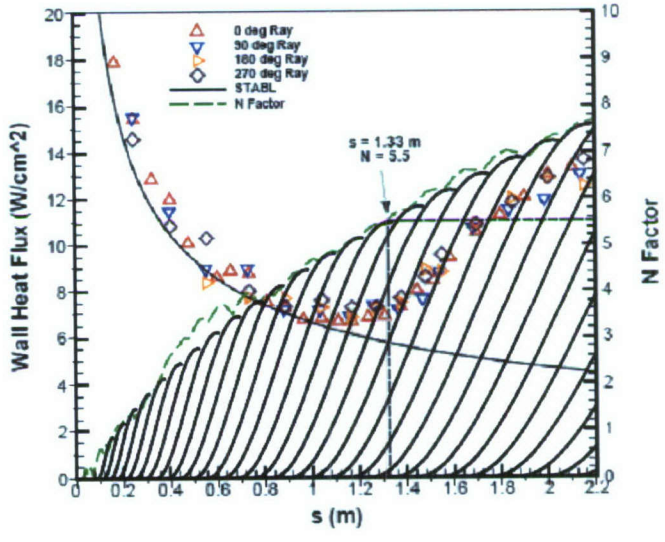

Fig. 1.8 Comparison of N-factors predicted by STABL (dashed green line) with our calculations (family of solid black lines) for Run 22 (sharp cone); symbols – experimental measurements of the wall heat flux, thin black line – laminar heat flux predicted by STABL; S – longitudinal coordinate measured along the cone surface.

2.1.3. Assessments of UAC performance

Parametric calculations of the UAC-LFC performance are carried out for the free-stream conditions of Run 5 (see Table 1 of Ref. [20]): $\mathrm{M}_\infty = 7.14$, $\mathrm{Re}_{1\infty} = 9.76 \times 10^6$ m^{-1}, $T_\infty^* = 231.8$ K, the wall temperature is $T_w^* = 299.3$ K. The cone length (measured along the cone generator) is $L^* = 2.2$ m. The Navier-Stokes solution gives the local parameters: $\mathrm{Re}_{1e} = 14.2 \times 10^6$ m^{-1}, $T_e^* = 299.02$ K, $M_e = 6.21$, and the wall temperature ratio $T_w / T_e = 1$. It is assumed that M_e, T_w / T_e and T_w^* do not change in the range of unit Reynolds number considered hereafter. For a certain value of Re_{1e}, stability calculations are conducted for the second-mode 2-D waves.

Preliminary estimates indicated that the UAC of $r^* = 25$ μm, $s^* = 100$ μm and $h^* = 10r^* = 250$ μm (porosity $\phi = 0.196$) are appropriate for the aforementioned flow conditions. Figures 1.9 and 1.10 show the amplification factors $N(X^*, \omega_j^*)$ for different disturbance frequencies ω_j^* as well as the ratio of the disturbance wavelength to the pore spacing λ^* / s^*. The latter characterizes fineness of the UAC structure. Hereafter, X^* is the longitudinal coordinate measured from the cone tip along the cone surface. The horizontal line in the left plot corresponds to the critical value of $N_{tr} = 5.5$.

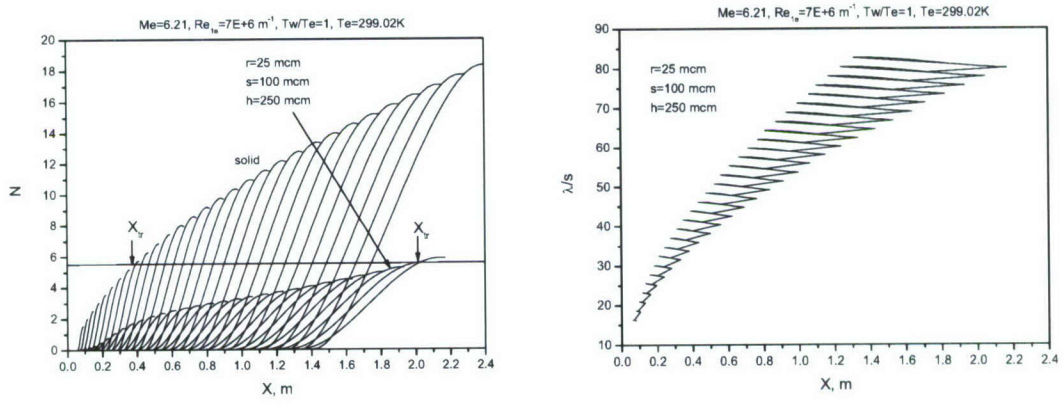

Fig. 1.9 *N*-factors for solid and porous walls (left) and the coating fineness distributions λ^* / s^* (right) along the cone surface, $\mathrm{Re}_{1e} = 7 \times 10^6$ m^{-1}, $\mathrm{M}_\infty = 7.14$.

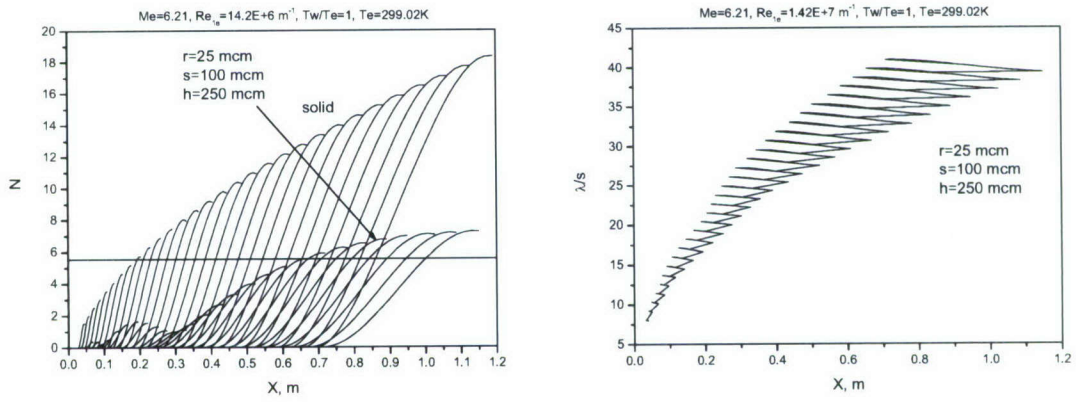

Fig. 1.10 *N*-factors for solid and porous walls (left) and the coating fineness distributions λ^* / s^* (right) along the cone surface, $\mathrm{Re}_{1e} = 14.2 \times 10^6$ m^{-1}, $\mathrm{M}_\infty = 7.14$.

Similar calculations were conducted in the range of local unit Reynolds numbers $2 \times 10^6 \le \mathrm{Re}_{1e} \le 20 \times 10^6$ m^{-1}. Results are summarized in Fig. 1.11, where the transition onset point is shown as a function of Re_{1e} for the solid (black line) and porous (red line) wall. The theory predicts that the UAC strongly stabilizes the second mode and can lead to dramatic (on the order of magnitude) increase of laminar run (see data close to $\mathrm{Re}_{1e} \approx 10^7$ m^{-1}). The UAC performance is not monotonic versus Re_{1e}. Namely, the transition onset point on the porous wall

has a jump at $\mathrm{Re}_{1e} \approx 11.7 \times 10^6$ m^{-1}. This effect is associated with a finite depth h of pores. The disturbances penetrating into a blind hole are reflected by the hole bottom that affects the UAC admittance. As a result, the envelope of amplification curves has modulations (see left plot in Figure 1.10). As the unit Reynolds number increases crossing the value $\mathrm{Re}_{1e} \approx 11.7 \times 10^6$ m^{-1}, the envelope first maximum attains the critical level $N = 5.5$, and the predicted transition onset point jumps toward the cone tip. This trend is illustrated in Figure 1.12, where the amplification curves are shown in the vicinity of this jump.

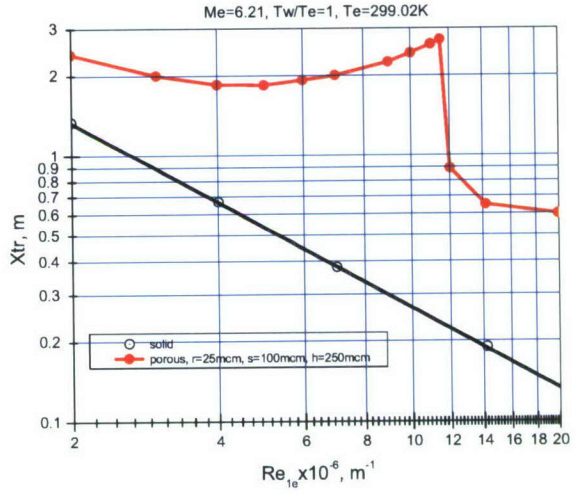

Fig. 1.11 The transition onset point X_{tr} as a function of Re_{1e} for solid (black line with symbols) and porous (red line with symbols) walls, $\mathrm{M}_\infty = 7.14$.

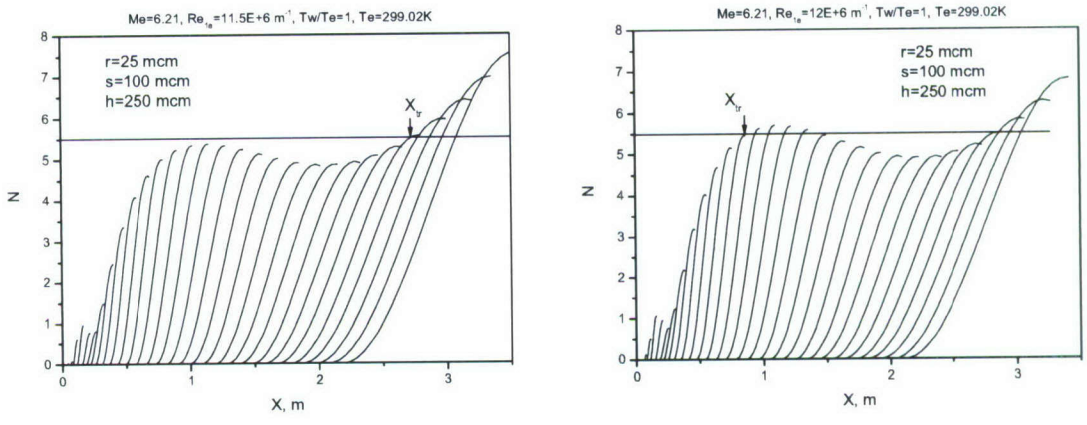

Fig. 1.12 N-factors for porous wall at $\mathrm{Re}_{1e} = 11.5 \times 10^6$ m^{-1} (left) and $\mathrm{Re}_{1e} = 12 \times 10^6$ m^{-1} (right).

The foregoing stability analysis lies in the expectation that the porous surface is aerodynamically smooth in order for the proposed mechanism to effectively delay transition. If this were not the case, then the holes would act as distributed surface roughness and prematurely trip the boundary layer. Unfortunately, data relevant to roughness-induced transition on surfaces with distributed

blind holes are very limited. There is only one set of experimental data obtained by Rasheed et al. [10] in the GALCIT T5 shock tunnel on a 5-degree half-angle sharp cone at zero angle of attack. In these experiments the cone model had a smooth surface over its half and the aforementioned coating over the other half beginning at 148 mm from the cone tip. The UAC had 60 μm diameter holes spaced 100 μm apart in a rectangular grid arrangement resulting in a porosity of 28%. In Ref. [10], the coating roughness is characterized by the Reynolds number

$$\mathrm{Re}_D^* = \frac{\rho^*(T_{ref}^*)U_e^* D^*}{\mu^*(T_{ref}^*)}, \tag{1.14}$$

where $D^* = 2r^*$ is hole diameter, the density ρ^* and viscosity μ^* are calculated at the reference temperature, T_{ref}^*, determined as

$$\frac{T_{ref}^*}{T_e^*} = 0.5 + 0.039M_e^2 + 0.5\frac{T_w^*}{T_e^*}. \tag{1.15}$$

Assuming that the viscosity coefficient is approximated as $\mu^*(T_{ref}^*) = \mu^*(T_e^*)(T_{ref}^* / T_e^*)^{0.75}$ and the density $\rho^*(T_{ref}^*) = \rho^*(T_e^*)T_e^* / T_{ref}^*$, the Reynolds number Re_D^* is

$$\mathrm{Re}_D^* = \mathrm{Re}_{1e}\frac{D^*}{(T_{ref}^* / T_e^*)^{1.75}}. \tag{1.16}$$

The experiment [10] showed that the coating becomes less effective at $\mathrm{Re}_D^* \approx 130$ and prematurely trips the boundary layer at $\mathrm{Re}_D^* > 300$.

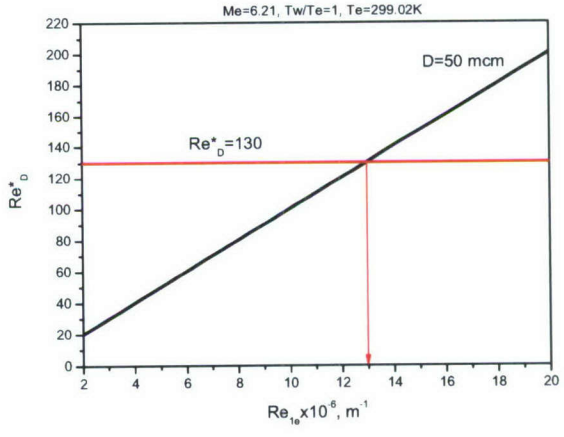

Fig. 1.13 The Reynolds number Re_D^* versus Re_{1e}. The criterion $\mathrm{Re}_D^* = 130$ indicates that UAC can be treated as aerodynamically smooth for $\mathrm{Re}_{1e} < 13\times10^6$ m^{-1} and $\mathrm{M}_\infty = 7.14$.

Since the UAC characteristics [10] are close to those considered herein, we assume that the criterion $\mathrm{Re}_D^* = 130$ can be used for estimates of the UAC roughness effect if the coating begins at a distance $X_0^* > 148$ mm from the cone tip. Figure 1.13 shows Re_D^* as a function of Re_{1e} for the UAC considered herein. The criterion $\mathrm{Re}_D^* = 130$ indicates that the UAC can be treated as aerodynamically smooth for $\mathrm{Re}_{1e} < 13\times10^6$ m^{-1}.

The same porous coating ($r^* = 25$ μm, $s^* = 100$ μm, $h^* = 10r^* = 250$ μm, $\phi = 0.196$) was analyzed for the freestream conditions: $M_\infty = 10.04$, $T_\infty^* = 198.62$ K, and $T_w^* = 297.28$ K relevant to Run 22 of Ref. [20]. The local flow parameters, which were predicted by the Navier-Stokes solver at $\mathrm{Re}_{1\infty} = 1.92 \times 10^6$ m^{-1}, are: $M_e = 8.1$, $T_e^* = 297.93$ K, $T_w / T_e = 1.03$, $\mathrm{Re}_{1e} = 3.2 \times 10^6$ m^{-1}. It is assumed that M_e, T_w / T_e and T_w^* do not change in the range of unit Reynolds number considered hereafter. Figure 1.14 shows the amplification factors $N(X^*, \omega_j^*)$ for different disturbance frequencies ω_j^* as well as the ratio of the disturbance wavelength to the pore spacing λ^* / s^* at $\mathrm{Re}_{\infty 1} = 12 \times 10^6$ m^{-1}. Similar calculations were carried out at various Re_{1e} and summarized in Fig. 1.15.

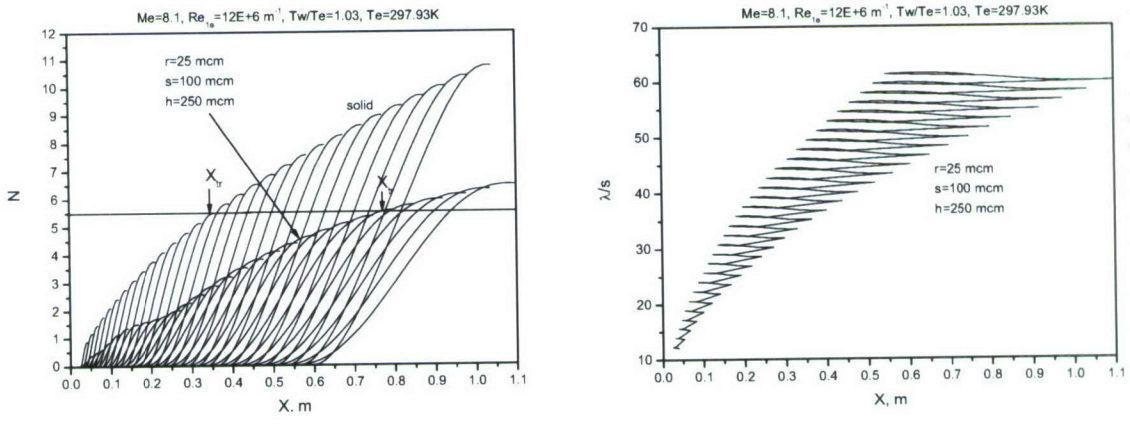

Fig. 1.14 N-factors for solid and porous walls (left) and the coating fineness distributions λ^* / s^* (right) along the cone surface, $\mathrm{Re}_{1e} = 12 \times 10^6$ m^{-1}, $M_\infty = 10.04$.

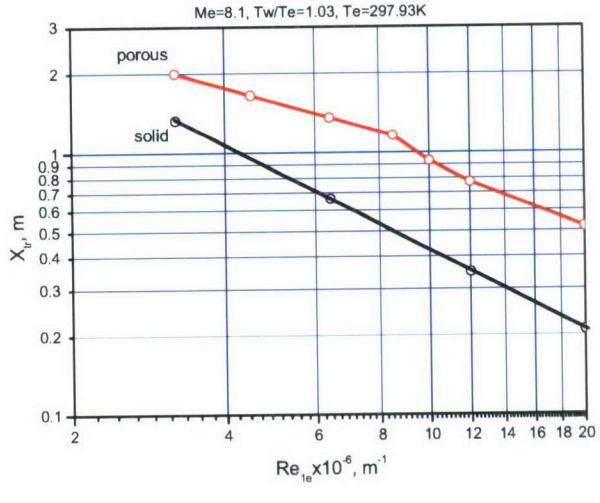

Fig. 1.15 Transition onset point X_{tr} as a function of Re_{1e} for solid (black line with symbols) and porous (red line with symbols) walls, $M_\infty = 10.04$.

Comparing this figure with Fig. 1.11, we conclude that the UAC is less effective than in the Mach=7 case. However, the laminar run increase is still significant. The transition onset point is more than doubled in the range of $8\times10^6 < \mathrm{Re}_{1e} < 20\times10^6$ m^{-1}. For $\mathrm{Re}_{1e} < 8\times10^6$ m^{-1}, the relative pore radius r^*/λ^* becomes small that leads to decreasing of the UAC performance.

The Reynolds number Re_D^* is shown as a function of Re_{1e} in Fig. 1.16. It is seen that Re_D^* does not reach the critical value in the range of $2\times10^6 < \mathrm{Re}_{1e} < 20\times10^6$ m^{-1}; i.e., the coating is aerodynamically smooth in the case of $M_\infty = 10.04$.

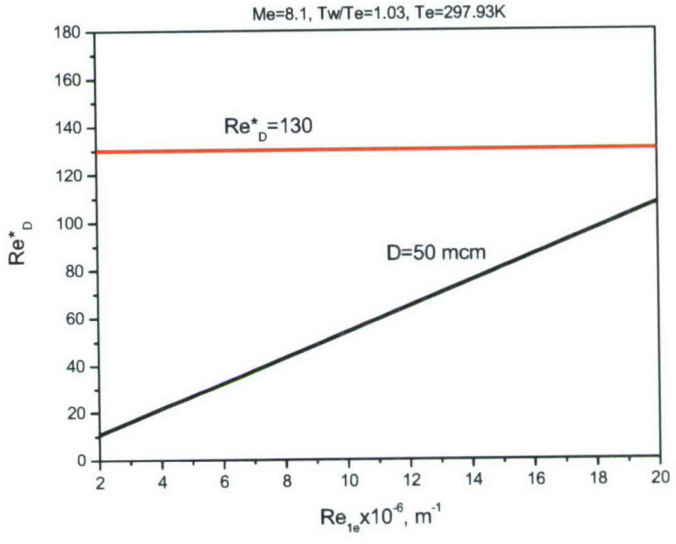

Fig. 1.16 The Reynolds number Re_D^* versus Re_{1e}. The criterion $\mathrm{Re}_D^* = 130$ indicates that the UAC can be treated as aerodynamically smooth in the considered range of Re_{1e}, $M_\infty = 10.04$.

The foregoing calculations indicate that the porous coating of $r^* = 25$ μm, $s^* = 100$ μm and $h^* \approx 10r^*$ is appropriate for testing on a 7-degree half-angle sharp cone in the CUBRC LENS I shock tunnel at free-streams Mach numbers 7 and 10. Because of manufacturing constraints, the UAC thickness is specified as $h^* = 300$ μm ($h^* = 12r^*$). The UAC upstream boundary is placed at the station $X_0^* = 200$ mm. This configuration has been chosen for further consideration.

The transition onset points were calculated at $M_\infty = 7.14$ (Fig. 1.17). For the coating of $h^* = 300$ μm, disturbance reflections from the pore bottoms are weaker than in the case of $h^* = 250$ μm, and the transition onset point varies smoother versus Re_{1e} (compare blue and red curves). At $\mathrm{Re}_{1e} \approx 14\times10^6$ m^{-1}, transition occurs near the coating beginning, $X_0^* = 0.2$ m, the transition onset point jumps toward the cone tip and corresponds to the solid wall case. Similar calculations were conducted for $M_\infty = 10.04$ (Fig. 1.18).

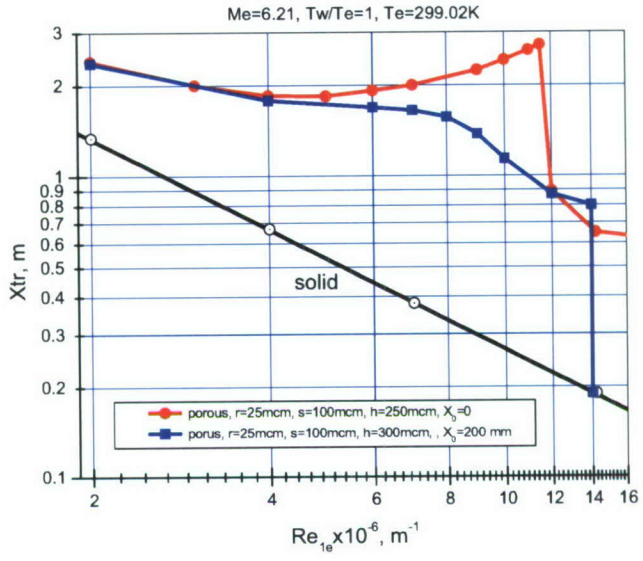

Fig. 1.17 Transition onset point as a function of Re_{1e} for solid and porous walls, $M_\infty = 7.14$.

The foregoing assessments indicate that for experiments at Mach=7 the cone length should be at least 3 m to capture transition on the coated surface in the unit Reynolds number range of $2\times10^6 < \mathrm{Re}_{1e} < 12\times10^6\ \mathrm{m}^{-1}$ (this range corresponds to $4.5\times10^6 < \mathrm{Re}_{1\infty} < 27\times10^6\ \mathrm{ft}^{-1}$). For experiments at Mach=10, the cone length should be larger than 2 m to capture transition on the coated surface in the range of $4\times10^6 < \mathrm{Re}_{1e} < 20\times10^6\ \mathrm{m}^{-1}$ ($7.9\times10^6 < \mathrm{Re}_{1\infty} < 3.9\times10^7\ \mathrm{ft}^{-1}$). In accord with data shown in Fig. 1.19, these ranges of $\mathrm{Re}_{1\infty}$ are achievable in the CUBRC LENS I shock tunnel.

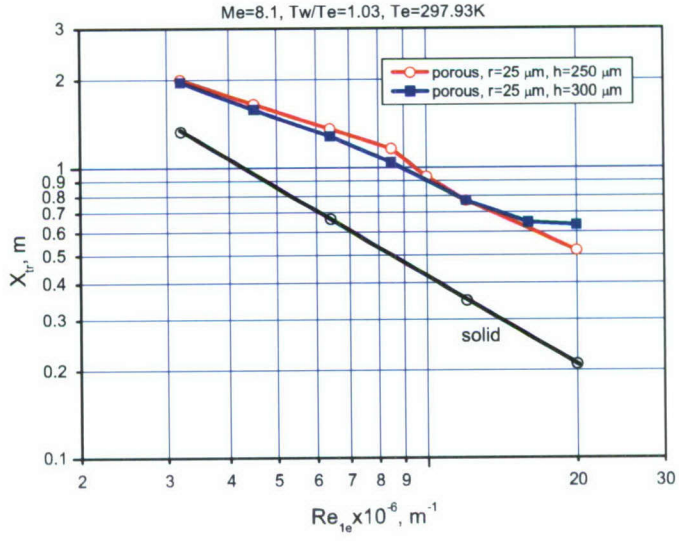

Fig. 1.18 Transition onset point as a function of Re_{1e} for solid and porous walls, $\mathrm{M}_\infty = 10.04$.

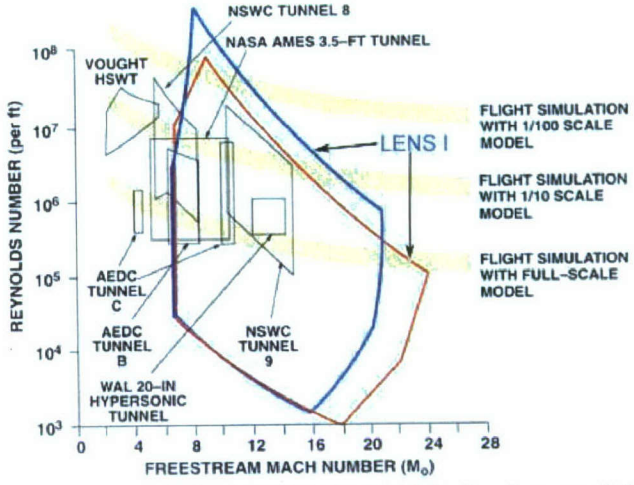

Fig. 1.19 Free-stream parameters of the CUBRC LENS I shock tunnel (scanned from [20]).

2.1.5. Porosity effect

Apparently the UAC-LFC performance increases with porosity ϕ. Figure 1.20 illustrates this trend for the coating of $r^* = 25$ μm and $h^* = 300$ μm. With decreasing the pore spacing from $s^* = 100\,\mu\text{m}$ ($\phi = 0.196$) to $s^* = 75\,\mu\text{m}$ ($\phi = 0.35$), the predicted transition onset point increases from 1.25 m to 1.97 m.

For the UAC configuration shown in Fig. 1.1, the theoretical maximum $\phi = \pi/4 = 0.785$ corresponds to the minimal spacing $s^* = 2r^*$. More promising are configurations schematically shown in Fig. 1.21. For the square-rectangular or honeycomb patterns, it is feasible to fabricate coatings with porosity 70-90%.

In the theoretical model applied herein, the interaction between holes is neglected. Apparently, this interaction needs to be modeled especially for UAC of high porosity which comprises closely spaced holes depicted in Fig. 1.21. The structural constraints to these coatings should be formulated and verified experimentally.

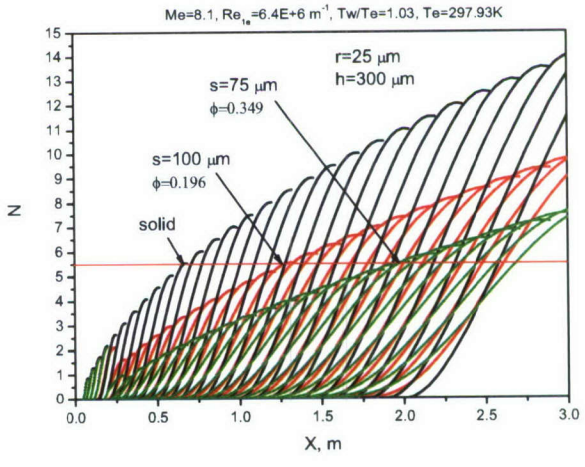

Fig. 1.20 Porosity effect on the UAC-LFC performance, $\text{Re}_{1e} = 6.4 \times 10^6$ m^{-1}, $M_\infty = 10.04$.

Square/rectangular pattern

$$\phi = \frac{D^2}{s^2}$$

Honeycomb pattern

$$\phi \equiv 3\frac{a^2}{s^2} = \frac{D^2}{s^2}$$

Fig. 1.21 Porosity of different UAC patterns, pore cross-sections are grey.

2.2. Numerical simulation of UAC stabilization effect

In Section 2.1, stability calculations were carried out using LST of the local-parallel or weakly nonparallel approximation. The mean flow was approximated by self-similar (compressible Blasius) solutions for a flat plate or sharp cone; i.e., the viscous-inviscid interaction was neglected. Nonuniformity of the boundary conditions due to UAC end effects associated with the upstream and downstream junctures between coated and uncoated surfaces was not considered. Interaction of external disturbances (acoustic, vorticity and entropy waves) with the porous surface was not analyzed. These aspects are addressed hereafter using direct numerical simulation (DNS).

2.2.1. Flat plate

2-D DNS is carried out for hypersonic flow over a flat plate with sharp leading edge at the free-stream Mach number $M_\infty = 6$ and the Reynolds number $\mathrm{Re}_\infty = \rho_\infty^* U_\infty^* L^* / \mu_\infty^* = 2 \times 10^6$. Here ρ_∞^* – free-stream density, U_∞^* – free-stream velocity, L^* – plate length, asterisks denote dimensional variables. Flow variables are made nondimensional using undisturbed freestream parameters: $(u, v) = (u^*, v^*) / U_\infty^*$ – velocity components, $p = p^* / (\rho_\infty^* u_\infty^{*2})$ – pressure, $\rho = \rho / \rho_\infty^*$ – density, $T = T^* / T_\infty^*$ – temperature. Dimensionless coordinates and time are $(x, y) = (x^*, y^*) / L^*$, $t = t^* U_\infty^* / L^*$. The fluid is a perfect gas with specific heat ratio $\gamma = 1.4$ and Prandtl number $\mathrm{Pr} = 0.72$. The viscosity-temperature dependence is approximated by the power law $\mu^* / \mu_\infty^* = (T^* / T_\infty^*)^{0.7}$, the second viscosity is assumed to be zero.

The computational domain is a rectangle (Fig. 2.1) with its bottom side being on the plate surface. For the solid wall case, the no-slip boundary conditions $(u, v) = 0$ are imposed on the plate surface. The wall temperature corresponds to the adiabatic condition $\partial T_w / \partial n = 0$ for the steady-state solution. On the outflow boundary, unknown variables u, v, p, T are extrapolated using the linear approximation to minimize upstream effects of this boundary on the disturbance field. On the inflow and upper boundaries, the boundary conditions correspond to the free stream. Details on the problem formulation and governing equations are discussed in Ref. [21].

The problem is solved in two steps. Firstly, the steady-state solution is calculated to provide the mean flow field. Then, unsteady disturbances are activated on some boundaries of the

computational domain at the initial time instance and the unsteady problem is integrated. Numerical solutions are obtained using the fully implicit second-order finite-volume method described in Ref. [21]. Two-dimensional Navier-Stokes equations are approximated by the conservative TVD shock-capturing scheme. This is of particular importance for simulation of receptivity processes in which free-stream disturbances pass through the shock and induce its oscillations. Moreover, the shock-capturing scheme allows for simulation of the disturbance dynamics in the leading-edge vicinity, where receptivity to free-stream disturbances is most pronounced. The computational grid has 1501×201 nodes. The grid nodes are clustered in the boundary layer and in the leading-edge region.

The steady pressure field (Fig. 2.1) indicates that the viscous-inviscid interaction between the boundary layer and the free stream causes a shock wave emanating from the plate leading edge. However, comparison of the mean-flow solution with the self-similar (compressible Blasius) solution demonstrated a good agreement between them besides small nose region where viscous-inviscid interaction is appreciable [21].

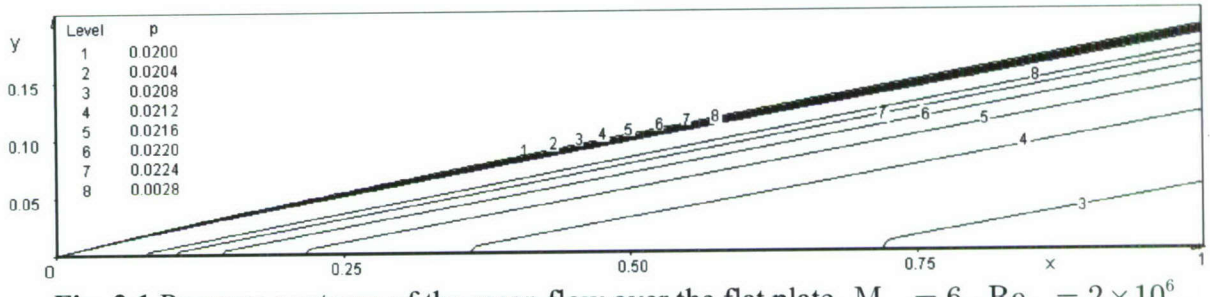

Fig. 2.1 Pressure contours of the mean flow over the flat plate, $\mathrm{M}_\infty = 6$, $\mathrm{Re}_\infty = 2 \times 10^6$.

For modeling of the boundary-layer instability, initial disturbances are induced by local periodic suction-blowing in the leading-edge vicinity. The mass flow on the plate surface is specified as

$$q_w(x,t) = \frac{\rho_w^* v_w^*}{\rho_\infty^* U_\infty^*} = \varepsilon \sin\left(2\pi \frac{x - x_1}{x_2 - x_1}\right) \sin(\omega t), \quad x_1 \le x \le x_2, \quad t > 0, \tag{2.1}$$

where ε is forcing amplitude; $x_1 = 0.0358$, $x_2 = 0.0495$ are boundaries of the local suction-blowing region; $\omega = \omega^* L^* / U_\infty^* = 260$ is angular frequency that corresponds to the frequency parameter $F = \omega / \mathrm{Re} = 1.3 \times 10^{-4}$. The amplitude $\varepsilon = 6 \times 10^{-4}$ was chosen small enough to ensure validity of the linear approximation and compare DNS results with linear stability theory (LST). In the unsteady problem, the wall temperature corresponds to the undisturbed adiabatic temperature, $T_w(x,t) = T_{ad}(x)$; i.e., the temperature disturbances on the wall are zero.

For modeling of the UAC effect, the boundary condition on the porous wall is formulated using the analytical relation (1.4) that couples the vertical velocity disturbance with the pressure disturbance. In terms of real variables, this relation is written as

$$v_{w,n}(x,t) = p_w'(x,t)\,\mathrm{Real}(A) - \frac{1}{\omega}\frac{\partial}{\partial t}\left(p_w'(x,t)\right)\mathrm{Imag}(A), \tag{2.2}$$

where $p_w'(x,t) = p_w(x,t) - p_w(x,0)$ is pressure disturbance on the plate surface. The boundary conditions for disturbances of streamwise velocity and temperature are $u'(x,0) = T'(x,0) = 0$. For

numerical integration, the time derivative of pressure disturbance in (2.2) is approximated with the second order. The porous coating admittance A is calculated using (1.6) and (1.7).

The porous coating has a regular microstructure (Figure 1.1) with the nondimensional pore radius $r_0 = 0.333 \times 10^{-3}$, and the porous layer thickness $h = 5.5 \times 10^{-2}$. The UAC boundary condition (2.2) is imposed in the region $x > 0.3$. Calculations are carried out for porosities $\phi = \pi/9$, $\pi/16$, which correspond to the pore spacing $s = 3r_0$ and $4r_0$, respectively. The UAC parameters are chosen so that the number of pores per the disturbance wavelength is approximately 20 in the case of $s = 3r_0$ and 15 in the case of $s = 4r_0$. Note that the second-mode disturbance wavelength is $\lambda \approx 0.02$ at the frequency $\omega = 260$. It is assumed that the porous surface is aerodynamically smooth and the pore end effects are negligible.

In the case of $\phi = \pi/16$, the pressure-disturbance distributions along the solid (Fig. 2.2a) and porous (Fig. 2.2b) walls agree satisfactory with LST in the region where the second mode dominates. The porous coating leads to significant decreasing of the disturbance amplification. In Fig. 2.3, the pressure-disturbance amplitude on the solid wall (curve 1) is compared with that on the porous wall with $\phi = \pi/16$ (curve 2) and $\phi = \pi/9$ (curve 4). Apparently, the UAC stabilization effect increases with porosity. In the region $x < 0.45$, which is upstream from the instability onset point, the UAC weakly affects the boundary-layer disturbances. The maximum effect is observed in the unstable region; i.e., the porous coating reduces the second-mode growth rate.

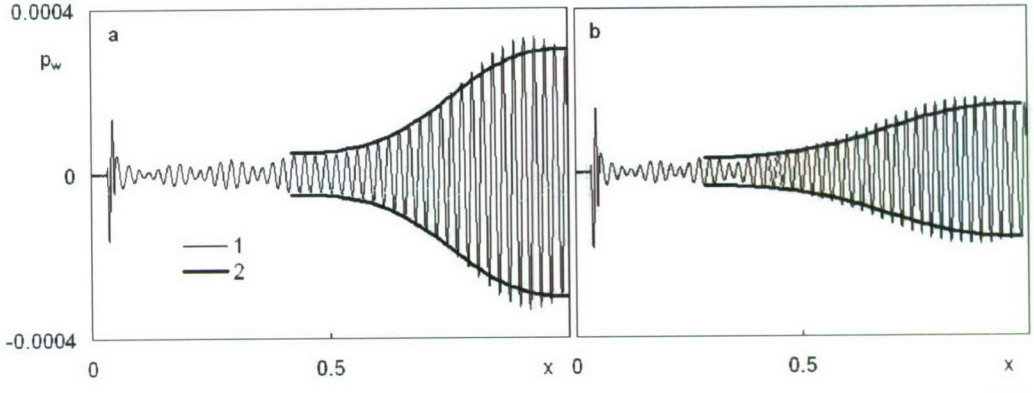

Fig. 2.2 Pressure disturbances on solid (a) and porous (b) wall: 1 – DNS, 2 – LST.

To estimate the UAC end effects associated with the upstream and downstream junctures between the solid and porous surfaces, we carried out calculations for a piecewise coating. The boundary condition (2.2) corresponding to the porous wall of $\phi = \pi/16$ is imposed in the strips: $0.3 < x < 0.4$, $0.5 < x < 0.6$, $0.7 < x < 0.8$ and $0.9 < x \leq 1$, while the remaining surface part is considered to be solid (except for the narrow suction-blowing region). In this case, the pressure disturbance amplitude (curve 3 in Fig. 2.3) oscillates between the curves 1 and 2 corresponding to the solid and porous walls respectively. In the intervals $\Delta x \approx 0.1$, the amplitude increases to the solid-wall level and decreases to the porous-wall level with approximately the same rate. The relaxation length in both directions is approximately $\Delta x_r \approx 0.05$ that is 2-3 wavelength of the second mode. These numerical data indicate that the considered end effects are quite local and can be neglected in calculations of the integral UAC performance.

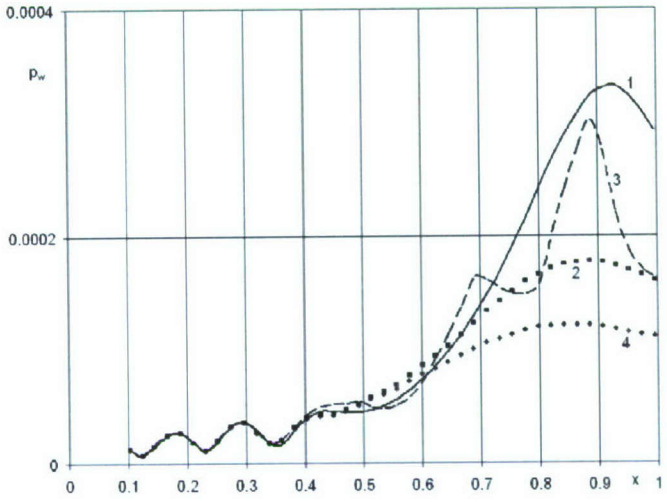

Fig. 2.3 Pressure disturbance amplitudes on the wall: 1 – solid 2 – porous wall with $\phi = \pi/16$, 3 – porous wall with $\phi = \pi/9$, 4 – piecewise porous wall with $\phi = \pi/16$.

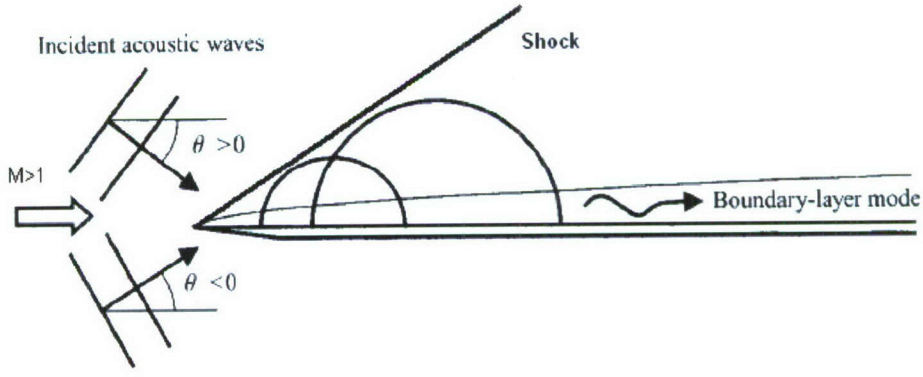

Fig. 2.4 Schematics of receptivity to free-stream acoustic waves interacting with supersonic flow over the flat plate.

For modeling of receptivity to acoustic disturbances, a plain monochromatic acoustic wave is imposed on the steady-state free stream (Fig. 2.4)

$$\left(u', v', p', T'\right)_\infty^T = \left(\left|u'\right|, \left|v'\right|, \left|p'\right|, \left|T'\right|\right)_\infty^T \exp\left[i\left(k_x x + k_y y - \omega t\right)\right]. \tag{2.3}$$

Here $\left|u'\right|$, $\left|v'\right|$, $\left|p'\right|$, $\left|T'\right|$ are dimensionless amplitudes

$$\begin{aligned} &\left|p'\right| = \varepsilon, \quad \left|u'\right| = \pm M_\infty \left|p'\right| \cos\theta, \\ &\left|v'\right| = \mp M_\infty \left|p'\right| \sin\theta, \quad \left|T'\right| = (\gamma - 1) M_\infty^2 \left|p'\right|, \end{aligned} \tag{2.4}$$

θ is angle of incidence that is positive (negative) if the acoustic wave radiates the plate from above (below); ε is pressure amplitude of the incident acoustic wave; $k_x = k_\infty \cos\theta$, $k_y = -k_\infty \sin\theta$ are wavenumber components expressed as

$k_\infty = \omega M_\infty / (M_\infty \cos\theta \pm 1)$. In (2.4), the upper (lower) sign corresponds to the fast (slow) acoustic wave. If the angle of incidence is zero, $\theta = 0°$, then

$$k_x = k_\infty,\ k_y = 0,\ |u'| = \pm M_\infty |p'|,\ |v'| = 0,\ |p'| = \varepsilon,\ |T'| = (\gamma - 1) M_\infty^2 |p'|. \qquad (2.5)$$

For positive angles of incidence (radiation from above), the relations (2.4) are imposed on the inflow and upper boundaries. For negative angles (radiation from below), the acoustic wave is specified on the inflow boundary whereas soft boundary conditions are imposed on the upper boundary.

Herein we consider acoustic waves of small amplitude $\varepsilon = 5 \times 10^{-5}$ at which the receptivity process is linear. The disturbance angular frequency is $\omega = 260$. In the solid wall case, the foregoing receptivity problem was considered in Ref. [22] for fast and slow acoustic waves of various angles of incidence. Herein we study the UAC effect on the receptivity process with imposing the boundary condition (2.2) in the region $x > 0.1$. Calculations have been performed for porosity $\phi = \pi / 16$. The following cases have been considered: fast and slow acoustic waves of $\theta = 0°$, and fast acoustic wave of $\theta = +45°$.

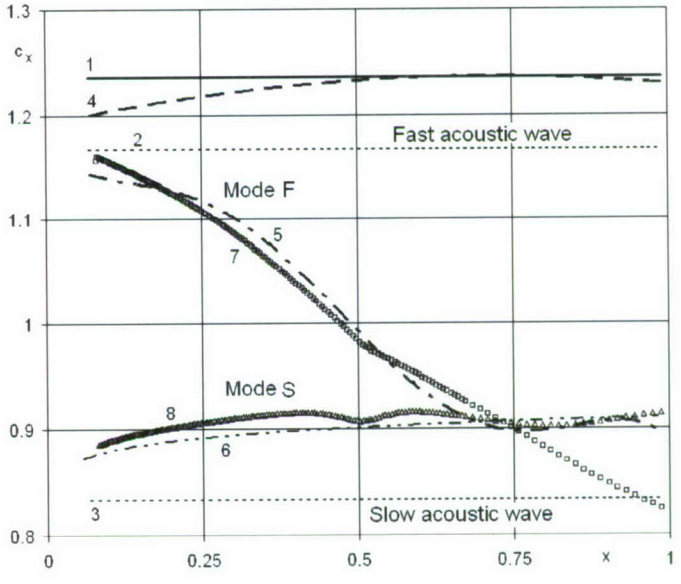

Fig. 2.5 Phase speeds diagram: 1 – fast acoustic wave of $\theta = 45°$, 2 – fast acoustic wave of $\theta = 0°$, 3 – slow acoustic wave of $\theta = 0°$, 4 – disturbances induced by fast acoustic wave of $\theta = 45°$, 5 – disturbances induced by fast acoustic wave of $\theta = 0°$ (DNS), 6 – disturbances induced by slow acoustic wave of $\theta = 0°$ (DNS), 7 – disturbances induced by fast acoustic wave of $\theta = 0°$ (LST), 8 – disturbances induced by slow acoustic wave of $\theta = 0°$ (LST).

The phase speed diagram $c_x(x)$ for different types of disturbances is presented in Fig. 2.5. Curves 2 and 3 show the lower bound ($c_x = 1 + 1/M_\infty$) for fast acoustic waves and the upper bound ($c_x = 1 - 1/M_\infty$) for slow acoustic waves, respectively. These bounds correspond to zero angle of incidence $\theta = 0°$. Curves 7 and 8 show phase speeds of the modes F and S predicted by LST. This terminology was proposed by Fedorov [23] in connection with asymptotic behavior of the mode phase speed in the leading-edge vicinity. Namely, the phase speed of the mode F (fast

mode) tends to the phase speed $c_x = 1 + 1/M_\infty$ of fast acoustic wave whereas the phase speed of the mode S (slow mode) tends to $c_x = 1 - 1/M_\infty$ of slow acoustic wave as $x \to 0$. As contrasted to the terminology of Mack [17], the terminology [23] allows for unambiguous definition of the boundary-layer modes at hypersonic speeds. This issue is also discussed by Forgoston and Tumin [24]. In the considered boundary layer, the mode S corresponds to the Mack first mode upstream from the synchronization point ($x \approx 0.7$ where the two modes have equal phase speeds), and to the Mack second mode downstream from this point.

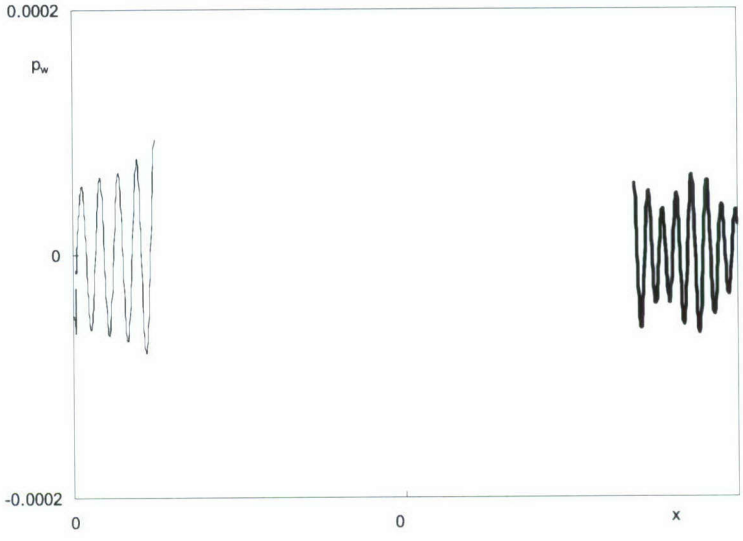

Fig. 2.6 Wall-pressure disturbances in the case of fast acoustic wave of $\theta = 0°$: 1 – solid, 2 – porous wall with $\phi = \pi/16$.

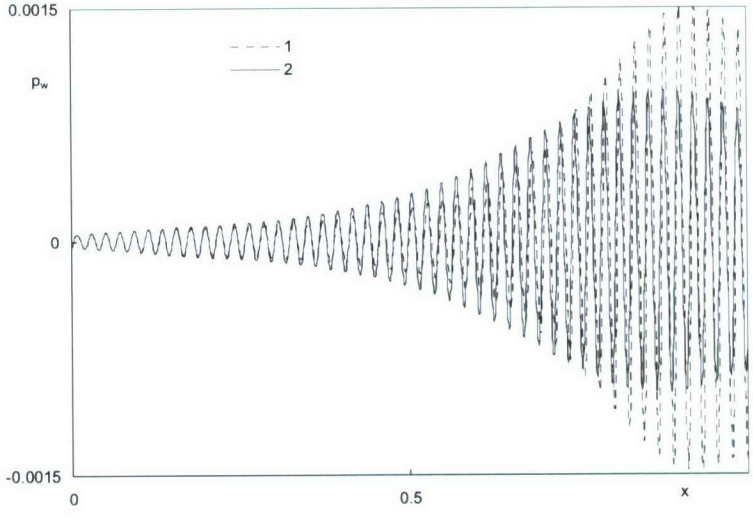

Fig. 2.7 Wall pressure disturbances in the case of slow acoustic wave of $\theta = 0°$: 1 – solid wall, 2 – porous wall with $\phi = \pi/16$.

Note that LST results shown in Fig. 2.5 were obtained using the self-similar (compressible Blasius) solution for the mean flow. This solution was calculated with mean-flow parameters at the upper boundary-layer edge taken from the Navier-Stokes steady-state solution. The phase

speeds of disturbances predicted by DNS are approximately calculated using the wall pressure disturbance distribution $p_w(x)$. Namely, the phase speed is $c_x(x) \approx \omega \Delta x / \pi$, where Δx – distance between zeros of the function $p_w(x)$.

The wall pressure disturbances are shown in the Fig. 2.6 for the case of fast acoustic wave of $\theta = 0°$. Curve 1 corresponds to the solid wall, curve 2 – to the porous wall. The disturbance phase speed is shown in Fig. 2.5 (curve 5). The porous coating leads to decreasing of the mode F amplitude in the leading edge region $0 < x < 0.4$. As a result, the disturbance amplitude in the synchronization region ($0.6 < x < 0.7$) is noticeably lower than in the solid wall case. In the region where the mode S dominates ($x > 0.7$), disturbances on the porous wall virtually do not amplify due to the UAC stabilization effect. Note that UAC slightly affects the disturbance phase speeds and does not change the synchronization conditions. Comparison of the disturbance field patterns (not shown here) indicates that the UAC weakly affects acoustic fields.

Figure 2.7 shows the wall pressure disturbances for the case of slow acoustic wave with $\theta = 0°$ (curve 6 in Fig. 2.5 shows the corresponding phase speed). Curves 1 and 2 in Fig. 2.7 are relevant to the solid and porous walls, respectively. The LST and experiments [11, 12] revealed that UAC stabilizes the second mode and slightly destabilizes the first mode. Hence, the mode S should be less stable in the region $x < 0.6$ and more stable in the region $x > 0.7$. Exactly the same behavior is predicted by DNS.

To illuminate the UAC effect on acoustic disturbances, calculations were performed for the fast acoustic wave of $\theta = +45°$. Since this wave does not synchronized with the modes F and S, there is no appreciable excitation of unstable disturbances in the boundary layer. The phase speed predicted by DNS (curve 4 in Fig. 2.5) remains approximately equal to the phase speed of incident acoustic wave (curves 1 in Fig. 2.5). Comparing the disturbance distributions on the solid and porous walls (Fig. 2.8, curves 1 and 2) we conclude, that the UAC weakly affects the interaction of considered acoustic wave with the boundary layer flow.

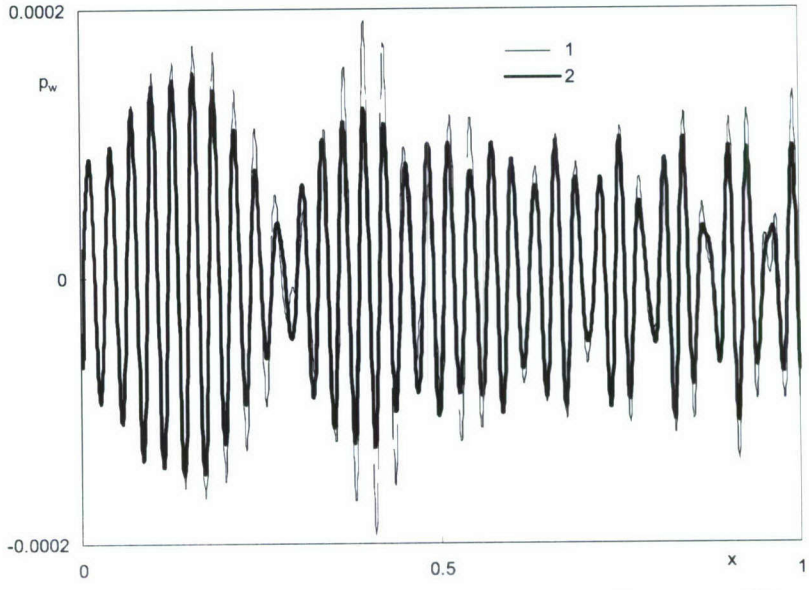

Fig. 2.8 The wall-pressure disturbances in the case of fast acoustic wave of $\theta = +45°$: 1 – solid, 2 – porous wall with $\phi = \pi / 16$.

2.2.2. Sharp cone

DNS of disturbances in the boundary layer flow over a sharp cone of apex half-angle 7° has been carried out for the flow parameters corresponding to the experiments [11,12], which were performed in the ITAM T-326 wind tunnel at the free-stream Mach number $M_\infty = 5.95$, stagnation temperature $T_0^* = 385 \div 400$ K, wall temperature $T_w^* = (0.80 \div 0.84) T_0^*$, and angle of attack $0 \pm 0.05^\circ$. In these experiments, besides propagation of natural disturbances, artificially excited wave-packets of frequency $f^* = 275$ kHz (relevant to the second mode) were studied. In all cases the maximum amplitude was observed at the transversal wave number $\beta = 0$. This indicates that 2-D (axisymmetric) waves of second mode were dominant. To investigate the UAC effect, a half of cone surface was covered by a perforated sheet schematically shown in Fig. 1.1. The sheet thickness was $450\,\mu$m, pores were slightly conical with the diameter $50 \pm 6\,\mu$m on the front side and $64 \pm 6\,\mu$m on the back side. Spacing between pores, $s = 100 \pm 4\,\mu$m, corresponds to the porosity $\phi \approx 0.2$. The UAC was placed downstream from the station $x = 182$ mm.

The computational domain is a rectangle (Fig. 2.9) with its bottom side being on the cone surface. For the solid wall case, no-slip boundary conditions are imposed on the cone surface. The computational grid has 4001×151 nodes with clustering in the boundary-layer and nose-tip regions.

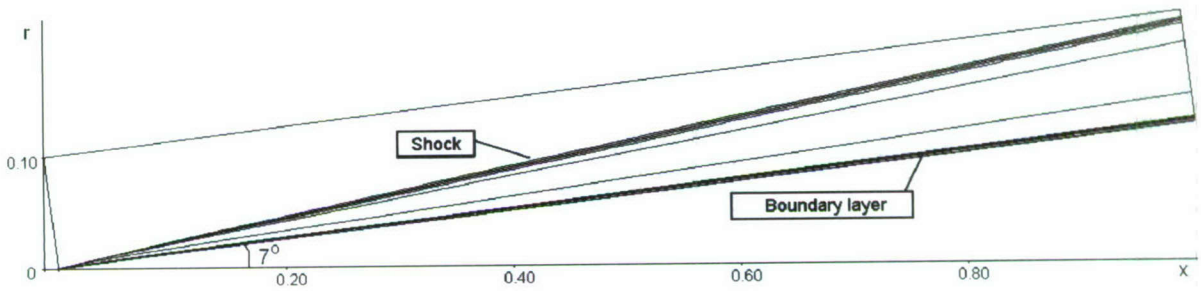

Fig. 2.9 Density contours of mean flow over a sharp cone, $\mathrm{M}_\infty = 5.95$, $\mathrm{Re}_\infty = 4.2 \times 10^6$.

The steady-state flow field was calculated for the free-stream parameters: $M_\infty = 5.95$, $\mathrm{Re}_\infty = 4.2 \times 10^6$, the cone length is $L^* = 350$ mm, $T_w = 6.626$ ($T_0^* = 390$ K, $T_w^* = 0.82 T_0^*$), $T_\infty^* = 48.26$ K, $\gamma = 1.4$, Pr=0.72. The density contours, shown in Fig. 2.9, visualize the boundary-layer region and the shock wave forming near the cone tip. The boundary layer characteristics agree well with the experimental data and the self-similar solution (Figs. 2.10 and 2.11) in the considered x-stations.

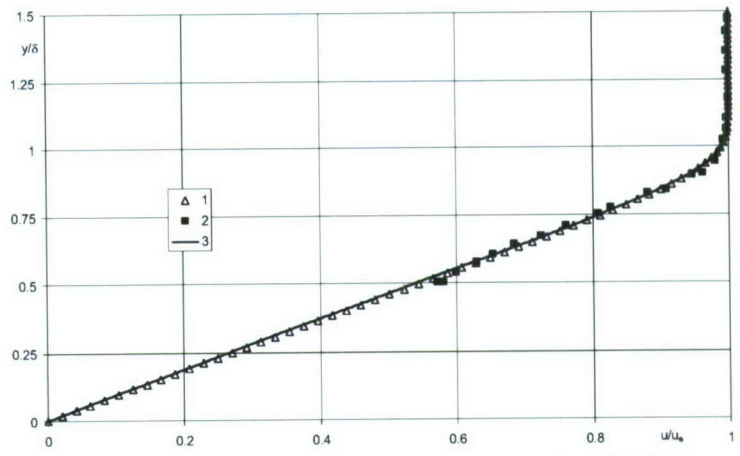

Fig. 2.10 Velocity profile in the boundary layer at $x = 0.41$: 1 – DNS, 2 – experiment, 3 – self-similar solution; y is normalized to the boundary-layer thickness δ determined as $u(\delta)/u_e = 0.99$.

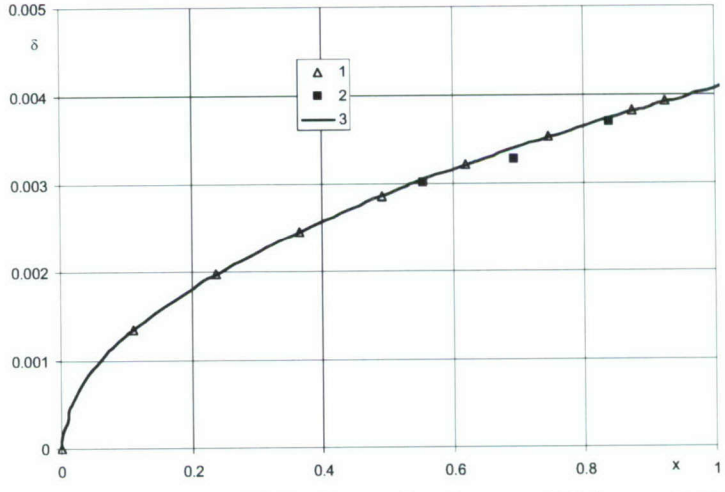

Fig. 2.11 Boundary layer thickness $\delta(x)$ determined as $u(\delta)/u_e = 0.99$: 1 – DNS, 2 – experiment, 3 – self-similar solution.

A local periodic suction-blowing was introduced into the flow using the boundary condition (2.1), where $\varepsilon = 5 \times 10^{-4}$ is small enough to meet the LST restriction, $x_1 = 0.1971$, $x_2 = 0.2108$, $\omega = 727.75$ corresponds to the frequency $f^* = 275$ kHz actuated in the experiments [11, 12]. Disturbances of this frequency are associated with the second-mode instability.

For $x > 0.55$, the boundary-layer mode starts to grow downstream. This is illustrated by the wall pressure disturbance shown in Fig. 2.12 at a fixed time moment. Detailed snapshots of unstable disturbances are presented in Fig. 2.13 (pressure) and Fig. 2.14 (density) in the region $0.87 \le x \le 0.9675$. Two-cell structures in the boundary layer (Fig. 2.13) typify the second mode wave [21]. Their longitudinal wavelength is approximately 2δ in accord with the experimental observations [25-27]. Near the upper boundary-layer edge (in the critical layer where the disturbance phase speed is close to the mean-flow velocity), the density disturbances

resemble rope-like waves (see Fig. 2.14). These features are similar to the flat plate case treated in Ref. [21].

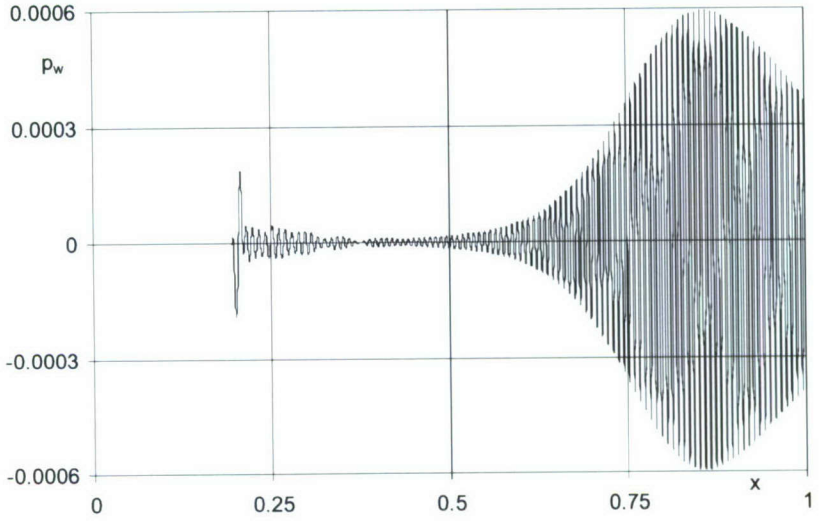

Fig. 2.12 The wall-pressure disturbances on a sharp cone.

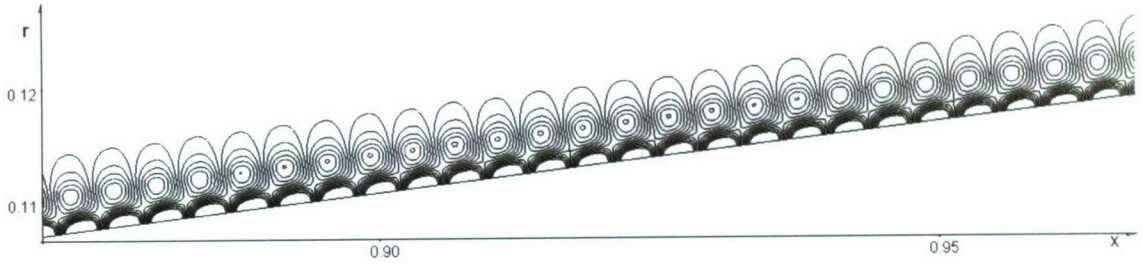

Fig. 2.13 Pressure disturbance field on a sharp cone, $0.87 \leq x \leq 0.9675$.

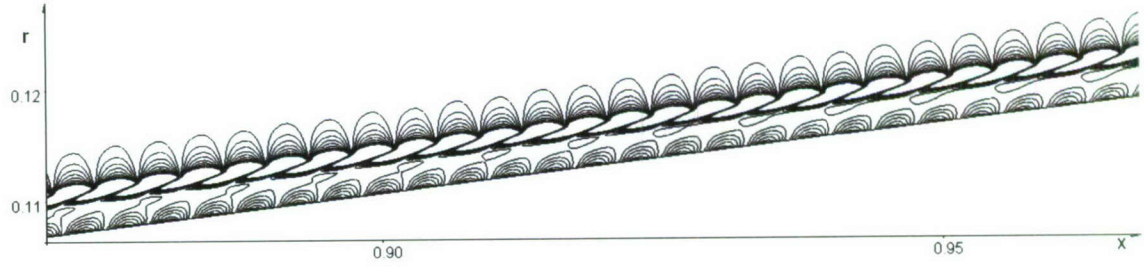

Fig. 2.14 Density disturbance field on a sharp cone, $0.87 \leq x \leq 0.9675$.

To evaluate the UAC effect on the disturbance field, the porous wall boundary condition (2.2) has been imposed in the region $x \geq 0.52$ (corresponding to $x \geq 182$ mm in the experiment

[12]). Calculations have been performed for the UAC parameters relevant to the experimental conditions: $r_0 = 7.14 \times 10^{-5}$, $h = 1.286 \times 10^{-3}$, $s = 4r_0$, $\phi = \pi r_0^2 / s^2 = \pi / 16$. Figure 2.15 shows that the pressure disturbance amplitude on the porous wall is essentially smaller than that on the solid wall (Fig. 2.12). The UAC weakly affects the second mode phase speed in accord with the flat-plate case treated in Section 2.2.1.

In order to compare the disturbance growth rates σ determined in the experiment [12] with those predicted by DNS, we calculate $\sigma(x)$ along the line of maximum mass-flow oscillations using the relation $\sigma = \dfrac{d}{dx}\left[\ln\left\langle \rho(x)\, u(x)\right\rangle\right]$. Figure 2.16 shows $\sigma(x)$ for the solid-wall case: curve 1 corresponds to DNS, curve 3 – LST, and curve 2 – experiments [12]. Similar comparison for the porous-wall case is presented in Fig. 2.17. The growth rates predicted by DNS are higher than those observed in experiment. This discrepancy is presumably due to nonlinear effects, because the amplitude of fundamental harmonic saturates under the experimental conditions. Similar trend was numerically observed in Ref. [21].

Fig. 2.15 Pressure disturbances on the cone surface with UAC.

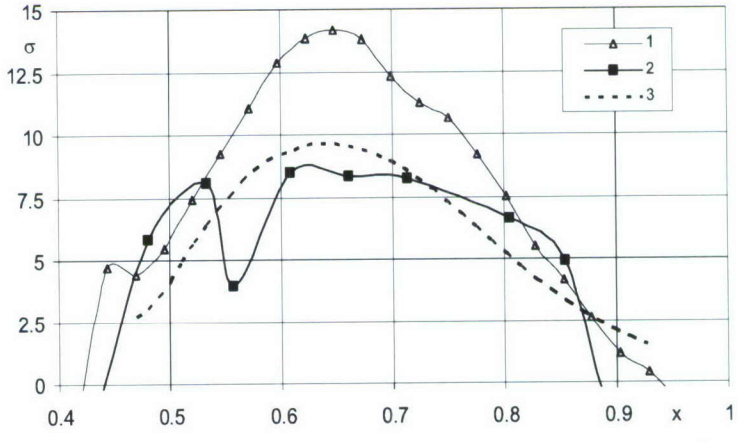

Fig. 2.16 Growth rates for the solid wall case: 1 – DNS, 2 – experiment, 3 – LST.

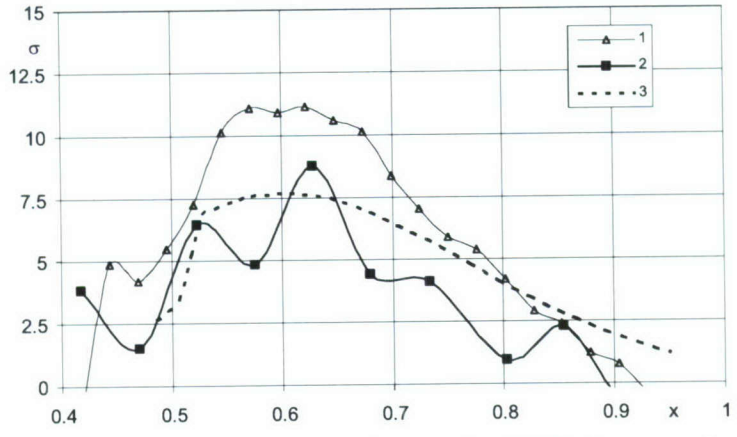

Fig. 2.17 Growth rates for the porous wall case: 1 – DNS, 2 – experiment, 3 – LST.

2.3. Reflection of acoustic disturbances from a porous coating of regular microstructure

Since the second mode represents trapped acoustic waves of ultrasonic frequency band, it is assumed that basic features of its interaction with a porous coating can be captured by considering reflection of ultrasonic disturbances from the UAC surface without external boundary-layer flow. This will help to examine end-effects associated with scattering of incoming acoustic disturbances by the pore openings, and evaluate robustness of our theoretical models describing propagation of acoustic disturbances within a porous layer.

In this connection we have analyzed reflection of ultrasonic waves from a plane surface covered by UAC of regular micro-structure (see Fig. 1.1). Theoretical predictions of the reflection coefficient are compared with the benchmark (no flow) measurements at various ambient pressures with special emphasis on low pressures relevant to high-altitude hypersonic flights. Details of this study will be presented in Ref. [28]

2.3.1. Theoretical model

Consider reflection of a plane monochromatic acoustic wave of an ultrasonic frequency band from a lane surface covered by UAC of regular microstructure (Fig. 3.1). It is assumed that the UAC frame is absolutely rigid and its temperature is uniform and constant.

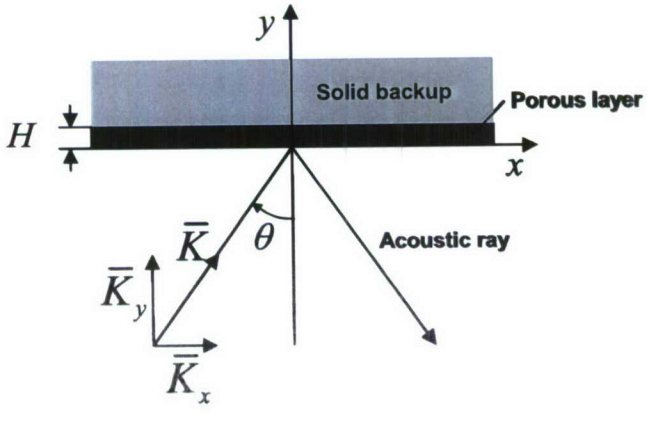

Fig. 3.1 Reflection of acoustic wave from a solid wall covered by a porous layer.

Small disturbances of density ρ', pressure p', temperature T' and velocity $\mathbf{v}$ are governed by the linearized Navier-Stokes equations

$$\frac{\partial \rho'}{\partial t} + \rho_0 (\nabla \cdot \mathbf{v}) = 0, \tag{3.1}$$

$$\rho_0 \frac{\partial \mathbf{v}}{\partial t} + \nabla p' = \mu \Delta \mathbf{v} + \left(\frac{1}{3}\mu + \zeta\right) \nabla (\nabla \cdot \mathbf{v}), \tag{3.2}$$

$$\rho_0 c_P \frac{\partial T'}{\partial t} = \frac{\partial p'}{\partial t} + \kappa \Delta T', \tag{3.3}$$

where Δ – Laplacian, μ – dymanic viscosity, ζ – bulk viscosity, the subscript "zero" denotes unperturbed quantities.

The interaction of acoustic wave with the solid wall leads to formation of the Stokes layer on the wall surface. Its thickness is estimated as $\delta_{visc} = \sqrt{2\mu / \rho_0 \omega}$, where ω is angular frequency. For disturbances of frequency $f = 200$ kHz relevant to the benchmark experiment, δ_{visc} varies from $4.9\,\mu$m at the normal atmospheric pressure to 69.6 μm at $p_0 = 5$ mbar. The acoustic wave has the wave length $\lambda \approx 1720$ μm at the room temperature $T_0 = 295$K. Since $\delta_{visc} \ll \lambda$, the Stokes layer and details of the UAC microstructure (holes of $100\,\mu$m diameter with spacing of $200\,\mu$m) can be ignored. Then the boundary condition on the UAC surface are formulated in the inviscid approximation

$$p'(x,0) = -Z_c \langle v(x,0) \rangle, \tag{3.4}$$

where $\langle\ \rangle$ – averaging over the UAC surface area. Furthermore, the gas motion can be treated as irrotational, $\mathrm{rot}\mathbf{v} = 0$. The system of equations (3.1)-(3.3) is implemented by the gas state equation in the form of Ref. [29]

$$\frac{p}{p_0} = \left(\frac{\rho}{\rho_0}\right)^{\gamma} \exp\left(\frac{S - S_0}{c_V}\right), \tag{3.5}$$

and the energy law

$$TdS = c_V dT + pd\left(\rho^{-1}\right), \tag{3.6}$$

where S is entropy. Using (3.5) we obtain

$$p' / \rho_0 c_0^2 \approx \rho' / \rho_0 + S' / c_P. \tag{3.7}$$

Equation (3.6) gives

$$T' \approx \left(\frac{\partial T}{\partial \rho}\right)_s \rho' + \left(\frac{\partial T}{\partial s}\right)_\rho S' = \frac{T_0}{c_V}\left(\frac{p_0}{\rho_0 T_0}\frac{\rho'}{\rho_0} + S'\right), \tag{3.8}$$

where $c_0 = \sqrt{\gamma p_0 / \rho_0}$ – speed of sound, γ – specific heat ratio. Using (3.8) we can express the linearized energy equation in the form (see, for example, Ref. [29])

$$\frac{\partial S'}{\partial t} = \frac{\kappa}{\rho_0 T_0}\Delta T' = \frac{\kappa}{\rho_0 c_V}\left\{\Delta S' + \frac{p_0}{\rho_0^2 T_0}\Delta\rho'\right\}. \tag{3.9}$$

Since $\mathrm{rot}\mathbf{v} = 0$, we introduce the velocity potential φ as $\mathbf{v} = \nabla\varphi$. Integrating the linearized momentum equation (3.2) once, we obtain

$$\rho_0\frac{\partial\varphi}{\partial t} + p' - \left(\frac{4}{3}\mu + \zeta\right)\Delta\varphi = 0. \tag{3.10}$$

Thus, the system of governing equations reads

$$\frac{\partial\rho'}{\partial t} + \rho_0\Delta\varphi = 0, \tag{3.11}$$

$$\frac{\partial\varphi}{\partial t} - \frac{1}{\rho_0}\left\{\left(\frac{4}{3}\mu + \zeta\right)\Delta\varphi - c_0^2\rho' - p_0\, S'/c_V\right\} = 0, \tag{3.12}$$

$$\frac{\partial S'}{\partial t} - \frac{\kappa}{\rho_0 c_V}\left\{\Delta S' + \frac{p_0}{\rho_0^2 T_0}\Delta\rho'\right\} = 0, \tag{3.13}$$

with the boundary condition (3.4) on the wall surface. Introduce the unknown quantities $F_1' = \rho'/\rho_0$, $F_2' = \omega\varphi/c_0^2$, $F_3' = S'/c_P$, and express them in the traveling wave form

$$F_j' = \delta_j \exp\{i\omega t - i(\mathbf{K}\cdot\mathbf{r})\},\ j = 1, 2, 3, \tag{3.14}$$

where $\mathbf{K}$ is complex wave vector, and δ_j are dimensionless complex amplitudes. Substitution of (3.14) into the system (3.11)-(3.13) leads to the homogeneous linear algebraic system

$$\begin{pmatrix} 1 & i\bar{\mathbf{K}}^2 & 0 \\ 1 & i + b_1\bar{\mathbf{K}}^2 & 1 \\ (\gamma-1)b_2\bar{\mathbf{K}}^2 & 0 & i + \gamma b_2\bar{\mathbf{K}}^2 \end{pmatrix}\begin{pmatrix}\delta_1\\ \delta_2\\ \delta_3\end{pmatrix} = 0, \tag{3.15}$$

where $\bar{\mathbf{K}}^2 = (\mathbf{K}\cdot\mathbf{K})/k_0^2 = \left(K_x^2 + K_y^2 + K_z^2\right)/k_0^2$, $k_0 = \omega/c_0$ is the wave-vector module in non-absorbing gas, $b_1 = (4\mu/3 + \zeta)\omega/\rho_0 c_0^2$, $b_2 = \kappa\omega/\rho_0 c_0^2 c_P = \mu\omega/\rho_0 c_0^2\,\mathrm{Pr}$. The solvability condition for the system (3.15) gives the dispersion relation

$$ib_2(1 + i\gamma b_1)\left(\bar{\mathbf{K}}^2\right)^2 - \left[1 + i(b_1 + \gamma b_2)\right]\bar{\mathbf{K}}^2 + 1 = 0, \tag{3.16}$$

with the roots

$$\left(\bar{\mathbf{K}}^2\right)_{1,2} = \frac{1 + i(b_1 + \gamma b_2) \mp \sqrt{\left[1 + i(b_1 + \gamma b_2)\right]^2 - 4ib_2(1 + i\gamma b_1)}}{2ib_2(1 + i\gamma b_1)}. \tag{3.17}$$

If the coefficients b_1 and b_2 are small ($b_1 \sim b_2 \ll 1$), then the roots (3.17) are approximated as

$$\left(\bar{\mathbf{K}}^2\right)_1 \approx 1 - i\left[b_1 + (\gamma - 1)b_2\right], \tag{3.18}$$

$$\left(\bar{\mathbf{K}}^2\right)_2 \approx -i/b_2. \tag{3.19}$$

The root $\left(\bar{\mathbf{K}}^2\right)_2$ is relevant to the thin Stokes layer that is ignored in the approximation considered herein. Then the pressure disturbance near the wall surface is expressed as a sum of incident and reflected waves

$$p' = \rho_0 c_0^2 A \exp\left[i\omega t - ik_0 \bar{K} x \sin\theta\right]\left[\exp\left(ik_0 \bar{K} y \cos\theta\right) + R\exp\left(-ik_0 \bar{K} y \cos\theta\right)\right], \tag{3.20}$$

where R – complex reflection coefficient, $A = \text{const}$, $\bar{K} \approx 1 - 0.5i\left[b_1 + (\gamma - 1)b_2\right]$, θ – the angle of incidence (Fig. 3.1). The velocity potential φ is expressed in terms of the density pulsations using the linearized continuity equation (3.11)

$$\varphi = \frac{ic_0^2}{\omega \bar{\mathbf{K}}^2}\frac{\rho'}{\rho_0}. \tag{3.21}$$

In accord with (3.7), density pulsations are coupled with pressure and entropy pulsations as

$$\frac{\rho'}{\rho_0} = \frac{p'}{\rho_0 c_0^2} - \frac{S'}{c_P}. \tag{3.22}$$

The linearized energy equation (3.13) gives

$$\frac{S'}{c_P} = i\frac{(\gamma - 1)b_2 \bar{\mathbf{K}}^2}{1 - i\gamma b_2 \bar{\mathbf{K}}^2}\frac{\rho'}{\rho_0}. \tag{3.23}$$

Substituting (3.23) into (3.22) we obtain

$$\frac{\rho'}{\rho_0} = \frac{1 - i\gamma b_2 \bar{\mathbf{K}}^2}{1 - ib_2 \bar{\mathbf{K}}^2} \cdot \frac{p'}{\rho_0 c_0^2}, \tag{3.24}$$

and substituting (3.24) into (3.21) we express the velocity potential as

$$\varphi = \frac{ic_0^2}{\omega \bar{\mathbf{K}}^2}\frac{1 - i\gamma b_2 \bar{\mathbf{K}}^2}{1 - ib_2 \bar{\mathbf{K}}^2}\left(\frac{p'}{\rho_0 c_0^2}\right). \tag{3.25}$$

Using these relations we satisfy the boundary condition (3.4) and obtain the reflection coefficient

$$R = \frac{\beta \bar{Z}_c \cos\theta - 1}{\beta \bar{Z}_c \cos\theta + 1}, \tag{3.26}$$

$$\beta = \frac{1}{\bar{K}}\frac{1 - i\gamma b_2 \bar{\mathbf{K}}^2}{1 - ib_2 \bar{\mathbf{K}}^2} \approx 1 + 0.5i\left[b_1 - (\gamma - 1)b_2\right], \tag{3.27}$$

$$\bar{Z}_c = \frac{Z_c}{\rho_0 c_0} = \frac{1}{\phi}\sqrt{\frac{\tilde{\rho}}{\tilde{C}}}\coth(mh). \tag{3.28}$$

Here $\bar{Z}_c$ is normalized characteristic impedance and m is propagation constant, h – porous layer thickness, ϕ – porosity. The dynamic density $\tilde{\rho}$, dynamic compressibility $\tilde{C}$ and propagation constant m of an isolated cylindrical long pore are calculated using the analytical

solutions of Ref. [19]. Note that the foregoing solution gives well known formula for the absorption coefficient α_P of viscous heat-conducting gas

$$\alpha_P \approx 0.5[b_1 + (\gamma - 1)b_2]\omega/c_0 = 0.5\left[4/3 + \zeta/\mu + (\gamma - 1)/\mathrm{Pr}\right]\left(\mu\omega^2/\rho_0 c_0^3\right). \quad (3.29)$$

The coefficient α_P is relatively large at low ambient pressures and high frequencies considered hereafter. However, as will be shown below, this absorption weakly affects the reflection process; i.e., in many practical cases we can use the approximation $\beta \approx 1$ and calculate the reflection coefficient using the formula

$$R = \frac{\overline{Z}_c \cos\theta - 1}{\overline{Z}_c \cos\theta + 1}. \quad (3.30)$$

2.3.2. Benchmark setup and UAC sample

Reflection of an ultrasonic beam from a solid plate and from a plate covered by UAC of regular microstructure have been measured by Robert Addison (Teledyne) at various ambient pressures. The experimental setup is shown in Fig. 3.2, and its scheme is presented in Fig. 3.3. An ultran transducer generates acoustic beam of frequency $f = 200$ kHz, diameter ≈ 50 mm and the angle of incidence $\theta = 32.4^\circ$. Another transducer measures the reflected beam. The apparatus and test plate are covered by a bell jar of $10''$ diameter. A vacuum pump allows for changing of the ambient pressure from approximately 1000 mbar down to 5 mbar. Test articles are metallic plates with the solid surface and with the surface covered by UAC. The porous coating is a perforated stainless steel sheet of thickness $H = 560\,\mu$m with equally spaced cylindrical holes of diameter $d \approx 100\,\mu$m. The hole spacing is $s \approx 200\,\mu$m that gives porosity $\phi = \pi(d/2s)^2 \approx 20\%$. Preliminary theoretical estimates show the foregoing signal frequency and UAC parameters correspond to the conditions typical for hypersonic laminar flow control applications.

Fig. 3.2 Experimental setup for measurements of ultrasonic beam reflection.

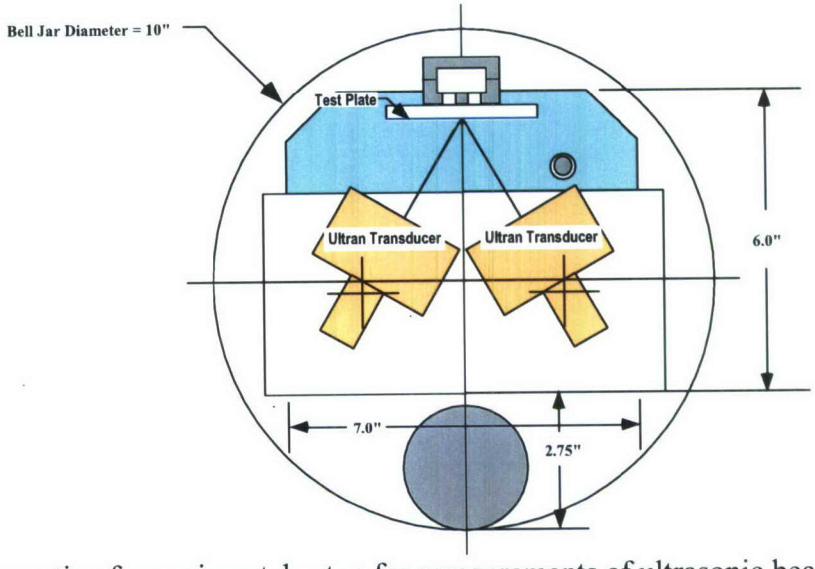

Fig. 3.3 Schematic of experimental setup for measurements of ultrasonic beam reflection.

Imaging and measurements of the UAC microstructure have been performed by Sergio Lucato and Michael Calabrese (Teledyne). Electronic images of the face (a) and back (b) UAC surfaces are shown in Fig. 3.4. Their analysis gives the average parameters: hole diameter $d = 100.5$ μm, hole depth $h = 560$ μm, porosity $\phi = 20.56\,\%$.

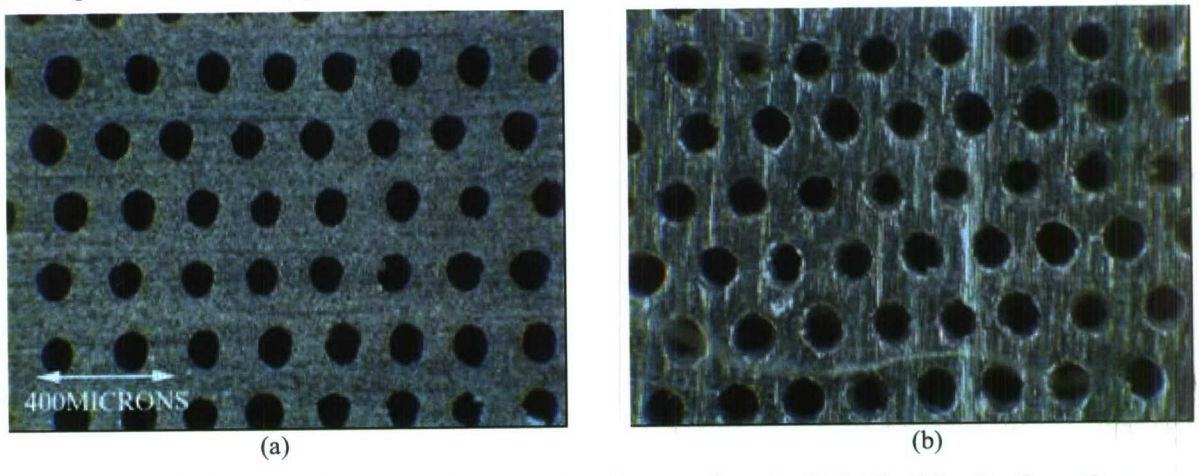

(a) (b)

Fig. 3.4 E-images of perforated plate, (a) – face surface (polished), (b) – back surface.

Measurements of the peak-to-peak pressure amplitude of the reflected beam were performed for the solid plate ($A_{p,solid}$) and for the plate covered by UAC ($A_{p,porous}$). With the assumption that the reflection from the solid plate is perfect ($R_{solid} = 1$), the reflection coefficient for the porous wall is $R_{porous} = A_{p,porous} / A_{p,solid}$. In dB units, this relation is written as $20 \log_{10} R_{porous} = E$, where $E = 20 \log_{10}(A_{p,porous} / A_{p,solid})$ is the attenuation excess. The ratio of $R_{porous}(p)$ at a certain ambient pressure p to its value $R_{porous}(p_0)$ at the reference ambient pressure p_0 is

$$R_{porous}(p) / R_{porous}(p_0) = 10^{-[E(p) - E(p_0)]/20}. \tag{3.31}$$

The value $\Delta E = E(p_0) - E(p)$ (with $p_0 = 800$ mbar) has been tabulated in the range of p from 5 mbar to 800 mbar.

2.3.3. Experimental results and comparison with theory

Comparison of four data sets (symbols) with the theoretical solutions (3.26) (thin red line) and (3.30) (thick black line) is shown in Fig. 3.5. Calculations of the ratio $R_{porous}(p)/R_{porous}(p_0)$ were performed for air ($\mathrm{Pr} = 0.72$ and $\gamma = 1.4$) at the room temperature $T = 295\,\mathrm{K}$. The viscosity coefficient is approximated by the Sutherland law

$$\mu = 1.458 \times 10^{-6} \frac{T^{3/2}}{T + 110.4} \ [\mathrm{kg/(m{\times}s)}]. \tag{3.32}$$

Calculations of the propagation constant m and impedance $\overline{Z}_c$ in (3.28) have been conducted with accounting for the Knudsen effect as reported in Ref. [19]. The pore wall accommodation coefficients were specified as $\alpha_u = \alpha_E = 0.85$. In the ambient pressure range from 20 mbar to 1000 mbar, the theoretical solutions agree well with the experimental data. The acoustic absorption in air produces negligible effect on the reflection coefficient at the ambient pressure larger than 4 mbar (compare black and red lines). For $p < 20$ mbar, experimental data have large scatter. In this low-pressure range, measured acoustic signals have very small amplitude due to strong attenuation of the reflected signal in air and due to significant mismatch between the acoustic resistances of the ultran transducer and ambient gas medium. Additional measures should be taken to increase accuracy in this low-pressure range.

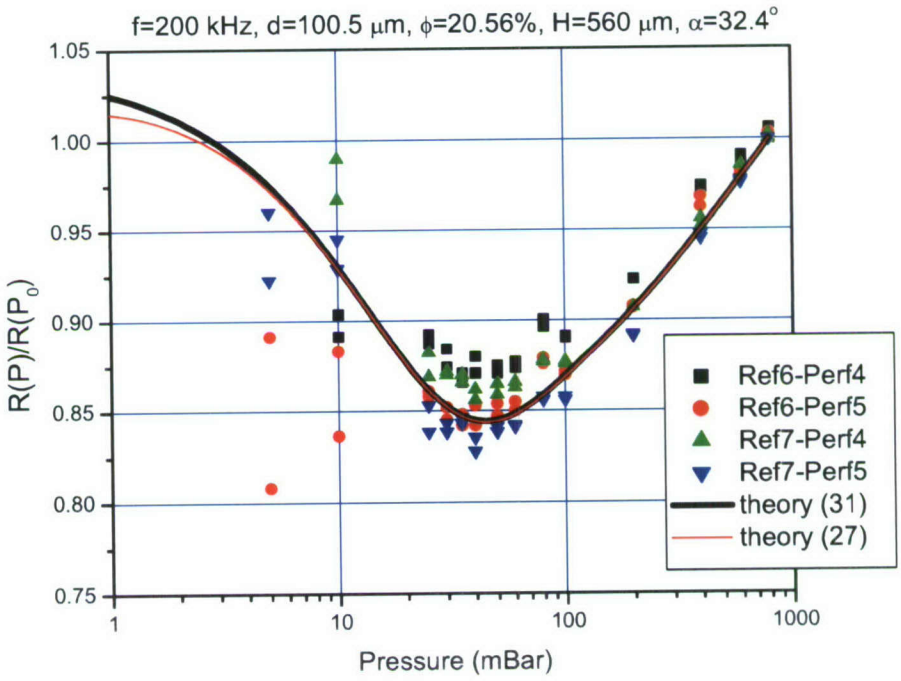

Fig. 3.5 The reflection coefficient ratio as a function of ambient pressure, black solid line – solution (3.30), red thin line – solution (3.26), symbols – experiment.

2.4. Interaction of acoustic disturbances with UAC micro-cavities

Design and robust implementation of UAC on hypersonic vehicles hinge on the development of accurate and efficient low-order models providing boundary conditions on the UAC surface to be used by traditional computational fluid dynamic (CFD) and instability codes. The research thus seeks to validate and improve existing porous-wall boundary-condition models. This motivates us to conduct direct numerical simulations for the boundary layer disturbances including unsteady processes within the micro cavities that constitute the UAC. DNS helps to examine end-effects at the mouths and bottoms of cavities, clarify dependencies of the UAC performance on the cavity spacing and depth, propose improvements of existing models to extend their range of validity, and generalize their use as a tool for design and implementation of UAC in applications.

Herein we use DNS to investigate in detail the interaction of incident acoustic waves with groups of equally-spaced micro-cavities on the at plate surface without flow. Although the external boundary-layer flow is an important component of the UAC modeling, this unit problem is of particular interest, since mechanisms of reflection and absorption of incoming boundary-layer disturbances occur near the cavity edges and inside cavities where the external flow is relatively slow and seems to play a minor role. Furthermore, the acoustic properties of UAC samples should be estimated in economical way before their testing in hypersonic wind tunnels. This can be done using benchmark (no-flow) measurements discussed in Section 2.3.

Consider the reflection of plane monochromatic acoustic waves of an ultrasonic frequency band from a plane surface covered by a porous coating (Fig. 4.1). The coating has a regular structure comprising equally-spaced slots (2-D cavities). It is assumed that the UAC frame is absolutely rigid and its temperature is uniform and constant.

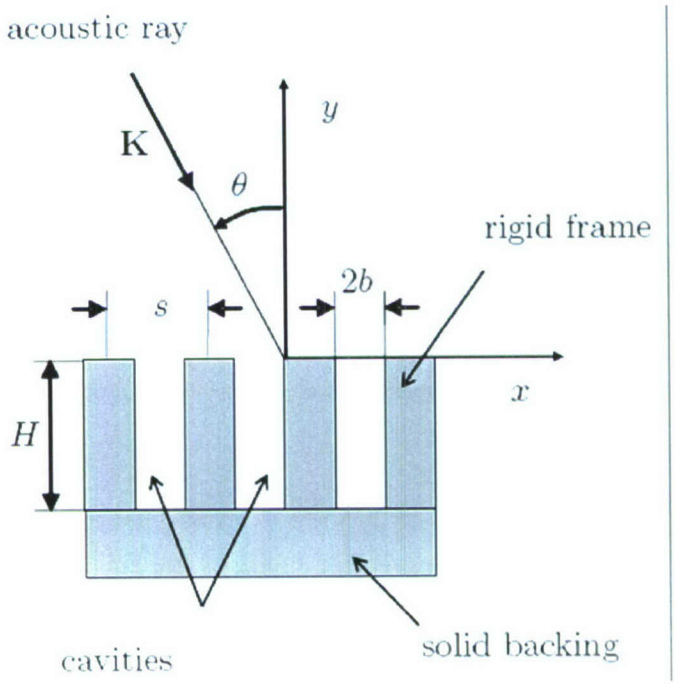

Fig. 4.1 Schematic of the reflection of acoustic wave from equally spaced 2-D cavities.

2.4.1. Numerical method

Colonius and Brès [30-32] developed a DNS code to solve the full compressible Navier-Stokes (NS) equations and study the flow over three-dimensional open cavities. The equations are solved directly, meaning that no turbulence model is used and all the scales of the flow are resolved. The code was modified to model the flow in individual and groups of equally-spaced micro-holes (i.e., cavities) in a rigid surface under a transitional boundary layer. We assume shock-free flow and use high-order accurate compact finite difference schemes for streamwise and normal directions, and Fourier-spectral differentiation for homogeneous directions (when present). The usual compressible formulation is used to nondimensionalize the NS equations, where the superscript d refers to the dimensional quantity, and the subscript 0 denotes the ambient undisturbed property:

$$\rho = \rho^d / \rho_0,\ p = p^d / (\rho_0 c_0^2),\ T = T^d c_p / c_0^2,\ u_i = u_i^d / c_0,\ x_i = x_i^d / H,\ t = t^d c_0 / H. \qquad (4.1)$$

The fluid is a perfect gas with specific heat at constant pressure c_p, Pr = 0.72 and $\gamma = 1.4$. The temperature at the walls is assumed uniform and constant ($T = T_0$). The code can handle any type of block geometry (including the porous surface configuration shown in Fig. 4.1) and is fully parallelized using Message-Passing Interface (MPI).

The current study focuses on the acoustic scattering by groups of equally-spaced 2-D micro-cavities without external flow. An incoming planar acoustic pulse of gaussian shape at angle of incidence θ is initialized in the computational domain. The pressure fields created by this acoustic pulse and its reflection on a solid wall (without cavities) and on a porous wall (with cavities) are computed, and can be decomposed as:

$$p_{solid}(x,y,t) = p_{inc}(x,y,t) + p_{ref,solid}(x,y,t),\ \ p_{porous}(x,y,t) = p_{inc}(x,y,t) + p_{ref,porous}(x,y,t). \qquad (4.2)$$

Assuming that the interaction is linear, and there is no overlapping of the incident and reflected waves, we can identify the reflected signals at any fixed point (x_0, y_0), and expand the signals $p_{ref,solid}(t)$ and $p_{ref,porous}(t)$ into Fourier integrals

$$p_{ref,solid}(t) = \frac{1}{\sqrt{2\pi}} \int_{-\infty}^{+\infty} \hat{p}_{ref,solid}(\omega) e^{-i\omega t} d\omega,\ p_{ref,porous}(t) = \frac{1}{\sqrt{2\pi}} \int_{-\infty}^{+\infty} \hat{p}_{ref,porous}(\omega) e^{-i\omega t} d\omega. \qquad (4.4)$$

Since the reflection from a solid wall has a reflection coefficient $R = 1$, we can calculate the complex reflection coefficient for the porous wall as

$$R_{DNS}(\omega) = \hat{p}_{ref,porous}(\omega) / \hat{p}_{ref,solid}(\omega), \qquad (4.5)$$

and compare it to the theoretical value $R(\omega)$ given by (3.30).

2.4.2. Parametric study

The first configuration considered corresponds to 2-D micro-cavities of constant length to depth ratio $2b / H = 0.12$, and an acoustic pulse at normal incidence

$$p_{pulse}(x,y) = p_i \exp[-(y - y_c)^2 / \sigma^2]. \qquad (4.6)$$

The reflected signal is measured at $(x_0, y_0) = (0,2)$ above the surface, for different Reynolds numbers: $\mathrm{Re} = \rho_0 c_0 b / \mu_0 =$ 1000, 100, and 10. For validation purposes, different measurement locations, computational grid spacings and widths σ of the incoming acoustic pulse were considered, and lead to identical results for the reflection coefficient, up to dimensionless frequency $f = f^d H / c_0 \approx 2$. For typical UAC parameters (e.g., $H \approx 500$ μm in Ref. [10]), this range of frequencies correspond to the ultrasonic frequency band, and is sufficient to capture the frequency of the most amplified second-mode instability waves observed in experiments [12] and predicted in theory [9, 18].

Figure 4.2(a) shows the time-history of the reflected signal p_{ref} normalized by the initial pulse amplitude p_{inc} for a flat plate and a porous surface of porosity $\phi = 0.48$, at different Reynolds numbers. A sequence of compression and expansion waves from the solid surface, and the bottom of the cavity can be identified. The corresponding reflection coefficient is shown in Fig. 4.2(b). At higher Reynolds numbers (Re = 1000 and 100), reflections from the bottom of the cavities lead to destructive/constructive reinforcement at some specific frequencies. In contrast, there is no additional reflection for Re = 10 because of the increase in viscous dissipation inside the cavities and the reflection coefficient decreases with increasing frequency.

To investigate the influence of porosity, additional simulations are performed for $\phi = 0.2$ and $\phi = 0.8$, keeping the same cavity aspect ratio. The pressure time-history and reflection coefficient for Re = 100 are shown in Figs. 4.3(a) and (b), respectively. As expected, the amplitude of the reflection from the bottom of the cavity (i.e., the second peak in Fig. 4.3(a)) increases with porosity. Overall, the reflection coefficient increase as porosity decrease, which is consistent with the limit value $|R| = 1$ for $\phi = 0$.

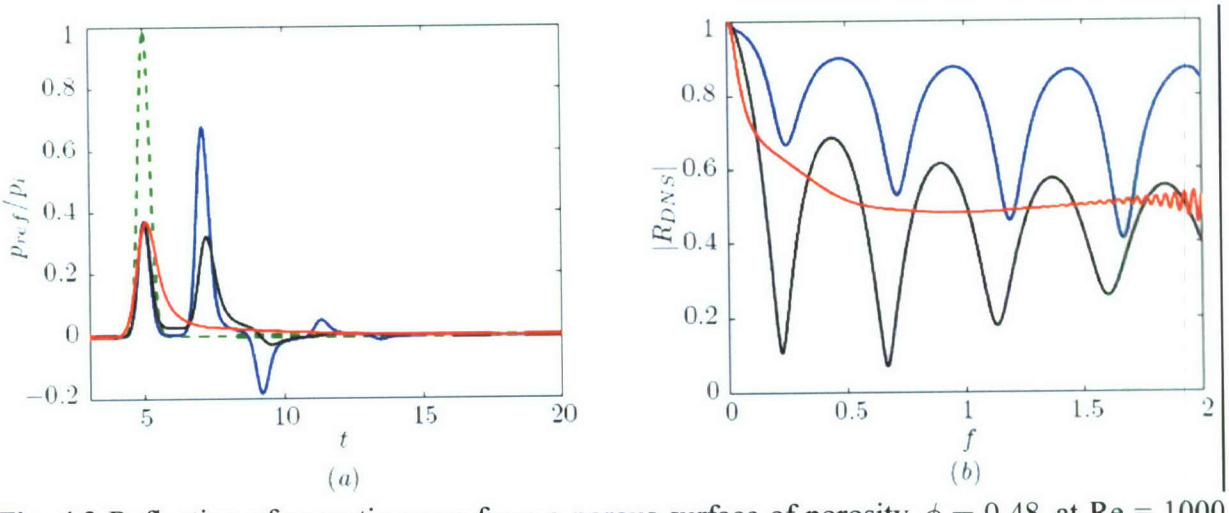

Fig. 4.2 Reflection of acoustic wave from a porous surface of porosity $\phi = 0.48$ at Re = 1000 (blue line), Re = 100 (black line), and Re = 10 (red line). (a) – pressure time-history; (b) – reflection coefficient amplitude. For comparison, the reflected signal from a flat plate at Re = 1000 is also presented (dashed green line).

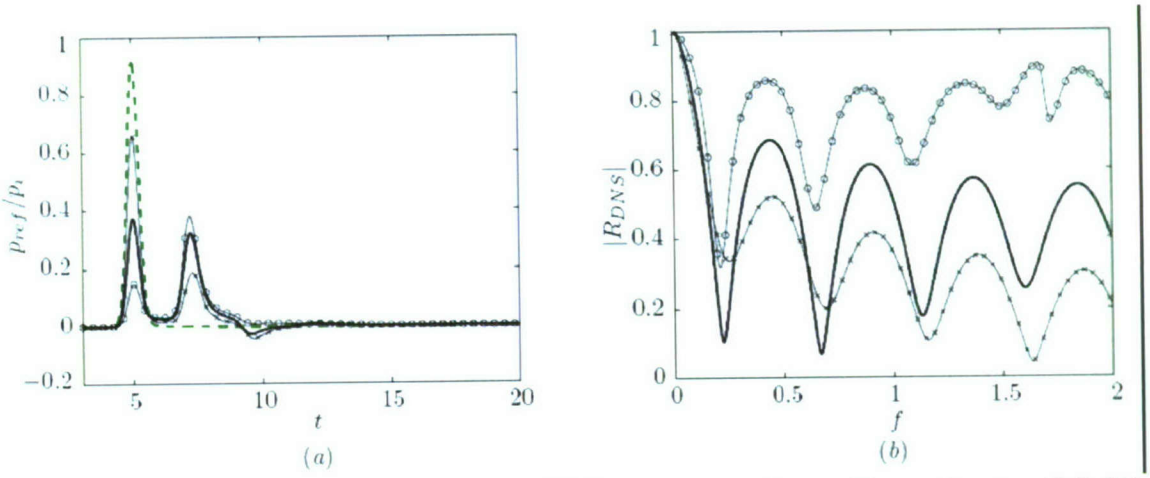

Fig. 4.3 Reflection of acoustic wave at Re = 100 for porous surfaces of porosity $\phi = 0.2$ (black line with circles), $\phi = 0.48$ (black line), and $\phi = 0.8$ (black line with crosses). (a) – pressure time-history; (b) – reflection coefficient amplitude. For comparison, the reflected signal from a at plate is also presented (dashed green line).

2.4.3. Comparison of DNS with theory

The comparisons between the reflection coefficients obtained from DNS and from theory (Eq. (3.30) of Section 2.3.1), for porosity $\phi = 0.8$, $\phi = 0.48$, and $\phi = 0.2$, are presented in Figs. 4.4 (a), (b), and (c), respectively. Overall, there is very good agreement between the DNS results and the theoretical predictions. Discrepancy increases with frequency because the theory assumes that the acoustic wavelength λ is much larger than the cavity half-width b. For instance, for frequency $f = 2$, the ratio of these quantities is only $b/\lambda = 0.12$. Similarly, the assumption that the cavity spacing s is of the order of the cavity half-width b leads to additional discrepancies at low porosity (i.e., $b/s = 0.125$ for $\phi = 0.2$). In these cases, the presence of the Stockes layer, which is not accounted for in the theoretical model, may affect the reflection coefficient. However, coatings of small porosity are of less interest for laminar-flow-control applications.

Details on parametric study of the geometrical factors (cavity aspect ratio, porosity) and flow conditions effects (Re, angle of incidence) will be presented in Ref. [33].

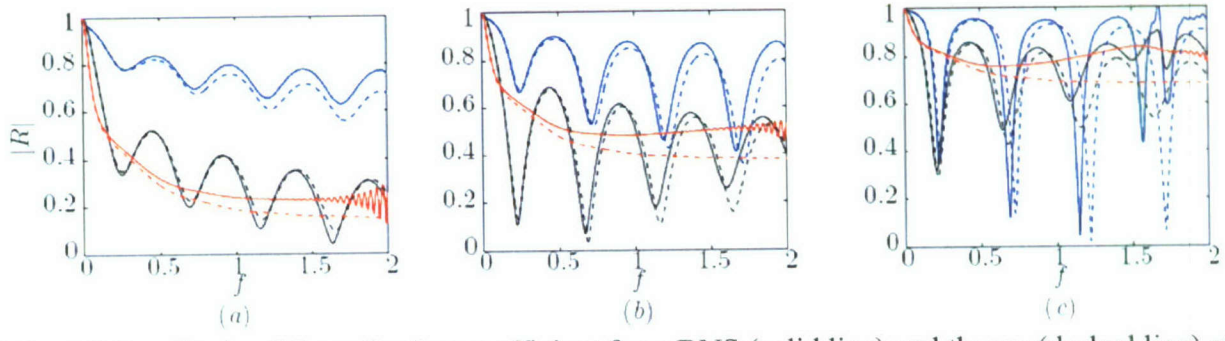

Fig. 4.4 Amplitude of the reflection coefficient from DNS (solid line) and theory (dashed line) at Reynolds number Re = 1000 (blue), Re = 100 (black), and Re = 10 (red). (a) – porosity $\phi = 0.8$, (b) – $\phi = 0.48$, (c) – $\phi = 0.2$.

2.5. Transition measurements on blunted cone with the felt-metal coating

UAC of random porosity could be more symbiotic with thermal protection systems (TPS) of actual hypersonic vehicles since the majority of TPS materials have random microstructures. In this connection, stability [11] and transition [14] measurements were performed on a sharp cone with a felt-metal coating in hypersonic wind tunnels of ITAM (Novosibirsk). Experiments [14] in the ITAM AT-303 high-enthalpy wind tunnel at Mach=12, showed that the felt-metal coating significantly (up to 100% of the model length) delayed transition. The major objective of present experiments is to conduct similar transition measurements at $M_\infty \approx 8.8$ and investigate the nose bluntness effect on the UAC-LFC performance.

2.5.1 Model and experimental setup

The cone model, which was tested in the ITAM AT-303 tunnel at free-stream Mach=12 [14] (Fig. 5.1), has been modified to study the UAC effect on transition at different radii of blunted nose. The original model is a 7° half-angle sharp cone. Its longitudinal half surface is solid, and the other half surface is covered by a porous coating. The total model length is of 1039 mm. The porous coating starts from the station $X = 70$ mm, where X is measured from the sharp nosetip along the cone axis. The felt-metal coating is composed of stainless steel fibers of 30 μm diameter. The fibers were hard sintered on a solid stainless steel sheet of 0.245 mm thickness. Then, they were rolled to the porosity $\phi = 0.75$. The porous layer has the thickness 0.75 mm so that the total thickness of the felt metal sheet is 1±0.1. The magnified image of the UAC surface is shown in Fig. 5.2. To treat bluntness effects, the exchangeable noses with spherical bluntness of radii $R = 0$, 1, 2, 4, 8 mm have been fabricated (Fig. 5.3). Hereafter these noses are denoted as R0, R1, R2, R4, R8, respectively.

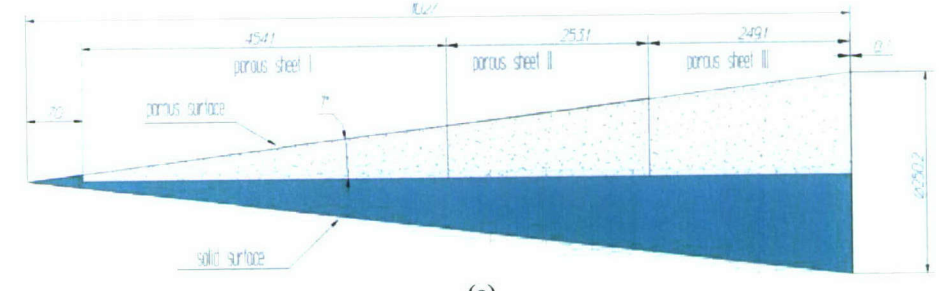

(a)

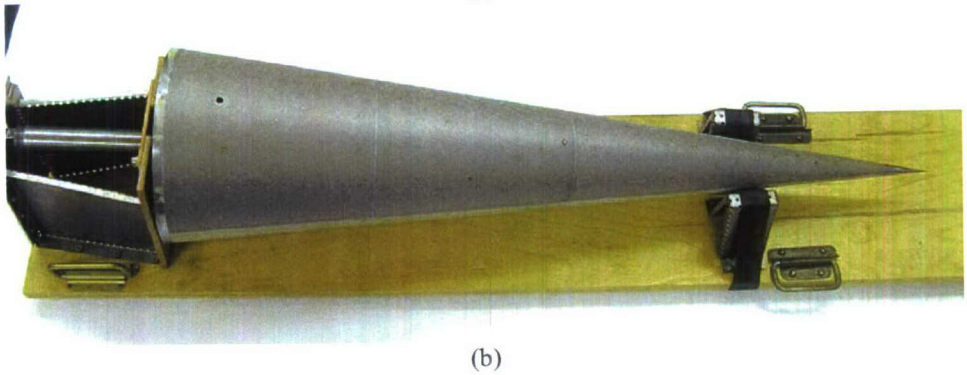

(b)

Fig. 5.1 Schematic view (a) and photo (b) of a sharp cone model with felt-metal coating tested at the free-stream Mach=12 [14].

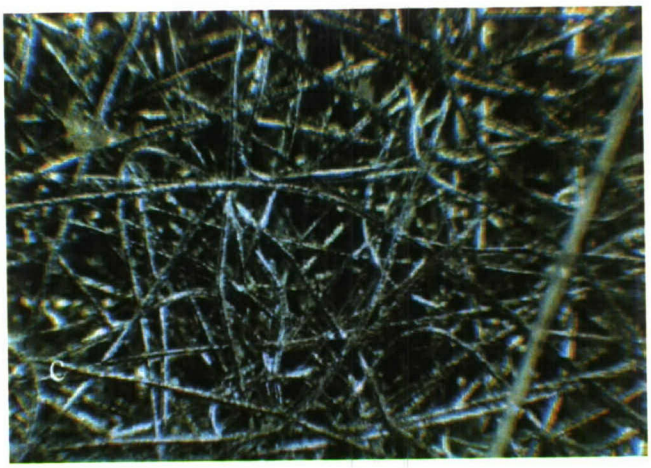

Fig. 5.2 Magnified image of the felt-metal coating.

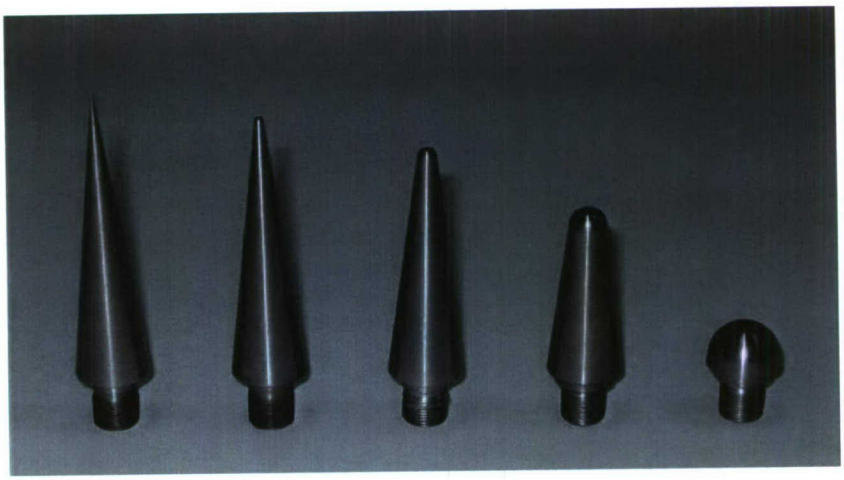

Fig. 5.3 Exchangeable noses with spherical bluntness of radii $R = 0$, 1, 2, 4, and 8 mm.

Transition measurements have been conducted in the ITAM AT-303 high-enthalpy wind tunnel (Fig. 5.4). Basic parameters of this facility are given in Table 1. Experiments are carried out at the free-stream Mach number $M_\infty = 8.8$. Typical Mach number profiles at the nozzle exit are shown in Fig. 5.5. Flow parameters for all runs are specified in Table 2.

Table 1. Basic parameters of wind tunnel AT – 303

Nozzle diameter D, mm	300	600
Settling chamber volume, dm^3	6.4	
Stagnation pressure P_0, bar	3000	
Stagnation temperature T_0, K	2500	
Mach number M	8 – 13	14 – 20
Reynolds number Re_D	$6 \cdot 10^7 - 1.5 \cdot 10^7$	$2 \cdot 10^7 - 2.5 \cdot 10^6$
Run duration t, s	0.04 – 0.2	
Test gases	air, nitrogen, CO_2, etc.	

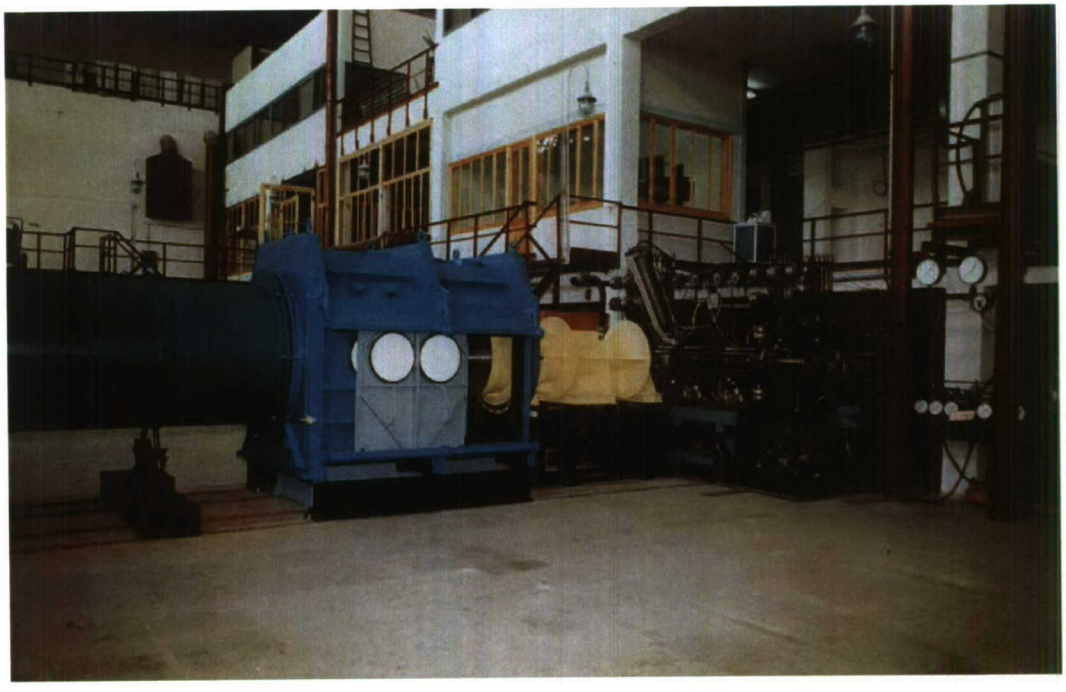

Fig. 5.4 General view of the AT-303 tunnel.

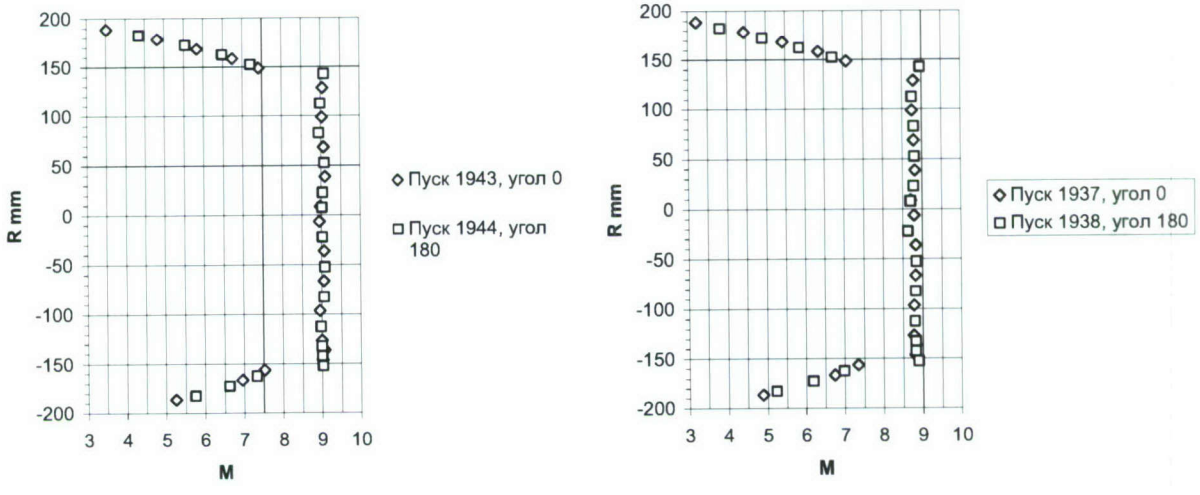

$Re_{1\infty}$=4.3 10^6 m^{-1} $Re_{1\infty}$=13.9 10^6 m^{-1}

Fig. 5.5 Mach number profiles at the nozzle exit.

The model is installed so that its axis coincides with the nozzle axis. However, the model position is inspected using sizing tools only; i.e., small deviations of the angle of attack from zero are possible. To estimate this effect every run is repeated twice (with nominally identical flow parameters) at two orientations of the porous surface (up and down). For this purpose the model is turned around its axis to an angle $\theta = 180°$: $\theta = 0°$ corresponds to the UAC surface oriented up, and $\theta = 180°$ – oriented down. Positions of porous surface are indicated in Table 2.

Table 2. Parameters of runs

Run	Nose	θ,°	P_0, bar	T_0, K	M_∞	$Re_{1\infty}\cdot 10^6$, m^{-1}
1	R0	0	73.7	-	-	-
2	R0	0	72.6	1314.	8.795	4.11
3	R0	180	73.5	1313.	8.796	4.17
4	R1	180	74.2	1323.	8.796	4.15
5	R1	0	72.2	1318.	8.794	4.07
6	R2	0	74.8	1319.	8.797	4.22
7	R2	180	75.4	1319.	8.798	4.24
8	R4	180	76.0	1326.	8.798	4.24
9	R4	0	76.3	1321.	8.798	4.28
10	R4	0	76.3	1317.	8.799	4.30
11	R8	0	73.8	1316.	8.796	4.17
12	R8	180	73.5	1314.	8.796	4.16
13	R8	180	39.6	1081.	-	-
14	R8	180	119.9	1495.	8.818	5.25
15	R8	0	117.6	1491.	8.817	5.17
16	R4	0	118.4	1492.	8.817	5.20
17	R4	180	118.4	1489.	8.818	5.22
18	R2	180	118.3	1487.	8.818	5.23
19	R2	0	117.1	1483.	8.817	5.19
20	R1	0	121.6	1493.	8.82	5.34
21	R1	180	116.7	1489.	8.816	5.14
22	R0	180	116.7	1485.	8.817	5.18
23	R0	0	117.0	1485.	8.817	5.18
24	R0	180	88.1	1572.	8.781	3.46
25	R0	180	81.5	1539.	8.778	3.31
26	R4	180	89.3	1575.	8.782	3.50
27	R4	0	88.8	1579.	8.782	3.47
28	R0	0	88.5	1574.	8.782	3.47
29	R1	0	87.9	1573.	8.781	3.45
30	R1	0	88.2	1575.	8.781	3.46
31	R2	0	87.6	1575.	8.781	3.43
32	R8	0	88.3	1572.	8.782	3.47
33	R8	180	90.0	1576.	8.783	3.52
34	R2	180	88.9	1571.	8.782	3.50
35	R1	180	89.2	1574.	8.782	3.50

Time-histories of stagnation pressure, stagnation temperature and free-stream unit Reynolds number for nine runs are shown in Figs. 5.6 and 5.7. It is seen that during each run there is a time window of about 30-55 ms with almost constant flow parameters. Heat flux measurements have been conducted in this time interval. Examples of the calorimeter-sensor signal on solid and porous surface are shown in Fig. 5.8 for Run 3. Vertical lines indicate the time window for acquisition of the heat flux data.

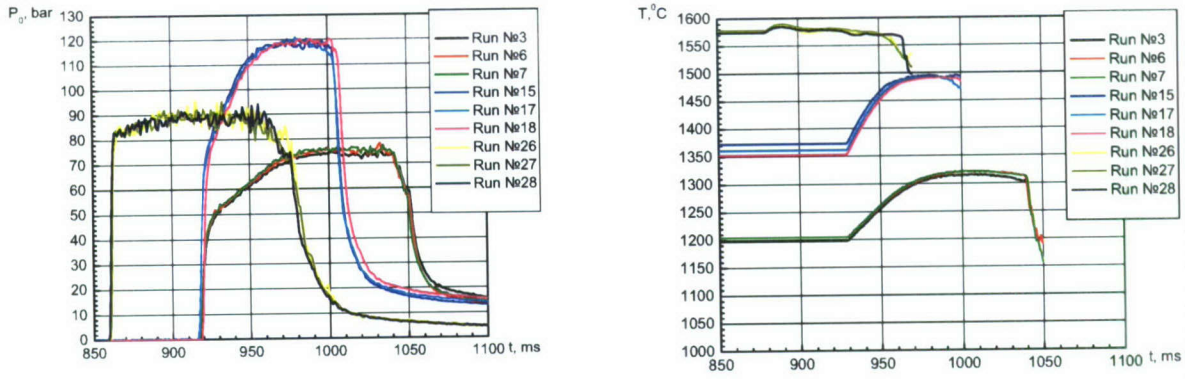

Fig. 5.6 Time-histories of stagnation pressure (left) and stagnation temperature (right) for nine runs.

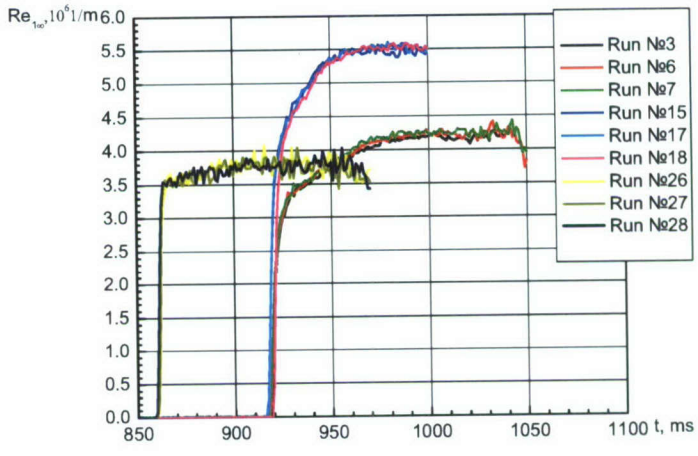

Fig. 5.7 Time-histories of unit Reynolds number for nine runs.

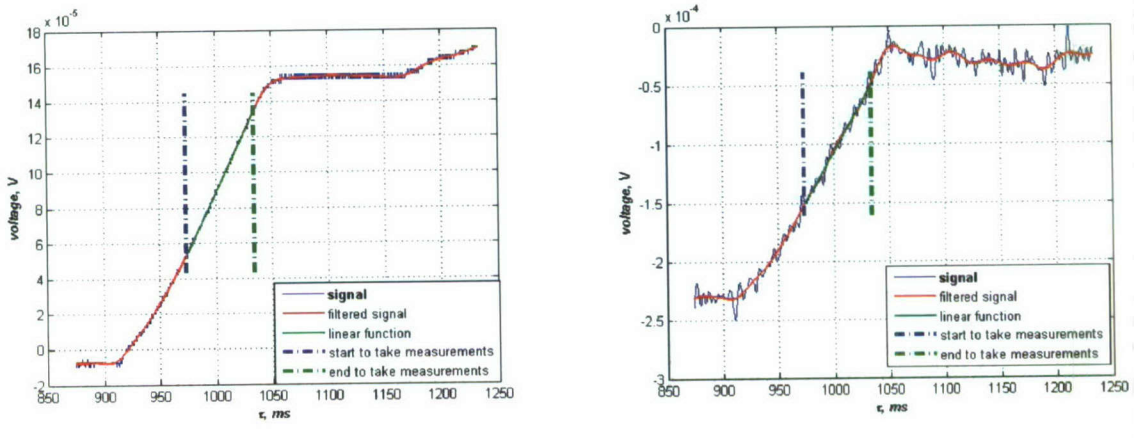

Fig. 5.8 Signal of Sensor 1 on porous (left) and solid (right) surface for Run 3.

2.5.2 Transition measurements

Transition loci are determined from distributions of heat flux, which are measured using 55 calorimeter sensors. The sensors are located on both solid and porous surfaces. The data acquisition system consists of 55 independent ADC converters with pre-amplifiers and filters. Data are acquired with the sampling rate of 5 kHz and processed as follows:

- Signal is smoothed using standard MATLAB 6.5 filter functions (ellip and filtfilt)
- The signal part corresponding to the data acquisition time window is extracted from the total signal
- Data are approximated by linear function using the least-squares method and a slope of this function is determined
- Heat flux is calculated as a product of the slope and the calibration sensitivity coefficient

The heat-flux distributions on solid and porous surfaces for noses R0, R1, R2, R4, and R8 are shown in Fig. 5.9. For transitional flow, the heat flux is decreased with X in the laminar flow region, rapidly grows during transition, and decreases again in the turbulent flow region. In the considered unit Reynolds number range, transition is not observed for large nose radii: R4 and R8 for porous surface, and R8 for solid surface.

There is good agreement between the heat flux distributions mastered at different orientations of the porous surface; i.e., the angle of attack is close to zero, and the free stream is sufficiently uniform. This allows us to calculate the transition loci by averaging the transition points for each pare of runs with $\theta = 0^\circ$ and $\theta = 180^\circ$. The transition onset point is determined as a point of minimum heat flux, and the transition end point – as a point of maximum heat flux. To identify these points the heat-flux distributions are filtered as shown in Fig. 5.10.

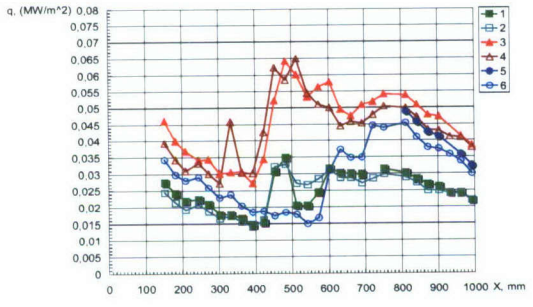

Nose R0, porous

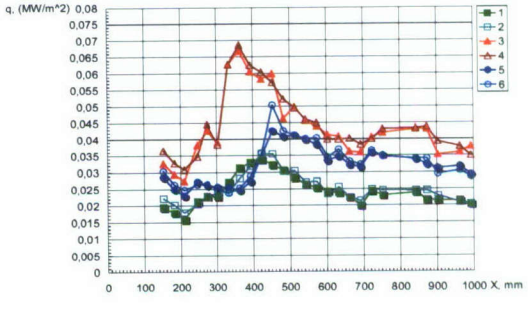

Nose R0, solid

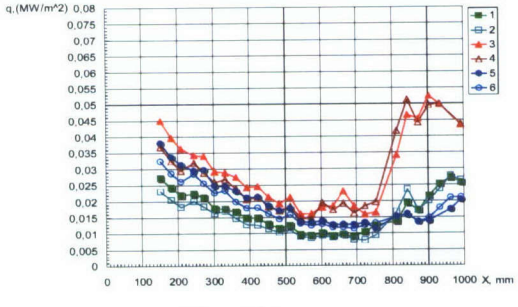

Nose R2, porous

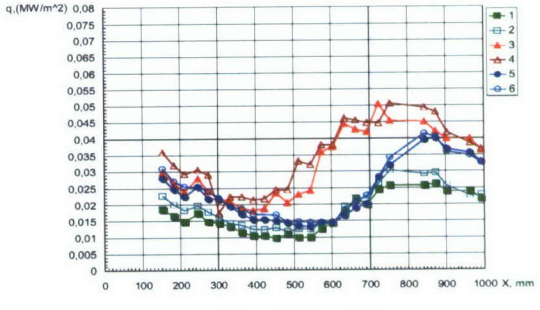

Nose R2, solid

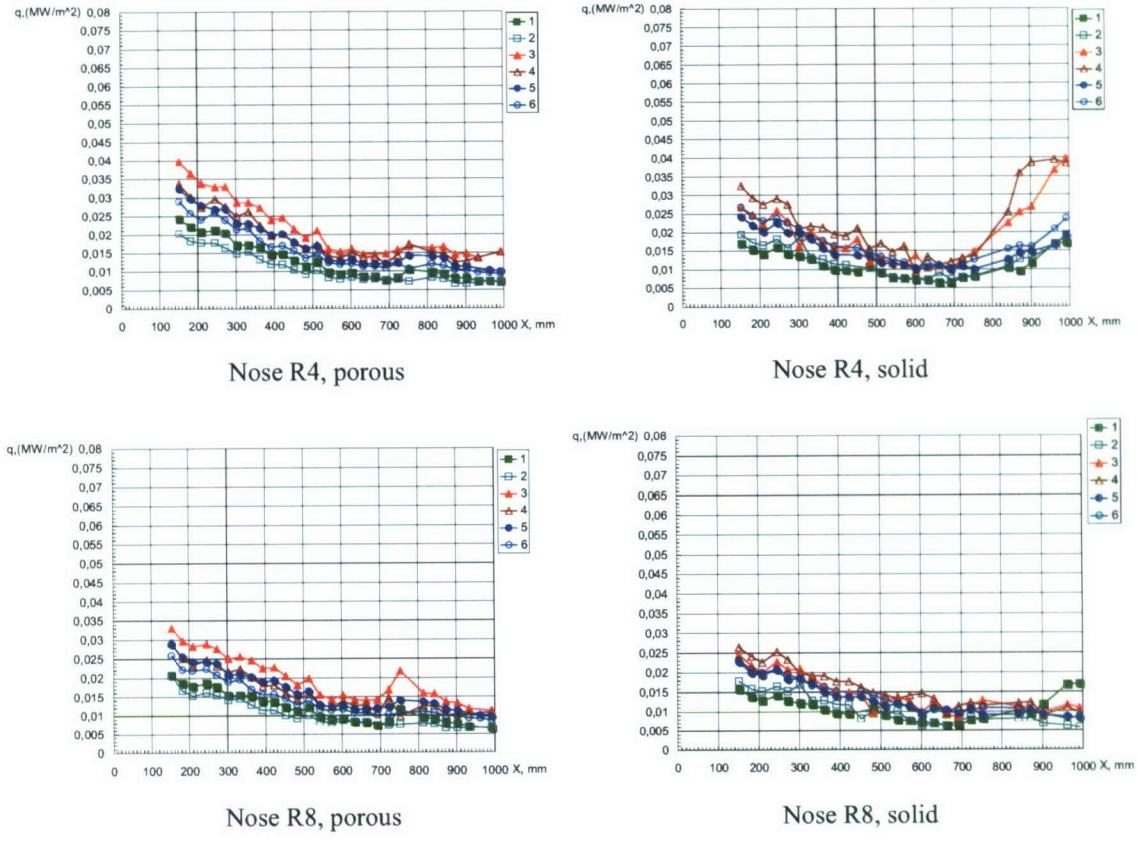

Fig. 5.9 Heat-flux distributions on porous (left) and solid (right) surface at different nose radii and Re= $Re_{1\infty}\cdot 10^6$ (m^{-1}); 1 – Re=4.1, θ=0°; 2 – Re=4.1, θ=180°; 3 – Re=5.2, θ=0°; 4 – Re=5.2, θ=180°; 5 – Re=3.5, θ=0°; 6 – Re=3.5, θ=180°.

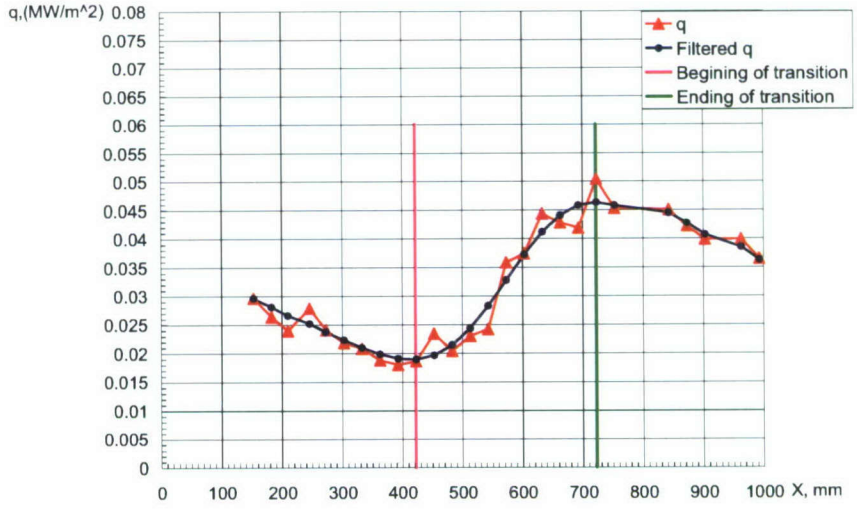

Fig. 5.10 Transition onset (vertical red) and transition end (vertical green line).

Dependences of the transition onset point (X_{trb}) and the transition end point (X_{tre}) on the free-stream unit Reynolds number ($\mathrm{Re}_{1\infty}$) are shown in Figs. 5.11 and 5.12, respectively. As expected, the transition loci decrease with increasing of $\mathrm{Re}_{1\infty}$ and increase with the bluntness radius. The transition Reynolds number $\mathrm{Re}_{trb} = X_{trb}\,\mathrm{Re}_{1\infty}$ and $\mathrm{Re}_{tre} = X_{tre}\,\mathrm{Re}_{1\infty}$ are shown in Figs. 5.13 and 5.14 as functions of $\mathrm{Re}_{1\infty}$. The Reynolds number Re_{trb} is approximately constant for small bluntness radii ($R = 0$ and $R = 1$ mm), while it increases with $\mathrm{Re}_{1\infty}$ for larger R. To evaluate the UAC-LFC performance, the ratio of transition end points, $X_{tre,porous} / X_{tre,solid}$, is shown in Fig. 5.15 for different nose bluntness radii. Despite some uncertainty of experimental data it is clear that the felt-metal coating causes significant (by a factor of 1.3-1.85) increase of the laminar run in the transitional cases.

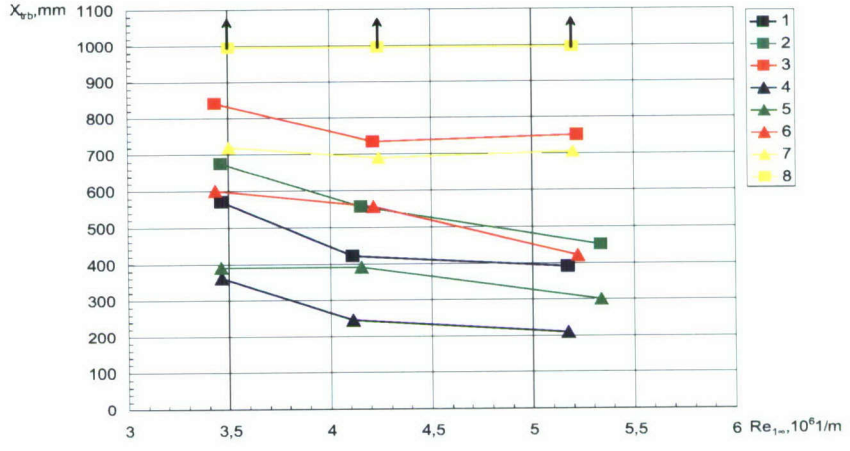

Fig. 5.11 Transition onset point (X_{trb}) as a function of unit Reynolds number $\mathrm{Re}_{1\infty}$; 1 – R0, porous surface ; 2 – R1, porous surface ; 3 – R2, porous surface ; 4 – R0, solid surface ; 5 – R1, solid surface ; 6 – R2, solid surface ; 7 – R4, solid surface ; 8 – R4, porous surface ; points with arrows – flow is laminar to the cone end.

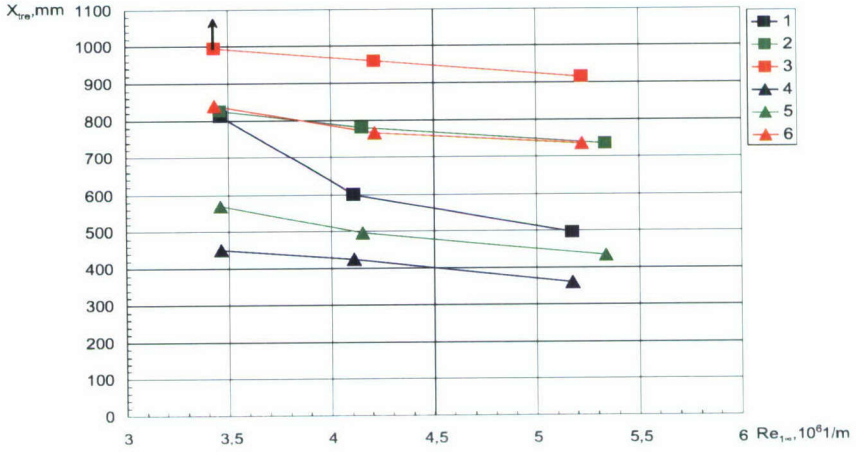

Fig. 5.12 Transition end point (X_{tre}) as a function of unit Reynolds number $\mathrm{Re}_{1\infty}$; 1 – R0, porous surface ; 2 – R1, porous surface ; 3 – R2, porous surface ; 4 – R0, solid surface ; 5 – R1, solid surface ; 6 – R2, solid surface; points with arrows – flow is laminar to the cone end.

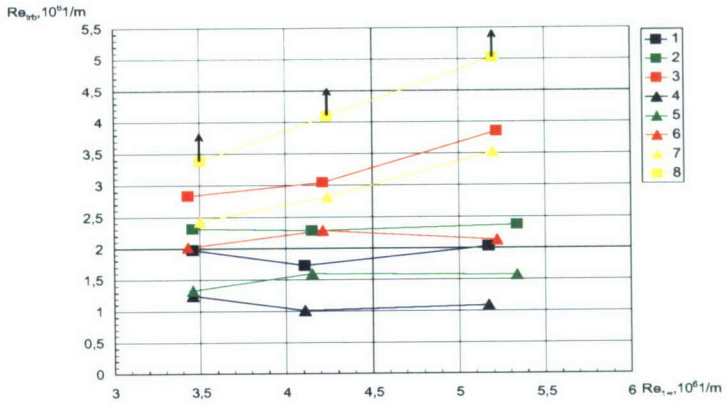

Fig. 5.13 Transition onset Reynolds number (Re_{trb}) versus $Re_{1\infty}$; 1 – R0, porous surface, 2 – R1, porous surface, 3 – R2, porous surface, 4 – R0, solid surface, 5 – R1, solid surface, 6 – R2, solid surface, 7 – R4, solid surface, 8 – R4, porous surface; points with arrows – flow is laminar to the cone end.

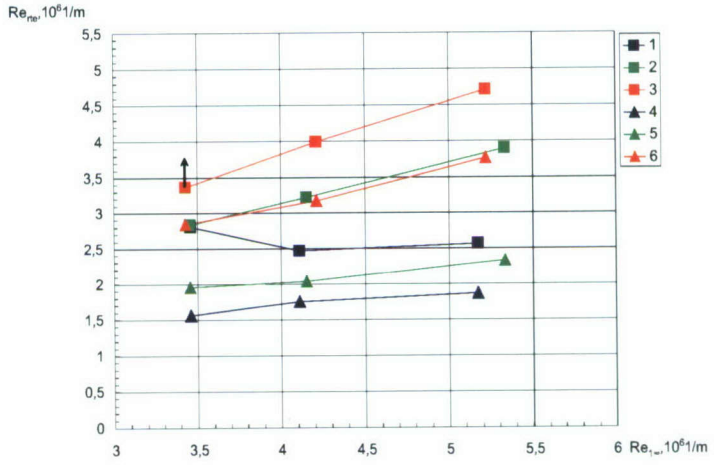

Fig. 5.14 Transition end Reynolds number (Re_{tre}) versus $Re_{1\infty}$; 1 – R0, porous surface, 2 –R1, porous surface, 3 – R2, porous surface, 4 – R0, solid surface, 5 – R1, solid surface, 6 – R2, solid surface ; points with arrows – flow is laminar to the cone end.

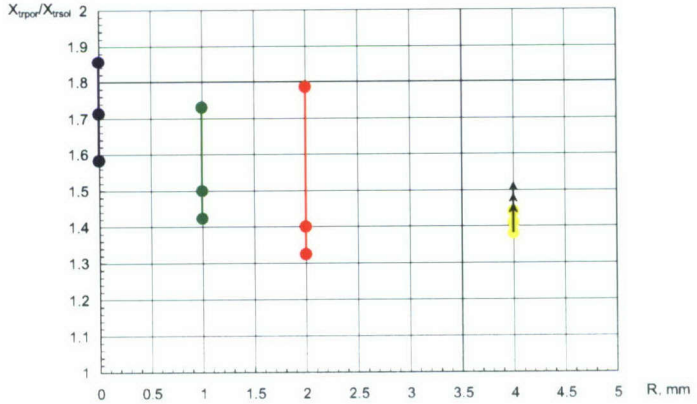

Fig. 5.15 Ratio of transition end points ($X_{tre,porous} / X_{tre,solid}$) versus bluntness radius R, points with arrows – flow is laminar to the cone end.

2.6. Mathematical modeling of acoustic properties of fibrous materials

In this section new approach is suggested for modeling of gas slow motions and propagation of acoustic disturbances in highly porous fibrous materials. The perturbations of gas parameters are assumed to consist of two components:

- The first is an exact solution of proper hydrodynamics problem averaged over the elementary cell volume. This macroscopic component varies on relatively large scales. Equations governing the average parameters are derived.
- The second is responsible for local perturbations nearby each fiber. Equations governing these perturbations are derived from first principles using rigorous mathematical methods.

These results are used for analysis of sound absorption by layered fibrous materials of high porosity. Corresponding mathematical problem is formulated, and its solution is expressed in terms of Fourier series.

2.6.1. Derivation of macroscopic equations for gas motion in a fibrous material

The problem of fluid motion in porous media is addressed in many papers and monographs. Review of basic and recent results obtained in the macroscopic porous media theory is given, for example, in Ref. [34]. More general cases of the heterogeneous media motion were discussed in Ref. [35]. Our analysis is based on the assumptions that widely used in the heterogeneous media theory (see Refs. [34, 35]):

1) Each constituent has sizes much larger than molecule-kinetic scales (in particular, the molecular mean free path)
2) The characteristic macroscopic size of a porous sample substantially exceeds the characteristic size of constituents
3) An independent state motion is assigned to each constituent. Hereafter it is assumed that the fibrous skeleton is rigid and fixed
4) Constituents are, on average, uniformly distributed over the sample volume
5) Each elementary volume within a porous sample is simultaneously occupied by each phase with corresponding probability

Up to day, semi-empirical dependencies are used for approximate description of acoustic properties of porous materials. Many of them are based on the analytical solution [36, 37] for an infinitely long round pipe. In this solution, the perturbations of velocity and temperature are decoupled. However, in the case of fibrous materials this approach is not valid. This motivates us to develop a mathematical model adequate to materials of this kind.

Gas motion within pores of a fibrous material with rigid skeleton is described by the fundamental equations of continuum mechanics written in the divergence form

$$\frac{\partial \rho}{\partial t} + \frac{\partial}{\partial x_j}\left(\rho u_j\right) = 0\,,$$

$$\frac{\partial \rho u_i}{\partial t} + \frac{\partial}{\partial x_j}\left(\rho u_i u_j - \sigma_{ij}\right) + \frac{\partial p}{\partial x_i} = 0\,,\ i = 1, 2, 3\,, \tag{6.1}$$

$$\frac{\partial \rho(u_i^2/2 + c_V T)}{\partial t} + \frac{\partial}{\partial x_j}\left\{\rho\left(u_i^2/2 + c_p T\right)u_j + q_j - u_i\sigma_{ij}\right\} = 0\,,$$

where ρ, p and T – gas density, pressure and temperature; $\mathbf{u}$ is vector of macroscopic gas velocity and u_i $(i=1,2,3)$ are its components in the Cartesian system of coordinates $\left(x_1, x_2, x_3\right)$; c_V and c_p – specific heat at constant volume and constant pressure, respectively; $\sigma_{ij} = 2\mu\left(e_{ij} - 1/3\,\delta_{ij}\mathrm{div}\mathbf{u}\right) + \zeta\delta_{ij}\mathrm{div}\mathbf{u}$ is viscous stress tensor (hereafter the term with bulk viscosity is omitted), δ_{ij} is Kronecker symbol, $e_{ij} = \frac{1}{2}\left(\frac{\partial u_i}{\partial x_j} + \frac{\partial u_j}{\partial x_i}\right)$ is the tensor of deformation rates, q_j is the heat flux vector. The summation convention is understood everywhere. The system (6.1) is supplemented with the state equation

$$p = \rho R_g T\,, \tag{6.2}$$

where R_g is gas constant per unit mass.

In accord with the aforementioned assumptions, the solid phase (fibers) is directly involved into the heat transfer only. The latter is governed by the heat conduction equation

$$\rho_s c_s \frac{\partial T_s}{\partial t} = \kappa_s \frac{\partial^2 T_s}{\partial x_i^2}, \tag{6.3}$$

where T_s is local temperature of the solid phase, ρ_s, c_s and κ_s is solid density, specific heat and heat-conductivity coefficient, respectively.

A porous sample is mentally subdivided into equal parallelepiped cells $\Delta x_1 \times \Delta x_2 \times \Delta x_3$ so that $a \ll \Delta x_1 \sim \Delta x_2 \sim \Delta x_3 \ll L_{\min}$, where a is the average fiber radius and $L_{\min}$ is the smallest characteristic size of the porous sample. Equations (6.1) are integrated over the cell porous volume that is a multi-connected domain. Accounting for no-slip condition on the fiber surfaces, we obtain

$$\phi V_{\text{cell}} \frac{\partial \overline{\rho}}{\partial t} = -\int_{S_{\text{cell}}} \rho u_j n_j dS_{\text{cell}}\,, \tag{6.4}$$

$$\phi V_{\text{cell}} \frac{\partial}{\partial t}\overline{\rho u_i} = -\int_{S_{\text{cell}}} \left\{\rho u_i u_j + p\delta_{ij} - \sigma_{ij}\right\} n_j dS_{\text{cell}} - \\ -\sum_k \int_{S_{\text{fib},k}} \left\{p\delta_{ij} - \sigma_{ij}\right\} n_{j,k} dS_{\text{fib},k}\,,\ i = 1,2,3\,, \tag{6.5}$$

$$\phi V_{\text{cell}} \frac{\partial}{\partial t}\overline{\rho\left(u_i^2/2 + c_V T\right)} = -\int_{S_{\text{cell}}} \left\{\rho u_j \left(u_i^2/2 + c_P T\right) + q_j\right\} n_j dS_{\text{cell}} + \\ +\int_{S_{\text{cell}}} u_i \sigma_{ij} n_j dS_{\text{cell}} - \sum_k \int_{S_{\text{fib},k}} q_j n_{j,k} dS_{\text{fib},k}\,, \tag{6.6}$$

where ϕ – porosity averaged over the porous material volume, $\int_{S_{\text{cell}}} \ldots n_j dS_{\text{cell}}$ – integral over the solid-free parts of the cell lateral surfaces, n_j – j^{th} component of the external normal to the cell surface, $n_{j,k}$ – j^{th} component of the external normal to the surface of k^{th} fiber sections falling into the cell, the overbar denotes averaging over the cell volume $V_{\text{cell}} = \Delta x_1 \times \Delta x_2 \times \Delta x_3$. The

integrals $\int_{S_{\text{fib},k}} \ldots n_{j,k} dS_{\text{fib},k}$ are taken over all surfaces of the fiber sections falling into the cell, the sums $\sum_k \int_{S_{\text{fib},k}} \left\{ p\delta_{ij} - \sigma_{ij} \right\} n_{j,k} dS_{\text{fib},k}$ and $\sum_k \int_{S_{\text{fib},k}} q_j n_{j,k} dS_{\text{fib},k}$ represent the resultant force acting on viscous gas on the fiber surfaces and the heat flux absorbed or emitted through surfaces of fiber sections falling into the cell, respectively.

The surface integrals are expressed via the surface averages

$$\int_{S_{\text{cell}}} B_j n_j dS_{\text{cell}} = \alpha_j \left\langle B_j \right\rangle n_j \Delta S_{\text{cell}}, \tag{6.7}$$

where the dimensionless coefficient α_j represents the average fraction of area of the solid-free part to the total area ΔS_{cell} of the cell facet with the normal n_j, $\langle\ \rangle$ – averaging over the solid-free lateral surfaces of the cell. As shown in Ref. [35] (pp. 65-66), a surface average can be approximately replaced by corresponding volume average as

$$\int_{S_{\text{cell}}} B_j n_j dS_{\text{cell}} \approx \phi \overline{B}_j n_j \Delta S_{\text{cell}}. \tag{6.8}$$

Since the cell sizes are much smaller than the characteristic macroscopic scale $L_{\min}$, the sum in the right-hand side of (6.8) can be approximated as

$$\phi \overline{B}_j n_j \Delta S_{\text{cell}} \approx V_{\text{cell}} \frac{\partial}{\partial x_j} \left(\phi \overline{B}_j \right) \left\{ 1 + O\left(L_{\text{cell}} / L_{\min} \right) \right\}, \tag{6.9}$$

where L_{cell} is maximal characteristic length scale of pores. The sum of integrals $\sum_k \int_{S_{\text{fib},k}} \left\{ p\delta_{ij} - \sigma_{ij} \right\} n_{j,k} dS_{\text{fib},k}$ in the right-hand side of (6.5) is responsible for the resultant resistance force produced by all fiber sections in the cell. For internal flows of small velocity, this sum is approximated as

$$\sum_k \int_{S_{\text{fib},k}} \left\{ p\delta_{ij} - \sigma_{ij} \right\} n_{j,k} dS_{\text{fib},k} \approx V_{\text{cell}} \hat{R}'_{ij} \overline{\overline{u}}_j, \tag{6.10}$$

where R'_{ij} are components of the hydrodynamic resistance tensor of porous media, $\overline{\overline{u}}_j = \overline{\rho u_j} / \overline{\rho}$ is mass-average j^{th} component of the velocity vector (such averaging is denoted hereafter by the doubled overbar). In general, both gas-flow deflections from a straight-line motion in pores and viscous-friction forces acting on fiber surfaces affect the magnitude of (6.10).

The aforementioned results allow us to formulate approximate differential laws of mass and momentum conservation. The energy equation should account for the heat transfer by gas and fibers including the energy interchange between these phases. To derive this equation one should additionally perform integration over the volume of all fiber sections falling into the cell

$$(1-\phi)\rho_s c_s V_{\text{cell}} \frac{\partial \overline{T}_s}{\partial t} \approx -\kappa_s \left\{ \sum_k \int_{S_{\text{fib},k}} \frac{\partial T_s}{\partial x_j} n_{j,k} dS_{\text{fib},k} + \sum_m \int_{S_{\text{fib},m}} \frac{\partial T_s}{\partial x_j} n_{j,m} dS_{\text{sec},m} \right\}, \tag{6.11}$$

where the normal $\mathbf{n}_k$ is directed outward the integration domain (it is the same as in (6.5)-(6.6)) and the sum $-\kappa_s \sum_m \int_{S_{\text{sec},m}} \frac{\partial T_s}{\partial x_j} n_{j,m} dS_{\text{sec},m}$ accounts for the heat interchange between neighboring cells through the imaginary solid boundaries (imaginary cross-sections) inside common fibers.

The normal component of the heat flux on the solid surfaces should be continuous

$$\sum_k \int_{S_{\text{fib},k}} q_j n_{j,k} dS_{\text{fib},k} = -\kappa_s \sum_k \int_{S_{\text{fib},k}} \frac{\partial T_s}{\partial x_j} n_{j,k} dS_{\text{fib},k} \,. \tag{6.12}$$

Accounting for (6.12) we summate term by term the equations (6.6) and (6.11) and obtain

$$V_{\text{cell}} \left\{ \phi \frac{\partial}{\partial t} \overline{\rho \left(u_i^2/2 + c_V T \right)} + (1-\phi)\rho_s c_s \frac{\partial \overline{\overline{T}}}{\partial t} \right\} = -\int_{S_{\text{cell}}} \left\{ \rho u_j \left(u_i^2/2 + c_P T \right) + q_j \right\} n_j dS_{\text{cell}} +$$

$$+ \int_{S_{\text{cell}}} u_i \sigma_{ij} n_j dS_{\text{cell}} - \kappa_s \sum_m \int_{S_{\text{fib},m}} \frac{\partial T_s}{\partial x_j} n_{j,m} dS_{\text{sec},m} + (1-\phi)\rho_s c_s V_{\text{cell}} \frac{\partial}{\partial t} \left(\overline{\overline{T}} - \overline{T}_s \right). \tag{6.13}$$

The averaged temperatures of gas $\overline{\overline{T}}$ and solids $\overline{T}_s$ and their gradients within the cell can be functions of time with different temporal rates. In general, these temperatures are different. However, our qualitative analysis shows that the last term in the right-hand side of (6.13) can be omitted in the problem relevant to acoustic disturbances in fibrous materials.

The terms in the right-hand side of (6.13), which are responsible for the heat transfer between neighboring cells, can be approximated as

$$\int_{S_{\text{cell}}} q_j n_j dS_{\text{cell}} + \kappa_s \sum_m \int_{S_{\text{fib},m}} \frac{\partial T_s}{\partial x_j} n_{j,m} dS_{\text{sec},m} \approx V_{\text{cell}} \frac{\partial q_j}{\partial x_j}, \tag{6.14}$$

where q_j – j^{th} component of the heat flux vector averaged over the cell volume. We assume that the average heat flux is expressed via the gradient of average cell temperature $\nabla \overline{\overline{T}}$ as

$$q_i = -\hat{\mathrm{K}}_{ij} \frac{\partial \overline{\overline{T}}}{\partial x_j}, \tag{6.15}$$

where $\hat{\mathrm{K}}_{ij}$ are components of the effective thermal conductivity tensor. This tensor should account for the heat transfer through gas and solid phases and the thermal interaction between cells (see Ref. [38]).

The foregoing approximations lead to the system of equations for the gas characteristics averaged over the cell volume (overbars denoting this averaging are omitted)

$$\phi \frac{\partial \rho}{\partial t} = -\frac{\partial \phi \rho u_j}{\partial x_j}, \tag{6.16}$$

$$\phi \rho \frac{Du_i}{Dt} = -\frac{\partial \phi p}{\partial x_i} - \hat{R}'_{ij} u_j + \frac{\partial \sigma_{ij}}{\partial x_j}, \; i = 1, 2, 3, \tag{6.17}$$

$$\phi\rho c_V \frac{DT}{Dt} + (1-\phi)\rho_s c_s \frac{\partial T}{\partial t} = -\phi p \frac{\partial u_j}{\partial x_j} + \hat{R}'_{ij} u_i u_j + \mu_{\text{ef}} \Phi + \frac{\partial}{\partial x_i}\left(\hat{\mathrm{K}}_{ij} \frac{\partial T}{\partial x_j}\right), \tag{6.18}$$

where $\frac{D}{Dt} = \frac{\partial}{\partial t} + u_j \frac{\partial}{\partial x_j}$ is the substantial derivative, μ_{ef} is effective viscosity, Φ is dissipative function.

Note that the tensors $\hat{R}'_{ij}$ and $\hat{\mathrm{K}}_{ij}$ as well as the effective viscosity coefficient μ_{ef} cannot be determined in the considered framework. This could be done using experimental measurements or additional theoretical analyses.

2.6.2. Mathematical model for highly porous fibrous materials

The tensors $\hat{R}'_{ij}$, $\hat{\mathrm{K}}_{ij}$ and the effective viscosity coefficient μ_{ef} can be evaluated in the case of highly porous media ($\phi \to 1$) as follows.

Consider a fibrous material that is formed by randomly placed rigid fibers of circular cross section. The fibers are stacked in mutually parallel planes. We assume that a plane monochromatic acoustic wave propagates perpendicular to these planes. A fibrous material is characterized by its structural geometry, average density ρ_m, fiber mass density ρ_s, and average fiber radius a. Using these parameters we can determine:

average fiber length per unit volume $$l = \frac{\rho_m}{\pi a^2 \rho_s}, \tag{6.19}$$

porosity $$\phi = 1 - \pi a^2 l = 1 - \frac{\rho_m}{\rho_s}, \tag{6.20}$$

specific area of fiber surface (without taking into consideration the area of butt-ends)

$$s_f \approx 2\pi a l = \frac{2\rho_m}{a\rho_s} = \frac{2}{a}(1-\phi), \tag{6.21}$$

average distance between axes of neighboring parallel fibers stacked in one plane

$$h = \frac{\pi a}{2(1-\phi)}. \tag{6.22}$$

Now we can estimate terms in the system (6.16)-(6.18). In the vicinity of fibers submerged into uniform cross flow, the viscous terms in the momentum equation are $\sim \mu u^* / a^2$, where u^* – characteristic velocity of gas inside porous material. Far from a fiber (at a distance h from its axis) these terms are $\sim \mu u^* / h^2 \sim \mu u^* (1-\phi)^2 / a^2$. The terms $\hat{R}'_{ij} u_j$ in the averaged momentum equation (6.17) are estimated as

$$\hat{R}'_{ij}u_j \sim \mu\left(\frac{u^*}{a}\right)s_f \sim \frac{\mu u^*}{a^2}(1-\phi)\,. \tag{6.23}$$

They are responsible for an effective force that is continuously distributed over the volume of gas filling pores. This volumetric (dumping) force is directly related to the viscous friction on the surfaces of solid elements and to the local gas-flow deflections from a straight-line motion in pores. In accord with (6.23), the characteristic length scale $L_d = a/\sqrt{1-\phi}$ represents a distance from the fiber axis at which the volume dumping force and the viscous force are of the same order of magnitude. Thus, to solve the problem we need the differential equations valid on the length-scales from a to L_d. To derive these equations we decompose the flow parameters in the vicinity of a fiber as

$$F = \overline{F} + F'\,, \tag{6.24}$$

where $\overline{F}$ denotes an unknown function in the equations (6.16)-(6.18), F' is local perturbation of F. We also assume that $\overline{F}$ substantially vary only on the "macroscopic" scale L, which is much larger than L_d

$$L \gg L_d \gg a\,. \tag{6.25}$$

In this case, we have $\partial\overline{F}/\partial x_j \ll \partial F'/\partial x_j$. Substituting the decompositions (6.24) into the exact Navier-Stockes equations, using approximate equations (6.16)-(6.18) for simplification and omitting terms $\sim \partial\overline{F}/\partial x_j$ we obtain

$$\frac{\partial\rho'}{\partial t} = -\overline{\rho}\frac{\partial u'_j}{\partial x_j} - \overline{u}_j\frac{\partial\rho'}{\partial x_j} - \frac{\partial\rho' u'_j}{\partial x_j}\,, \tag{6.26}$$

$$\left(\overline{\rho}+\rho'\right)\left\{\frac{\partial u'_i}{\partial t} + \left(\overline{u}_j + u'_j\right)\frac{\partial u'_i}{\partial x_j}\right\} + \rho'\frac{\partial\overline{u}_i}{\partial t} = -\frac{\partial p'}{\partial x_i} + $$

$$+\phi^{-1}\hat{R}'_{ij}\overline{u}_j + \mu\frac{\partial^2 u'_i}{\partial x_j^2},\ i=1,2,3\,, \tag{6.27}$$

$$\left(\overline{\rho}+\rho'\right)c_p\frac{\partial T'}{\partial t} + \left\{\rho' c_p - \frac{1-\phi}{\phi}\rho_s c_s\right\}\frac{\partial\overline{T}}{\partial t} + \left(\overline{\rho}+\rho'\right)c_p\left(\overline{u}_j+u'_j\right)\frac{\partial T'}{\partial x_j} =$$

$$= \frac{1-\phi}{\phi}\rho_s c_s\lambda_j\frac{\partial^2\overline{T}}{\partial t\partial x_j} + \frac{\partial p'}{\partial t} + \left(\overline{u}_j+u'_j\right)\frac{\partial p'}{\partial x_j} - \phi^{-1}\hat{R}'_{ij}\overline{u}_i\overline{u}_j + \mu\Phi' + \frac{\partial}{\partial x_i}\left(\kappa\frac{\partial T'}{\partial x_i}\right), \tag{6.28}$$

where the approximation $\dfrac{\partial}{\partial t}(T-T_s) \approx -\lambda_j\dfrac{\partial^2\overline{T}}{\partial t\partial x_j}$ is used, λ_j are components of a constant vector.

Note that the term $\phi^{-1}\hat{R}'_{ij}\overline{u}_j$ in the momentum equation (6.27) and the term $\phi^{-1}\hat{R}'_{ij}\overline{u}_i\overline{u}_j$ in the energy equation (6.28) are associated with Darcy law. However, they have opposite sign compared with the similar term in Darcy law: $\Delta p = -\hat{k}\mu\overline{u}$, where $\hat{k}$ is permeability. Brinkman [39] was the first who has included the term $-\hat{k}\mu\overline{u}$ into Newton's law of viscous friction relevant to flow through a porous medium. His phenomenological model has been used by many authors. Our analysis rigorously substantiates the Brinkman's term and clarifies conditions at which the Brinkman's model is valid.

2.6.3. Acoustic problem for highly porous layered fibrous materials and its general solution

Consider propagation of sound through highly porous media. In this case the system of equations (6.26)-(6.28) can be linearized as

$$\frac{\partial \rho'}{\partial t} + \rho_0 \frac{\partial u'_j}{\partial x_j} = 0, \tag{6.29}$$

$$\rho_0 \frac{\partial u'_i}{\partial t} + \frac{\partial p'}{\partial x_i} = \phi^{-1}\hat{R}'_{ij}\overline{u}_j + \mu \frac{\partial^2 u'_i}{\partial x_j^2}, \; i = 1, 2, 3, \tag{6.30}$$

$$\rho_0 c_p \frac{\partial T'}{\partial t} = \frac{\partial p'}{\partial t} + \kappa \frac{\partial^2 T'}{\partial x_j^2}, \tag{6.31}$$

$$\frac{p'}{p_0} = \frac{\rho'}{\rho_0} + \frac{T'}{T_0}, \tag{6.32}$$

where the subscript 0 stands for unperturbed quantities.

For layered fibrous materials of highly porosity, in the leading order approximation it is sufficient to consider flow past an isolated fiber (an infinitely long cylinder of radius a) placed perpendicular to uniform flux with effective parameters that correspond to the averaged quantities $\overline{F}$ in (6.24). Using the equations (6.29)-(6.32) and assuming that the dissipative effects are important, we obtain the length scale associated with the thickness of viscous Stokes layer

$$\delta_{\text{visc}} = \sqrt{\mu/\rho_0\omega} \sim a, \tag{6.33}$$

where ω is angular frequency of acoustic wave. Comparing terms of the linearized momentum equation (6.30) we obtain

$$p' \sim \frac{\mu u'}{a} \sim \frac{\mu}{\rho_0 c_0 a}\rho_0 c_0 u' \sim \left(\frac{\mu}{\rho_0 \omega a^2}\right)(k_0 a)\rho_0 c_0 u', \tag{6.34}$$

where $k_0 = \omega / c_0$ is wave number, $\rho_0 c_0$ is the acoustic impedance. Using (6.33) and the definition of compressibility $\tilde{C}$ we get

$$\frac{\rho'}{\rho_0} = \tilde{C}p' \sim \frac{p'}{\gamma p_0} \sim \frac{p'}{p_0}, \tag{6.35}$$

The energy equation (6.31) gives

$$\frac{\partial p'}{\partial t}\Big/\kappa\frac{\partial^2 T'}{\partial x_j^2}\sim\frac{\Pr\rho_0\omega a^2}{\mu}\frac{p'}{p_0}\Big/\frac{T'}{T_0}\sim O(1)\,, \tag{6.36}$$

Comparison of the dominant terms in (6.35) leads to

$$\frac{1}{\rho_0}\frac{\partial\rho'}{\partial t}\Big/\frac{\partial u_j'}{\partial x_j}\sim\left(\frac{\mu}{\rho_0\omega a^2}\right)(k_0 a)^2\ll 1\,. \tag{6.37}$$

Thus, the continuity equation (6.29) on scales $\sim a$ is reduced to the incompressible form

$$\frac{\partial u_j'}{\partial x_j}=0\,, \tag{6.38}$$

while Equations (6.30)-(6.32) remain the same.

To find a general solution of the foregoing problem, we consider velocity perturbation $\mathbf{u}'$ in the form $\mathbf{u}'\exp(i\omega)$ and express the amplitude $\mathbf{u}'$ as

$$\mathbf{u}'=\mathrm{grad}\varphi'+\mathrm{rot}\mathbf{A}'\,, \tag{6.39}$$

where the velocity potential amplitude φ' satisfies the continuity equation of incompressible fluid

$$\Delta\varphi'=0\,, \tag{6.40}$$

and the vector potential amplitude $\mathbf{A}'$ satisfies the Helmholtz equation

$$\left(\Delta+k^2\right)\mathbf{A}'=0\,, \tag{6.41}$$

$k^2=-i\omega\rho_0/\mu$ is squared complex wave number, and Δ is Laplacian.

Introduce the polar coordinate system $\left(r=\sqrt{x_1^2+x_2^2},\theta\right)$, where r is measured from the fiber axis. The equation (6.30) leads to the relation

$$p'=\mu k^2\varphi'+\phi^{-1}R_\perp'\,|\overline{\mathbf{u}}|\,r\cos\theta\,, \tag{6.42}$$

where $R_\perp'$ denotes flow resistance in the direction perpendicular to the fiber layers.

Since the flow disturbance past an isolated fiber should be symmetric with respect to the direction of uniform flow, solutions of the equations (6.40) and (6.41) can be expressed in terms of Fourier series

$$\varphi'=a_0+\sum_{n=1}^{\infty}\left(a_n r+b_n r^{-n}\right)\cos n\theta\,, \tag{6.43}$$

$$A_3'=\sum_{n=1}^{\infty}\left[c_n J_n(kr)+d_n H_n^{(2)}(kr)\right]\sin n\theta\,, \tag{6.44}$$

where a_n, b_n, c_n, d_n – constants, $J_n(kr)$– Bessel functions of n^{th} order and first kind, $H_n^{(2)}(kr)$ – Henkel functions of n^{th} order and second kind. Note that the vector potential $\mathbf{A}'$ has only one non-zero component A_3' in the case of two dimensional flow.

The solutions (6.43) and (6.44) should satisfy to the no-slip condition on the cylinder surface

$$\overline{\mathbf{u}} + \mathbf{u}'(a,\theta) = 0\,. \tag{6.45}$$

Instead of non-reflection conditions at the infinity, we should impose additional restrictions associated with the decomposition (6.24). Namely, perturbations of all unknowns F' should not contribute to the corresponding averages

$$0 = \int\limits_{V_{\text{cell}} \setminus V_c} F' dV \approx \int\limits_0^{2\pi} \int\limits_a^{R_{\text{cell}}} F' r d\theta dr\,, \tag{6.46}$$

where R_{cell} is radius of an equivalent coaxial cylindrical domain with the cell volume $V_{\text{cell}} = 2ah^2 = \pi R R_{\text{cell}}^2 h$.

Equations (6.31), (6.39) and (6.42) indicate that the temperature perturbations T' are coupled with the velocity perturbation $\mathbf{u}'$. Note that this coupling was not taken into account in the analysis of Ref. [40].

Substitution of (6.43)-(6.44) into (6.39) gives

$$u_r' = r^{-1}\left\{a_0 + \sum_{n=1}^{\infty} n\left(a_n r^n - b_n r^{-n} + c_n J_n(kr) + d_n H_n^{(2)}(kr)\right)\cos n\theta\right\}, \tag{6.47}$$

$$u_\theta' = -\sum_{n=1}^{\infty}\left\{n r^{-1}\left(a_n r^n + b_n r^{-n}\right) + k\left[c_n \dot{J}_n(kr) + d_n \dot{H}_n^{(2)}(kr)\right]\right\}\sin n\theta\,, \tag{6.48}$$

where the dot over symbol denotes the differentiation over the function argument.

The boundary condition (6.45) leads to the system of linear algebraic equations for the unknown coefficients

$$a_0 = 0\,, \tag{6.49}$$

$$a_n a^n - b_n a^{-n} + c_n J_n(\Lambda) + d_n H_n^{(2)}(\Lambda) = -\delta_{1n} a n^{-1} |\overline{\mathbf{u}}|\,, \tag{6.50}$$

$$a_n a^n + b_n a^{-n} + n^{-1}\Lambda\left(c_n J_n'(\Lambda) + d_n H_n'^{(2)}(\Lambda)\right) = -\delta_{1n} n^{-1} a |\overline{\mathbf{u}}|\,, \tag{6.51}$$

where δ_{1n} is Kronecker symbol, $\Lambda = ka$. Note that the expressions for u_r', u_θ' and p' satisfy the condition (6.46).

Equation (6.31) is non-uniform. Its solution consists of the solution of corresponding uniform equation and a partial solution. Besides (6.46), it should satisfy to the condition of normal heat flux continuity across the cylinder surface. The proper expressions will be derived in future.

2.7. Development of ceramic UAC

One of the objectives of this program was to develop and demonstrate a method for fabricating UACs on test panels of a ceramic thermal protection material with dimensions ~6 in. x 6 in., as well as to perform benchmark measurements of ultrasonic absorption and other relevant mechanical properties of these panels. This provides a direct link to the UAC modeling and the wind-tunnel testing of metallic UAC.

The choice of materials and processing methods was constrained to those that could be reasonably scaled up in a follow-on program to manufacture large panels, or arrays of panels, for testing in wind-tunnels and in flight. Space-shuttle tiles were selected as substrates (Fig. 7.1). These tiles consist of rigid fibrous silica insulation covered with a smooth dense surface layer of reaction-cured glass. The UAC was formed on top of the dense surface layer by a stamping process, using a reaction cured glass with composition similar to the surface layer of the tile. This approach ensured matching thermal expansion properties in the UAC and substrate, thus avoiding potential difficulties with cracking due to thermal expansion mismatch.

We note that the effectiveness of UAC coatings on tiles is not diminished by the presence of steps and gaps between adjacent tiles when scaling up to arrays of tiles in a vehicle TPS system. As discussed in section 1, roughness-induced transition at steps and gaps between tiles is suppressed under hypersonic flight conditions with high local Mach numbers on the vehicle surface, while second mode instabilities, which are reduced by the UAC, become dominant.

The development effort was focused on coatings with porosity resembling an ideal geometry of regularly spaced blind cylindrical holes in the pattern of Fig. 1.1, with diameter ~100 – 200 μm, depth ~500 μm, and spacing ~300 μm.

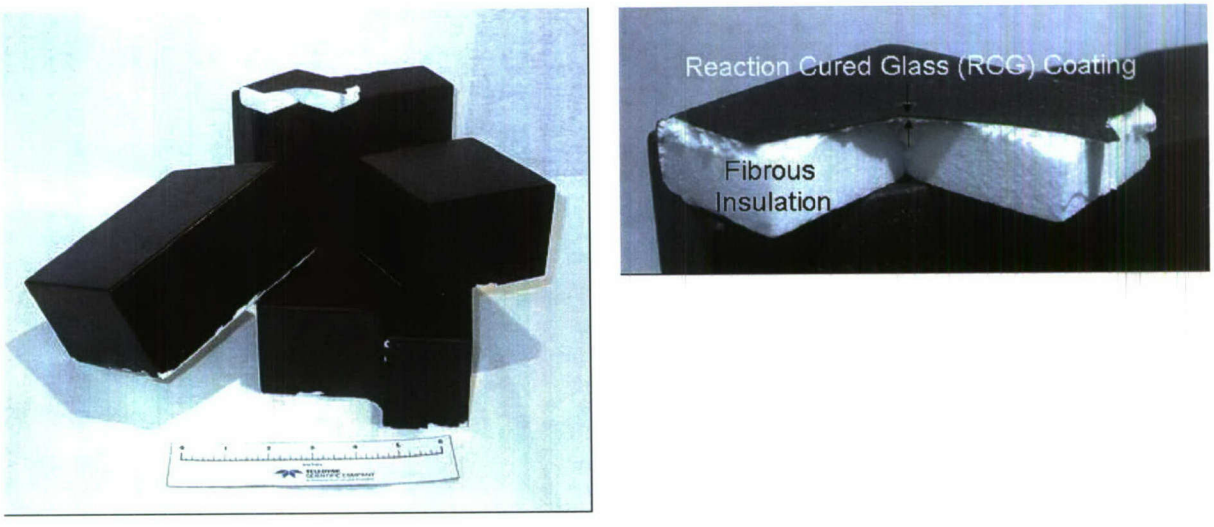

Fig. 7.1 Shuttle tiles for use as substrates for UAC.

The major steps of the fabrication process are shown in Figs. 7.2 and 7.3. Laser-drilled stainless steel plates (Fig. 3.4) were used as masters to fabricate molds for stamping the desired hole patterns on the tile surface. The plates are approximately 0.5 mm thick and the holes were tapered through the thickness, with diameter approximately 200 μm on one side and 100 μm on the other. The plates were covered with mold release agent (Miller-Stephenson MS-122/22) and a liquid polymer film was spread over the side of the plate with the larger hole diameter (Fig. 7.2a). Several types of polymer were investigated, including epoxy, thermal plastics and silicone rubber. The sample was then placed between sheets of Teflon release film and a roller was used to force the polymer through the holes and flatten the excess polymer on both sides of the plate. After curing (or thermally setting), the polymer that had extruded through the holes was removed using a razor blade (Fig. 7.2b) and the remaining polymer sheet on the other side of the plate was peeled from the surface of the plate yielding a "negative" structure with protruding posts, as shown in Fig. 7.4. In some cases a woven nylon monofilament fabric was embedded in the polymer sheet after it was spread on the surface of the plate to reinforce the polymer and increase its elastic stiffness, which aided in the removal of the posts from the holes without tearing.

The UAC was then formed by spreading a RCC slurry on the tile surface and stamping with the polymer mold (Fig. 7.3). The slurry was supplied by the Boeing Company. In the as-received state, the RCG slurry had a viscosity similar to water, which was too low for use in a stamping process. Therefore, the slurry was reformulated with a binder. This involved first drying the slurry then mixing with a polysiloxane resin in an acetone carrier. As the acetone evaporated, the mixture became semi-rigid. However, with slight heating (to ~75°C) the flow stress was reduced sufficiently to allow compression molding. To form the UAC coating, the slurry was spread over the tile surface and the acetone was evaporated. The tile was then covered with Teflon release film and placed in a heated platen press. The press was used to flatten the coating and ensure it was of uniform thickness. The release film was then removed and replaced with the polymer master stamp to produce holes in the coating (see Fig. 7.3b). Once the part cooled completely, the stamp was removed from the surface cleanly (Fig. 7.3c) leaving the green coating with the required cylindrical holes.

The coated tiles were then heat treated for densification and curing. Initially, trials were conducted to establish suitable sintering temperatures and times that would permit sufficient flow for densification without cracking and for adherence to the substrate, while allowing the shape of the cylindrical holes to be retained. For these trials, fugitive organic particles of diameter 50 μm were added to the slurry, which was then spread on the tile surface and heat treated for various temperature/time cycles. From the initial trials, a heat treatment temperature of 1250°C was needed to achieve flow of the coating and sintering times shorter than two hours were needed to maintain the holes. Stamped coatings after sintering under these conditions are shown in Fig 7.5.

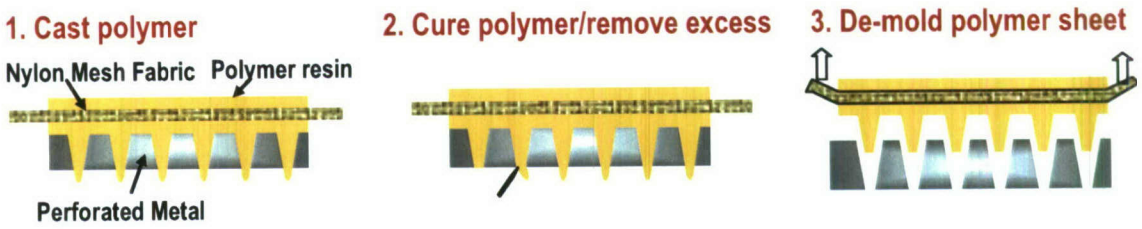

Fig. 7.2 Steps of the polymer stamp fabrication.

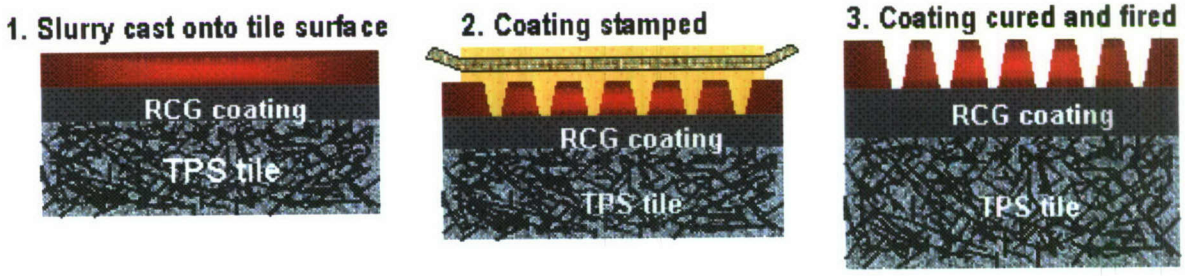

Fig. 7.3 Steps of ceramic UAC fabrication.

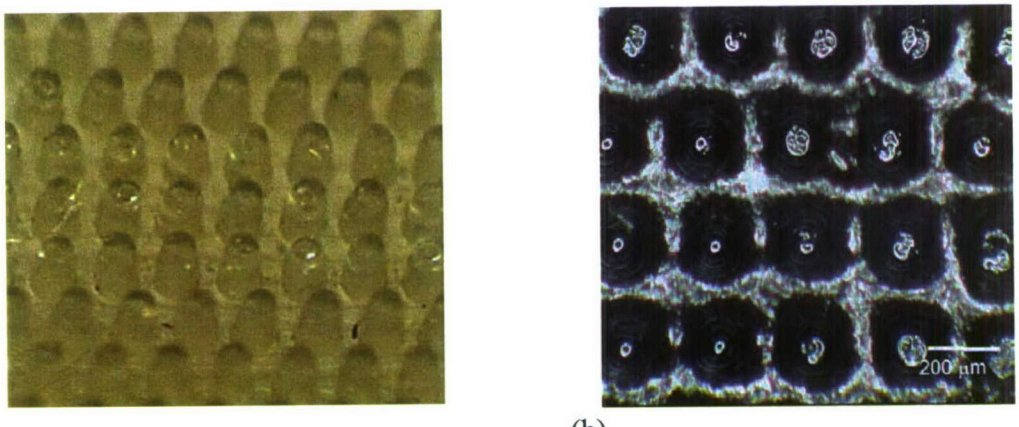

(a) (b)

Fig. 7.4 (a) Polymer stamp. (b) Stamped RCG slurry coating

The array of holes in Fig. 7.5 closely approximate the ideal configuration discussed in Sect. 2.1. Minor departures include slight rounding around the tops of the holes, some distributed surface roughness (with amplitude smaller than the hole diameter and much smaller than the hole depth)

and a shape of truncated cone rather a uniform cylinder. Refinement of the processing conditions could reduce the surface roughness and rounding of the edges. However, from experience with felt metal coatings, which have larger surface roughness, and other considerations, we expect that the effects of surface roughness at this level and rounding of the edges of the holes on UAC performance will be minor. Likewise, the sensitivity to the tapered hole shape is expected to be secondary (analysis of the sensitivity to taper angle was initiated at Cal Tech). These expectations need to be confirmed by future benchmark (no-flow) and wind-tunnel experiments.

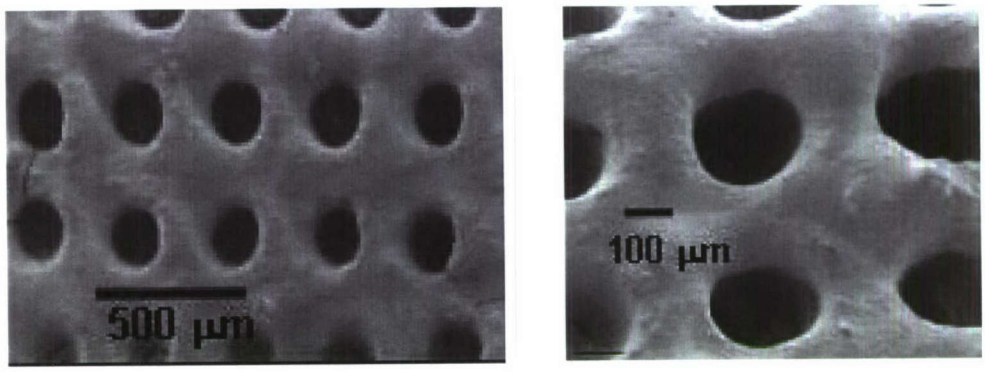

Fig. 7.5 Ceramic UAC formed in a layer of reaction-cured glass (RCG) on space shuttle tile. Hole diameter 100-200 μm, spacing 300 μm, depth 560 μm.

3. Summary and impact of effort

The foregoing theoretical, numerical and experimental studies of ultrasonically absorptive coatings for laminarization of hypersonic boundary-layer flows are summarized as follows:

1) To aid in the design of the porous coating to be tested on a 7-degree half-angle sharp cone in the CUBRC LENS I shock tunnel, parametric studies of the UAC-LFC performance were conducted for the Mach=7 and Mach=10 free-stream conditions.

   a) To calibrate and verify our stability and transition prediction tools we analyzed the transition onset data measured in the LENS I tunnel. Using our reduced-order computational package that includes the compressible Blasius mean flow and the local-parallel linear stability solver, we calculated *N*-factors for the second mode and compared them with the predictions of STABL at Mach=10 free-stream conditions. Strikingly, our results agree very well with those of STABL. This opened up an opportunity to conduct quick turn-around parametric computations of the transition onset point and search for optimal UAC parameters.

   b) Parametric stability calculations were carried out for the uncoated (solid) and coated (porous) wall. The UAC of regular microstructure comprises equally spaced vertical cylindrical blind micro-holes of fixed radius r^*, depth h^* and spacing s^*. It was shown that the coating of $r^* = 25$ μm, $s^* = 100$ μm and $h^* \approx 10r^*$ massively suppresses the

second-mode instability and can lead to significant (more than twice) increase of the laminar run under Mach=7 and Mach=10 free-stream conditions.

c) Estimates of the UAC roughness effect showed that this coating can be treated as aerodynamically smooth in the unit Reynolds number range required for transition experiments. The coating with the aforementioned r^*, s^* and depth $h^* = 300$ μm is recommended for testing in the CUBRC LENS I shock tunnel.

d) It was shown that the UAC-LFC performance strongly increases with porosity. In this connection, it is suggested to investigate a rectangular or honeycomb patterns, which allow for coatings of substantially higher porosity compared with cylindrical pores of circular cross-sections.

2) Two-dimensional DNS of hypersonic boundary layer stability was carried out for a flat plate and sharp cone at zero angle of attack. Both solid and porous walls were treated. The boundary conditions on UAC surface are formulated using the theoretical model.

For a flat-plate in Mach=6 free stream:

a) A porous coating of regular porosity effectively diminishes the second-mode growth rate. Namely, the second-mode amplitude decreases twice on the surface covered by the UAC of 20% porosity. The DNS results agree satisfactory with predictions of linear stability theory (LST) for the second mode disturbances.

b) The UAC end effects, associated with junctures between solid and porous surfaces, were simulated for the case of piecewise porous coating. It was found that these effects are localized over ~ 2-3 disturbance wavelength and can be neglected in calculations of the integral UAC performance.

c) DNS modeling of the UAC effect on the boundary-layer disturbances generated by free-stream acoustic waves was carried out. The porous coating essentially diminishes amplitudes of the boundary-layer modes F and S, when the fast acoustic wave radiates the flat plate at the angle of incidence $\theta = 0^\circ$. A slow acoustic wave of $\theta = 0^\circ$ predominantly excites the mode S. The UAC slightly destabilizes this mode in the upstream region (where the mode S corresponds to the Mack first mode) and stabilizes it in the downstream region (where the mode S corresponds to the Mack second mode). This behavior is consistent with LST. A fast acoustic wave of $\theta = +45^\circ$ weakly excites the boundary-layer modes since this wave does not meet the synchronization condition. In this case, the acoustic field dominates in the boundary layer. The porous coating weakly affects these acoustic disturbances.

DNS of disturbances generated by a local periodic suction-blowing on a sharp cone at zero angle of attack was carried out for the cases with and without UAC. The disturbance dynamics is similar to the flat plate case. However, the second-mode growth rates resulted from DNS are higher than that observed in the wind-tunnel experiments. This discrepancy is presumably due to nonlinear effects.

The aforementioned DNS studies confirm the UAC stabilization concept for hypersonic flows over a flat plate and a sharp cone at zero angle of attack. It was shown that the linear stability theory can be used for estimates of UAC stabilization effects. Three-dimensional DNS is needed to treat nonlinear phases of transition.

3) Analytical expressions of the UAC reflection coefficient were derived for a wide range of ambient pressures p with emphasis on low pressures relevant to high-altitude flight. Apparatus for benchmark (no flow) measurements of ultrasonic absorption by porous coatings was assembled. Its robustness was demonstrated in the range of ambient pressure from 10 to 1000 mbar. The reflection coefficients predicted with the theoretical model agree well with the benchmark measurements conducted at ultrasonic frequency 200 kHz for UAC of regular microstructure (comprising equally spaced blind cylindrical holes of diameter 100 μm, depth 560 μm and spacing 200 μm) in the range of p from 20 to 800 mbar. For ambient pressures less than 20 mbar, additional measures should be taken to increase accuracy of experimental data.

4) The interaction of incident acoustic waves with groups of equally-spaced micro-cavities on the plate surface without external flow was investigated using theoretical modeling and DNS. Numerical simulations are performed for a porous coating consisting of 2-D cavities of length to depth ratio 0.12, with an incoming planar acoustic pulse at normal incidence. The reflection coefficient is computed for coatings of different porosity at various Reynolds numbers. Comparisons with theoretical prediction show excellent agreement with the DNS results in the range of parameters relevant to laminar-flow control applications. Parametric study of the geometrical factors (cavity aspect ratio, porosity) and flow conditions effects (Reynolds number, angle of incidence) should be continued in future.

5) New approach for solving the problem of slow gas motions in porous fibrous materials has been developed. The gas parameters were decomposed into two components. The first is the exact solution averaged over a cell volume, and the second is responsible for local perturbations caused by solid fibrous. The differential equations governing this problem were derived from first principles. It was shown that these equations contain terms of the phenomenological model of Brinkman that is widely used for practice. In this framework, the problem of sound absorption by layered fibrous materials of high porosity was formulated. Its general solution was expressed in terms of Fourier series. This study provides a solid foundation for further developments of mathematical models predicting acoustic processes in UAC of random microstructure. This, in turn, will help to refine the boundary conditions on the UAC surface for the boundary-layer stability problem.

6) A 1-m length cone with the felt-metal coating was tested in the ITAM AT-303 wind tunnel at Mach=8.8. Transition measurements were carried out on coated and uncoated cone surfaces at different bluntness radii (R = 0, 1, 2, 4, 8 mm) of the cone tip. The cone configuration is similar to the FRESH FX-1 fore-cone shape. Transition loci were determined from measurements of heat flux distributions. It was shown that the felt-metal coating causes 1.3-1.85 time increase of the laminar run. These experimental data need to be analyzed using our theoretical and computational tools.

7) First samples of ceramic UAC integrated into the shuttle TPS tile were fabricated. It was shown that by using a stamping technique it is feasible to make large arrays of uniformly spaced blind holes of 100-200 μm diameter and of 500-600 μm depth. The parameters of these pores fit the laminar flow control requirements predicted by our theory. The aforementioned UAC samples have slightly conical holes, which may be preferable in practice. In this connection, we recommend an investigation (theoretical, numerical and experimental) of the UAC-LFC performance in the case of conical pores.

This project produces enabling technology and design tools for the UAC-LFC methodology. The results reported herein provide a solid foundation for large-scale demonstration of the UAC-LFC performance in the CUBRC LENS I tunnel as well as fabrication of ceramic UAC samples integrated into TPS. This, in turn, provides basis for design of UAC-TPS test articles that could be manufactured and deployed on a flight vehicle.

Important that UAC is passive rather than active system, and thus it is more robust under high temperatures in hypervelocity flows. Thin porous coatings can be naturally integrated into TPS and provides more than doubling of laminar run with virtually no penalties. In this connection, the project directly links to the FRESH program. Namely, the UAC-TPS articles could be flight tested within the framework of the HIFiRE (Hypersonic International Flight Research and Experimentation) program that includes transition measurements on cones and other hypersonic configurations.

References

1. Malik, M.R., Zang, T.A., and Bushnell, D.M., "Boundary Layer Transition in Hypersonic Flows," AIAA Paper No. 90-5232, 1990.
2. Schneider, S.P., "Flight Data for Boundary Layer Transition at Hypersonic and Supersonic Speeds," *J. Spacecraft and Rockets*, Vol. 36, No. 1, pp. 8-20, 1999.
3. Schneider, S.P., "Hypersonic Laminar-Turbulent Transition on Circular Cones and Scramjet Forebodies," *Progress in Aerospace Sciences*, Vol. 40, No. 1-2, Feb. 2004, pp. 1-50.
4. Kimmel, R., "Aspects of Hypersonic Boundary Layer Transition Control," AIAA Paper No. 2003-0772, Reno NV, Jan. 6-9, 2003.
5. Whitfield, J.D., and Iannuzzi, F.A., "Experiments on Roughness Effects on Boundary layer Transition up to Mach 16," AIAA Paper No. 68-0377, 1968.
6. Batt, R.G., and Legner, H.H., "A Review of Roughness-Induced Nosetip Transition," *AIAA J.*, Vol. 21, No. 1, 1983, pp. 7-22.
7. Lysenko, V.I., and Maslov, A.A., "Influence of Deep Cooling on Transition in Supersonic Boundary Layer," *Izv. AN SSSR, Mekh. Zhidk. I Gasa*, No. 2, 1981, pp. 43-49.
8. Malmuth, N.D., Fedorov, A.V., Shalaev, V.I., Cole, J., Khokhlov, A.P., Hites, M., and Williams, D., "Problems in High Speed Flow Prediction Relevant to Control," AIAA Paper No. 98-2695, 1998.
9. Fedorov, A.V., Malmuth, N.D., Rasheed, A., and Hornung, H.G., "Stabilization of Hypersonic Boundary Layers by Porous Coatings," *AIAA J.*, Vol. 39, No. 4, 2001, pp. 605-610.
10. Rasheed, A., Hornung, H.G., Fedorov, A.V., and Malmuth, N.D., "Experiments on Passive Hypervelocity Boundary Layer Control Using an Ultrasonically Absorptive Surface," *AIAA J.*, Vol. 40, No. 3, 2002, pp. 481-489.
11. Fedorov, A.V., Shiplyuk, A.N., Maslov, A.A., Burov, E.V., and Malmuth, N.D., "Stabilization of a Hypersonic Boundary Layer Using an Ultrasonically Absorptive Coating," *J. Fluid Mech.*, Vol. 479, 2003, pp. 99-124.

12. Fedorov, A.V., Kozlov, V.F., Shiplyuk, A.N., Maslov, A.A., Sidorenko, A.A., Burov, E.V., and Malmuth, N.D., "Stability of Hypersonic Boundary Layer on Porous Wall with Regular Microstructure," AIAA Paper No. 2003-4147, 2003.

13. Bountin, D.A., Shiplyuk, A.N., Maslov, A.A., and Chokani, N., "Nonlinear Aspects of Hypersonic Boundary Layer Stability on a Porous Surface," AIAA Paper No. 2004-0255, Reno NV, Jan. 5-8, 2004.

14. Maslov, A., Shiplyuk, A., Sidorenko, A., Polivanov, P., Fedorov, A., Kozlov, V., and Malmuth, N., "Hypersonic Laminar Flow Control Using a Porous Coating of Random Microstructure," AIAA Paper No. 2006-1112, Reno NV, Jan. 9-12, 2006.

15. Kimmel, R.L., Adamczak, D., Gaitonde, D., Rougeux, A., and Hayes, J.R., "HIFiRE-1 Boundary Layer Transition Experiment Design," AIAA Paper No. 2007-534, Reno NV, Jan. 8-11, 2007.

16. Egorov, I.V., Fedorov, A.V., Novikov, A.V., and Soudakov, V.G., "Direct Numerical Simulation of Supersonic Boundary-Layer Stabilization by Porous Coating," AIAA Paper No. 2007-948, Reno NV, Jan. 8-11, 2007.

17. Mack, L.M., "Boundary Layer Stability Theory," Part B. Doc. 900-277, JPL, Pasadena, California, May 1969.

18. Fedorov, A.V., and Malmuth, N.D., "Parametric Studies of Hypersonic Laminar Flow Control Using a Porous Coating of Regular Microstructure," AIAA Paper No. 2008-588, Reno NV, Jan. 2008.

19. Kozlov, V.F., Fedorov, A.V., and Malmuth N.D., "Acoustic Properties of Rarefied Gases inside Pores of Simple Geometries," *J. Acoust. Soc. Am.,* Vol. 117, No. 6, 2005, pp. 3402-3412.

20. Johnson H.B., Alba C.R., Candler G.V., MacLean M., Wadhams T., and Holden M. "Boundary Layer Stability Analysis to Support the HIFiRE Transition Experiment," AIAA Paper No. 2007-311, Reno NV, 2007.

21. Egorov, I.V., Fedorov, A.V., Soudakov, V.G., "Direct numerical simulation of disturbances generated by periodic suction-blowing in a hypersonic boundary layer," *Theoret. Comput. Fluid Dynamics,* Vol. 20, № 1, 2006, pp. 41-54.

22. Egorov, I.V., Fedorov, A.V., Soudakov, V.G., "Direct numerical simulation of supersonic boundary layer receptivity to acoustic disturbances," AIAA Paper No. 2005-97, 2005.

23. Fedorov, A.V., "Receptivity of a high-speed boundary layer to acoustic disturbances," *J. Fluid Mech.*, Vol. 491, 2003, pp. 101-129.

24. Forgoston, E., and Tumin, A., "Initial-value problem for three-dimensional disturbances in a compressible boundary layer," *Physics of Fluids*, Vol. 17, № 8, 2005.

25. Demetriades, A., "Hypersonic Viscous Flow over a Slender Cone, Part III: Laminar Instability and Transition," AIAA Paper No. 74-535, 1974.

26. Kendall, J.M., "Wind Tunnel Experiments Relating to Supersonic and Hypersonic Boundary Layer Transition", *AIAA J.*, Vol. 13, 1975, pp. 290-299.

27. Stetson, K.F., Kimmel, R., Thompson, E.R., Donaldson, J.C., & Siler L.G. "A Comparison of a Planar and Conical Boundary Layer Stability and Transition at Mach Number of 8", AIAA Paper No. 91-1639, 1991.

28. Fedorov, A.V., Kozlov, V. F., and Addison, R.C., "Reflection of Acoustic Disturbances from a Porous Coating of Regular Microstructure," accepted to 5th AIAA Theoretical Fluid Mechanics Conference, Seattle, June 2008.

29. Blokhintsev, D. I., "The Propagation of Sound in an Inhomogeneous and Moving Medium I," *J. Acoust. Soc. Am.*, Vol. 18, 1946, pp. 322-328; see also Acoustics of Nonhomogeneous and Moving Medium, Gostekhizdat, Moscow, 1946 (translated as NACA-TM-1399).

30. Brès, G.A., and Colonius, T., "Three-Dimensional Liner Stability Analysis of Cavity Flows," AIAA Paper No. 2007-1126, 2007.

31. Brès, G.A., and Colonius, T., "Direct Numerical Simulation of Three-Dimensional Cavity Flows," AIAA Paper No. 2007-3405, 2007.

32. Brès, G.A., and Colonius, T., "Three-Dimensional Instabilities in Compressible Flow over Cavities," *J. Fluid Mechanics*, 2007, accepted for publication.

33. Brès, G. A., Colonius, T., and Fedorov, A. V., "Stability of Temporally Evolving Supersonic Boundary Layers over Micro-cavities for Ultrasonic Absorptive Coatings," invited - 5th AIAA Theoretical Fluid Mechanics Conference, Seattle, June 2008.

34. De Boer, R., "Contemporary Progress in Porous Media Theory," *Appl. Mech. Rev.*, Vol. 53, No. 12, 2000, pp. 323-369.

35. Nigmatulin, R. I., *Principles of Mechanics of Heterogeneous Media*, Nauka, Moscow, 1978 (in Russian).

36. Kirchhoff, G., "Über den Einfluss der Wärmeleitung in einem Gase auf die Schallbewegung," *Poggendorfer Annalen*, Vol. 134, 1868, pp. 177-193.

37. Rayleigh, J. W. S., *The Theory of Sound*, Dover, New York, 1945.

38. Kozlov, V. F., "The theoretical model of heat conductivity in high-porous materials," (in Russian), Transactions of First Russian National Conference on Heat Transfer (published by Moscow Power Engineering Institute, Moscow), Vol. X, Pt. 2, 1994, pp. 3-7.

39. Brinkman, H.C., "A calculation of the viscous force exerted by a flowing fluid on a dense swarm of particles," *Appl. Sci. Res.,* Vol. A1, 1947, pp. 27-34.

40. Tarnow, V., "Compressibility of air in fibrous materials," *J. Acoust. Soc. Am.,* Vol. 99, No. 5, 1996, pp. 3010-3017.

41. Brinkman, H.C., "A calculation of the viscous force exerted by a flowing fluid on a dense swarm of particles," *Appl. Sci. Res.*, Vol. A1, 1947, pp. 27-34.

42. Tarnow, V., "Compressibility of air in fibrous materials," *J. Acoust. Soc. Am.*, Vol. 99, No. 5, 1996, pp. 3010-3017.

Publications

P1. Fedorov, A.V., and Malmuth, N.D., "Parametric Studies of Hypersonic Laminar Flow Control Using a Porous Coating of Regular Microstructure," AIAA Paper No. 2008-588, Reno NV, Jan. 2008

P2. Brès, G. A., Colonius, T., and Fedorov, A. V., "Stability of Temporally Evolving Supersonic Boundary Layers over Micro-cavities for Ultrasonic Absorptive Coatings," invited - 5th AIAA Theoretical Fluid Mechanics Conference, Seattle, June 2008.

P3. Fedorov, A.V., Kozlov, V. F., and Addison, R.C., "Reflection of Acoustic Disturbances from a Porous Coating of Regular Microstructure," accepted to 5th AIAA Theoretical Fluid Mechanics Conference, Seattle, June 2008.